TECHNISCHE UNIVERSITÄT DRESDEN

mpipks

Basis sets for light-matter interaction: from static coherent states to moving Gaussians

DISSERTATION

zur Erlangung des akademischen Grades

Doctor rerum naturalium (Dr. rer. nat.)

Mohammad Reza Eidi

Max-Planck-Institut für Physik komplexer Systeme

September 2022

Eingereicht am 21.03.2022

Betreuer : Prof. Dr. Jan Michael Rost

Vorsitzender : Prof. Dr. Jürgen Fassbender

Gutachter : Prof. Dr. Jan Michael Rost
Prof. Dr. Frank Großmann

Rigorosum : Prof. Dr. Frank Großmann
Prof. Dr. Arno Straessner

Protokollant : Prof. Dr. Jan Michael Rost

Verteidigt am 06.09.2022

To the lights of my life

my beloved parents, my kind wife, and my sweet daughter

for their warm wishes, continuous support, and encouraging presence

Acknowledgements

I would like to express my gratitude to my supervisor, Prof. Jan Michael Rost, for his guidance in completing my project and making me a better student who should always keep his motivation and curiosity alive. I wish to thank Dr. Alexandra Landsman and Dr. Mohsen Vafaee for advising me on the first part of my project. I would like to show my appreciation to my family and my friends and colleagues at the Max Planck Institute for the Physics of Complex Systems who made it easier for me to go through this scientific adventure and, more importantly, helped me to become a better person. I take this opportunity to thank the IT department, especially Mr. Huebert Scherrer-Paulus, and Mr. Thomas Müller, for always providing the computational facilities needed to carry on the research. I am thankful to Benjamin Rabe, Hamed Koochaki Kelardeh, and Sebastian Gemsheim for helping me to proofread this thesis and to Sajjad Azizi for providing some benchmark results used in this work.

Abstract

This thesis develops a computationally efficient way of employing Gaussian wave packets to study laser-induced electron dynamics in atomic and molecular systems by directly solving the time-dependent Schrödinger equation (TDSE). First, we investigate charge migration (treating the nuclei classically), high-order harmonic generation (HHG), and single-isolated attosecond pulse generation in the Hydrogen molecular ion subjected to intense laser fields in a different range of frequencies with a basis of static coherent states (SCS). Then, seeking for a smarter way of constructing and guiding a minimal set of time-dependent basis functions, we introduce a fast and accurate approach for optimizing s-type Gaussian type orbitals (GTOs) and apply it to calculate electronic states of different 1D and 3D time-independent systems. Finally, we apply our optimization approach to time-dependent problems. With our approach we obtain excellent agreement with the exact results for HHG spectra of the 1D Hydrogen atom and molecular ion exposed to intense laser fields, which is not possible even with a much larger basis of static s-type GTOs.

Kurzfassung

Diese Arbeit entwickelt einen numerisch effizienten Ansatz für die Verwendung von Gaußschen Wellenpaketen zur Untersuchung der laserinduzierten Dynamik von atomaren und molekularen Systemen durch direkte Lösung der zeitabhängigen Schrödingergleichung (TDSE). Beginnend mit statischen kohärenten Zuständen (SCS) untersuchen wir die Ladungsmigration (wobei wir die Kerne klassisch behandeln), die Erzeugung von Harmonischen höherer Ordnung (HHG) und die Erzeugung von isolierten Attosekundenimpulsen im Wasserstoffmolekül-Ion, das intensiven Laserfeldern in einem unterschiedlichen Frequenzbereich ausgesetzt ist. Als Ergebnis der Suche nach einer intelligenteren Methode zur Konstruktion und zeitabhängigen Anpassung eines minimalen Satzes von Basisfunktionen stellen wir einen schnellen und genauen Ansatz zur Optimierung von Gauß-Orbitalen (GTOs) vom s-Typ vor und wenden ihn erfolgreich zur Berechnung elektronischer Zustände verschiedener zeitunabhängiger 1D- und 3D-Quantensysteme an. Schließlich erweitern wir unseren Optimierungsansatz auf zeitabhängige Probleme. Mit unserem Zugang erzielen wir eine ausgezeichnete Übereinstimmung mit den exakten Ergebnissen für die HHG-Spektren des 1D-Wasserstoffatoms und Wasserstoffmolekül-Ions, die intensiven Laserfeldern ausgesetzt sind. Dies ist nicht möglich mit einer sogar viel größeren nicht optimierten (statischen) Basis aus s-Typ GTOs.

Table of Contents

List of Tables

List of Figures

List of Publications

1. M. Eidi, M. Vafaee, and A. Landsman.
   "Static coherent states method: One- and two-electron laser-induced systems with classical nuclear dynamics".
   In: *Applied Sciences* 8 (2018), p. 1252.

2. M. Eidi, H. Koochaki Kelardeh, M. Vafaee, and A. Landsman.
   "High-order harmonic generation by static coherent states method in single-electron atomic and molecular systems".
   In: *Journal of Computational Chemistry* 42 (2021), pp. 1312–1320.

3. M. Eidi, B. Rabe, and J. M. Rost.
   "A fast and highly accurate optimizer for s-type Gaussian basis sets".
   In preparation (2022).

List of Abbreviations

1D	One-**D**imensional
3D	Three-**D**imensional
TDSE	**T**ime-**D**ependent **S**chrödinger **E**quation
ITP	**I**maginary **T**ime **P**ropagation
RTP	**R**eal **T**ime **P**ropagation
GEVP	**G**eneralized **E**igen**v**alue **P**roblem
HHG	**H**igh-order **H**armonic **G**eneration
SAP	**S**ingle **A**ttosecond **P**ulse
USO	**U**nitary **S**plit **O**perator
SCS	**S**tatic **C**oherent **S**tates
CCS	**C**oupled **C**oherent **S**tates
GTO	**G**aussian **T**ype **O**rbital
STO	**S**later **T**ype **O**rbital
LCDAO	**L**inear **C**ombination of **D**istributed and **A**tomic **O**rbitals
SSFM	**S**plit-**S**tep **F**ourier **M**ethod
CAP	**C**omplex **A**bsorbing **P**otential

1 Introduction

Recent advances in attosecond technology have paved the way for profound insights into electron and nuclear dynamics in atomic and molecular systems on their natural timescales [1, 2] . In particular, the fine-tuned generation of coherent, ultrashort intense laser pulses makes it possible to control and manipulate electron dynamics and create a wide range of exciting applications in physics, chemistry, and biology [3–11].

Notwithstanding the impressive experimental accomplishments, obtaining an accurate and comprehensive interpretation of the time-dependent electron dynamics in atomic and molecular systems driven by strong light fields requires an extensive theoretical and computational support [7].

Due to the complexity arising from the laser interaction and the Coulomb forces, among a wide variety of computational methods for studying atomic and molecular systems exposed to intense laser fields, the direct solution of the time-dependent Schrödinger equation (TDSE) is arguably the only accurate theoretical approach. However, this approach is applicable to systems with a very limited number of degrees of freedom (DOF) in a finite region of momentum or coordinate space since the required computational resources grow exponentially with increasing DOF. Different TDSE approaches for simulating the electron dynamics in one- or two-electron atomic or molecular laser-induced systems have been introduced in one [12–18], two [19, 20], or three (full) [21–26] coordinate (or momentum) electronic dimensions. Some of these methods treat the nuclei in their investigated laser-induced system dynamically [12, 13, 15, 17–20, 24]. Moreover, we note the achievements in the interaction of two-electron molecules with attosecond pulses in the frequency domain of the ultraviolet (UV) and extreme ultraviolet (XUV) [27].

The developed numerical techniques for solving the TDSE are either based on the discretization on a grid or expansions into basis functions. The most recognized approaches are: discrete-variable representation (DVR) and finite difference discretization [28–32], momentum-space pseudospectral methods [33], B-spline basis functions [34, 35], hybrid Gaussian–B-spline basis [36], Gaussian wave packets and the variational multiconfigurational Gaussian (vMCG) approach [37–42], time-dependent configuration-interaction [43–45], different versions of the multiconfiguration time-dependent Hartree (MCTDH) [46–49],

and the multiconfiguration time-dependent Hartree-Fock (MCTDHF) [50–52] which takes into account anti-symmetrization of the electronic wave function in MCTDH.

To avoid heavy computational efforts of directly solving the TDSE, the strong field approximation (SFA), inherent in the Lewenstein model [53], is widely used as an approximation technique for computing nonlinear phenomena such as the high-order harmonic generation (HHG) in multi-electron systems subjected to an intense ultrashort laser field. Although SFA explains key qualitative features of HHG, it is not fully successful in describing the low harmonic region [53, 54]. Furthermore, using SFA in general implies that only one electron couples to the laser field. Moreover, the implicit assumption that the internal structure of the atom does not contribute to HHG, is an oversimplification.

In contrast to SFA, which neglects both the Coulombic potential after ionization and the influence of the laser field on the bound state, basis set approaches like the static coherent states (SCS) method and the optimized Gaussian-type orbitals (GTOs) that we have used in this thesis can treat the electron-nucleus Coulombic and the laser field potentials on the same footing by directly solving the TDSE.

This thesis aims to explore a cost-efficient approach to construct a set of Gaussian wave packets that precisely represent the time-dependent electronic wave function of a laser-induced system. Employing static basis functions alleviates the convergence problem that the trajectory-guided approaches like the coupled coherent states method (CCS) encountered in the past [55–57]. However, one might need a huge number of basis functions distributed in a relatively large volume. Our ultimate goal is to find a smart way of constructing and guiding a minimal number of basis functions that accurately describe the electronic wave function driven by an external laser field.

This thesis is structured as follows: In Chap. 2 (Sec 2.1), we expand the wave function of atomic and molecular systems on the basis of 3D static coherent states which are placed randomly in phase space. In Sec. 2.2, we apply this approach to investigate the charge migration in the 3D Hydrogen molecular ion H_2^+ exposed to a high-frequency laser field treating the nuclear motion classically. In Sec. 2.3, we study HHG and the single attosecond pulse (SAP) generation in the 3D H_2^+ subjected to low-frequency intense laser fields.

In Chap. 3, we introduce a procedure to determine the positions and the widths of the Gaussian wave packets in such a way that a minimal number of basis functions achieves the desired accuracy goal. To this end, we choose the simplest Gaussian basis functions (s-type GTOs). In Sec. 3.1, we describe our developed optimization approach for the s-type GTOs. In Sec. 3.2, we apply the introduced optimization technique to find the optimum exponents and center-positions of the s-type GTOs which accurately represent a desired electronic state of different 1D and 3D quantum systems.

In Chap. 4 (Sec 4.1), we extend our optimization approach to the time-dependent scenarios. In Sec. 4.2, we examine the performance of our time-dependent optimized basis in the time evolution of two eigenstates and two non-eigenstates of the 1D harmonic

oscillator. Finally, in Sec. 4.3, we come back to the HHG process treated by the SCS method in Sec. 2.3. We are now in a position to employ minimal sets of the time-dependent optimized s-type GTOs for investigating HHG in 1D single-electron atomic (the Hydrogen atom) and molecular (the Hydrogen molecular ion H_2^+) systems exposed to femtosecond intense laser pulses. We summarize the thesis and present possible future directions in Chap. 5.

We use atomic units (a.u.) (explained in detail in Sec. A), $e = \hbar = m_e = 1$, throughout this thesis unless stated otherwise.

2 Static coherent states for laser-induced dynamics

During the last two decades, a number of approaches have been developed on the basis of coherent states (CSs) to solve the TDSE for high-dimensional quantum systems interacting with intense laser fields and to investigate the related phenomena [38, 56–61]. Among many advantageous features of coherent states, the most important ones are the flexibility of generating the initial basis set and the fact that on the basis of CSs Coulombic potential singularities are removed and replaced by the complex error function. By implementing CSs for solving the TDSE, Shalashilin et al. introduced the coupled coherent states (CCS) method [58]. The CCS method was originally developed to simulate systems with distinguishable particles. For simulating fermionic systems, two different versions of a fermion coupled coherent state (FCCS) method were introduced [56, 60, 62]. The first version of the FCCS method, which was introduced by Shalashilin et al., uses a Slater determinant to symmetrize the CCS equations [56]. The second version of the FCCS method, introduced by Eidi et al. [60, 62], simplifies the process by (anti)symmetrizing the CSs grid. However, the CCS method and its derivatives are essentially trajectory-guided. The CCS method was already employed to compute HHG in a hypothetical laser-induced 1D system with one electron experiencing a simple Gaussian binding potential [55]. The most important concern regarding trajectory-guided approaches based on CCS is that they are not completely successful in getting high-quality convergence in real-time propagation of TDSE in realistic single- or two-electron systems experiencing an external laser field [55–58]. Due to their semi-classical character, such issues are tackled in SCS by using static grids of coherent states instead of trajectory-guided ones [61].

In this chapter, initially we briefly review the the static coherent states (SCS) method [61, 63] and its formulations. In the SCS method, in contrast to the CCS approach and other older methods that use an evolving grid of CSs [38, 64–67], the CSs grid remains constant throughout the whole simulation. For all SCS calculations, two complementary CS grid boxes form the static CS grid. CSs that are distributed in an internal box are suitable for simulating the ground state of the system. As in the SCS approach the CS grid is static, we need to enlarge the grid to insure getting a good result from computations of excited electronic states or real time simulations of the system exposed to an external laser field. To

do so, an additional number of CSs are distributed differently in an external box. The external box plays a crucial stabilizing role in the real time propagation of TDSE in the absence or presence of an external laser field considering classical nuclear dynamics. However, both of the internal and external boxes participate in all simulation procedures. In contrast to trajectory guided approaches such as the CCS method, which has serious convergence problems in real time simulations, we extend our static CS grid by adding a number of static coherent states (external box) with a distribution scheme suited especially for the real time simulations.

In Sec. 2.2, by implementing classical nuclear dynamics, we compute the electronic-state potential energy curves of 3D H_2^+ in the absence and presence of an external ultrashort (high-frequency) laser pulse and study the charge migration phenomenon. Next, in Sec. 2.3, we apply the SCS method to investigate the high-order harmonic generation and single attosecond pulse generation in 3D H_2^+ induced by a relatively low frequency laser field.

2.1 Theory for molecular systems

2.1.1 Quantum description of electronic motion

In the static coherent states method (SCS), to simulate a single (or two) -electron system, using a Gaussian distribution function a static grid of three (or six) dimensional coherent states (CS) is constructed in the phase space. Having generated the CS grid, it remains constant throughout the whole simulation. To do so, for each dimension of every electron in the system, the same number of one-dimensional coherent states is generated using

$$z = \frac{\gamma^{1/2}}{\sqrt{2}} q + i \frac{\gamma^{-1/2}}{\sqrt{2}\hbar} p, \tag{2.1}$$

where γ tunes the width of coherent states in phase space. In Eq. (2.1), q is the position and p is the momentum of the 1D coherent state. Using the fact that coherent states are eigenkets of the annihilation operator and eigenbras of the creation operator ,

$$\hat{a}\,|z\rangle = z\,|z\rangle \quad , \quad \langle z|\,\hat{a}^\dagger = \langle z|\,z^*. \tag{2.2}$$

It is simple to verify that these two operators are related to the position and momentum operators in each dimension in such a way that

$$\hat{q} = \frac{\gamma^{-1/2}}{\sqrt{2}}\big(\hat{a}^\dagger + \hat{a}\big) \quad , \quad \hat{p} = i\hbar\frac{\gamma^{1/2}}{\sqrt{2}}\big(\hat{a}^\dagger - \hat{a}\big). \tag{2.3}$$

For one-electron systems, a set of 3D coherent states is constructed from 1D coherent

states of each dimension of the electron

$$|\mathbf{Z}\rangle = |z_1\rangle \otimes |z_2\rangle \otimes |z_3\rangle = |z_1 z_2 z_3\rangle \,. \tag{2.4}$$

For two-electron systems, two sets of 3D coherent states corresponding to each electron form a set of 6D coherent states

$$|\mathbb{Z}\rangle = |\mathbf{Z}_{e_1}\rangle \otimes |\mathbf{Z}_{e_2}\rangle = |z_1 z_2 z_3 z_4 z_5 z_6\rangle \,. \tag{2.5}$$

For two electron systems, as the system is a fermionic one, the CS grid should be constructed in such a way that the total wave function of the system becomes anti-symmetric [56, 60, 62]. For example in the ground state of a two-electron system where the spin wave function is anti-symmetric, the spatial wave function should be symmetric. Since SCS method deals with the spatial wave function, the static CS grid should be symmetrized (or anti-symmetrized) to produce symmetric (or anti-symmetric) electronic states of a two-electron system [60, 62].

Coherent states are not orthogonal and form an over-complete basis set with the overlap matrix elements of

$$\Omega_{\mathbf{Z}\mathbf{Z}'} = \langle \mathbf{Z}|\mathbf{Z}'\rangle = \prod_{j=1}^{3n} \exp\left(-\frac{1}{2}\left(|z_j|^2 + |z'_j|^2\right) + z_j^* z'_j\right). \tag{2.6}$$

where n is the number of electrons in the system.

The wave function of a single (or two) electron system can be represented as a superposition of N three (or six) dimensional coherent states

$$|\Psi\rangle = \sum_{k=1}^{N} D_k \, |\mathbf{Z}_k\rangle \,, \tag{2.7}$$

with coefficients

$$D_k = \sum_{l=1}^{N} \Omega_{kl}^{-1} C_l, \tag{2.8}$$

where

$$C_l = \langle \mathbf{Z}_l|\Psi\rangle \,, \tag{2.9}$$

and Ω^{-1} is the inverse of the overlap matrix Ω. Applying the identity operator of coherent states [58, 62]

$$I = \sum_{k,l=1}^{N} |\mathbf{Z}_k\rangle \, \Omega_{kl}^{-1} \, \langle \mathbf{Z}_l| \tag{2.10}$$

to the TDSE, we get

$$\langle \mathbf{Z}_j| \frac{\mathrm{d}\,|\Psi\rangle}{\mathrm{d}t} = \frac{-i}{\hbar} \sum_{k,l=1}^{N} \langle \mathbf{Z}_j| \,\mathrm{H}\, |\mathbf{Z}_k\rangle \left(\Omega^{-1}\right)_{kl} \langle \mathbf{Z}_l|\Psi\rangle \,. \tag{2.11}$$

Since in the SCS method, coherent states $\langle \mathbf{Z}_j|$ are time-independent, Eq. (2.11) with the help of Eqs. (2.8) and (2.9) reduces to

$$\frac{\mathrm{d}C_j}{\mathrm{d}t} = \frac{-i}{\hbar}\sum_{k=1}^{N} \langle \mathbf{Z}_k|\mathrm{H}|\mathbf{Z}_l\rangle \, D_k \ , \tag{2.12}$$

where H is the Hamiltonian of the system.

For m nuclei fixed at position $\mathbf{R}_j$ with the atomic number $\mathscr{Z}_j$, the general Hamiltonian for a n-electron system, dipole-coupled to a laser field, $\mathrm{H} = \mathrm{T_e} + \mathrm{V_{en}} + \mathrm{V_{ee}} + \mathrm{V_{nn}} + \mathrm{V}_l^{Lg/Vg}$, reads

$$\mathrm{H} = \sum_{i=1}^{n} \frac{|\mathbf{p}_i|^2}{2} - \sum_{i=1}^{n}\sum_{j=1}^{m} \frac{\mathscr{Z}_j}{|\mathbf{r}_i - \mathbf{R}_j|} + \sum_{i=1}^{n}\sum_{i'>i}^{n} \frac{1}{|\mathbf{r}_i - \mathbf{r}_{i'}|} + \sum_{j=1}^{m}\sum_{j'>j}^{m} \frac{\mathscr{Z}_j \mathscr{Z}_{j'}}{|\mathbf{R}_j - \mathbf{R}_{j'}|} + \mathrm{V}_l^{Lg/Vg}. \tag{2.13}$$

In Eqs. (2.13), the first term is for the kinetic energy of n electrons, $\mathrm{T_e}$, and the second term is for the electron-nuclear Coulombic potentials,$\mathrm{V_{en}}$. For multi-electron systems one should also compute the third term which incorporates the repulsive potentials between the electrons, $\mathrm{V_{ee}}$. For multi-center systems the fourth term accounts for the repulsive potentials between the nuclei, $\mathrm{V_{nn}}$. In the presence of an external laser field, considering the dipole moment approximation, depending on the length or velocity gauges, for $\mathrm{V}_l^{Lg/Vg}$ we have

$$\mathrm{V}_l^{Lg/Vg} = \begin{cases} \displaystyle\sum_{i=1}^{n} \quad \mathbf{r}_i \cdot \mathbf{E}(t) & \text{Length gauge} \\ \\ \displaystyle\sum_{i=1}^{n} \mathbf{A}(t)\cdot\mathbf{p}_i + \frac{\mathbf{A}(t)^2}{2} & \text{Velocity gauge} \end{cases} , \tag{2.14}$$

where $\mathbf{E}(t)$ is the electric field and $\mathbf{A}(t)$ is the corresponding vector potential.

For the matrix elements of the kinetic energy of electrons in Eq. (2.13) on the base of a $3n$ dimensional CS grid, employing Eqs. (2.2) and (2.3), one obtains

$$\left\langle \mathbf{Z}_k \middle| \sum_{i=1}^{n} \frac{|\mathbf{p}_i|^2}{2} \middle| \mathbf{Z}_l \right\rangle = -\frac{\gamma}{2} \langle \mathbf{Z}_k|\mathbf{Z}_l\rangle \sum_{j=1}^{3n} \left(z_{kj}^{*2} + z_{lj}^2 - 2 z_{kj}^* z_{lj} - 1 \right), \tag{2.15}$$

where j is the dimension number. The matrix elements of electron-nuclear Coulombic potentials in Eq. (2.13) can be also calculated analytically [62, 68]

$$\left\langle \mathbf{Z}_k \middle| \frac{\mathscr{Z}_j}{|\mathbf{r}_i - \mathbf{R}_j|} \middle| \mathbf{Z}_l \right\rangle = \langle \mathbf{Z}_k|\mathbf{Z}_l\rangle \, \frac{\mathscr{Z}_j}{\sqrt{|\boldsymbol{\rho}_{ij}|^2}} \, \mathrm{erf}\left(\sqrt{\gamma |\boldsymbol{\rho}_{ij}|^2} \right), \tag{2.16}$$

where i, j are the index numbers of electrons and nuclei, respectively and

$$\boldsymbol{\rho}_{ij} = \frac{\mathbf{Z}_{k_i}^* + \mathbf{Z}_{l_i}}{\sqrt{2\gamma}} - \mathbf{R}_j. \tag{2.17}$$

The matrix elements of the electron-electron Coulombic potential in Eq. (2.13) gives [62, 68]

$$\left\langle \mathbf{Z}_k \left| \frac{1}{|\mathbf{r}_i - \mathbf{r}_{i'}|} \right| \mathbf{Z}_l \right\rangle = \langle \mathbf{Z}_k | \mathbf{Z}_l \rangle \frac{1}{\sqrt{|\boldsymbol{\rho}_{ii'}|^2}} \operatorname{erf}\left(\sqrt{\gamma |\boldsymbol{\rho}_{ii'}|^2} \right), \tag{2.18}$$

where

$$\boldsymbol{\rho}_{ii'} = \frac{\mathbf{Z}_{k_i}^* + \mathbf{Z}_{l_i}}{\sqrt{2\gamma}} - \frac{\mathbf{Z}_{k_{i'}}^* + \mathbf{Z}_{l_{i'}}}{\sqrt{2\gamma}}. \tag{2.19}$$

As it is evident from Eqs. (2.16) and (2.18), one of the most important features of coherent states is that *they remove the singularity of Coulombic potentials and replace it with the complex error function* (erf).

For the matrix elements of the external laser potential (Eq. (2.14)) exerted on each electron, using Eqs. (2.2) and (2.3), one can easily verify that

$$\left\langle \mathbf{Z}_k \left| \mathrm{H}_{l_{e_i}}^{Lg/Vg} \right| \mathbf{Z}_l \right\rangle = \begin{cases} \langle \mathbf{Z}_k | \mathbf{Z}_l \rangle \frac{1}{\sqrt{2\gamma}} (\mathbf{Z}_k^* + \mathbf{Z}_l) \cdot \mathbf{E}(t) & \text{Length gauge} \\ \\ \langle \mathbf{Z}_k | \mathbf{Z}_l \rangle \left(i\sqrt{\frac{\gamma}{2}} (\mathbf{Z}_k^* - \mathbf{Z}_l) \cdot \mathbf{A}(t) + \frac{\mathbf{A}^2(t)}{2} \right) & \text{Velocity gauge} \end{cases}. \tag{2.20}$$

In order to compute the time-dependent expectation value of any observable O on the basis of a static grid of coherent states, by employing the identity operator of coherent states from Eq. (2.10), one can write

$$\langle \Psi | \mathrm{O} | \Psi \rangle = \sum_{jklm} \langle \Psi | \mathbf{Z}_j \rangle \, \Omega_{jk}^{-1} \, \langle \mathbf{Z}_k | \mathrm{O} | \mathbf{Z}_l \rangle \, \Omega_{lm}^{-1} \, \langle \mathbf{Z}_m | \Psi \rangle \, . \tag{2.21}$$

Finally, by employing Eqs. (2.8) and (2.9) in Eq. (2.21) we get

$$\langle \Psi | \mathrm{O} | \Psi \rangle = \sum_{k,l=1}^{N} \langle \mathbf{Z}_k | \mathrm{O} | \mathbf{Z}_l \rangle \, D_k^* D_l. \tag{2.22}$$

To obtain the ground state of the system at a fixed inter-nuclear distance, one has two options: either propagating the time-dependent Schrödinger equation Eq. (2.12) in imaginary time (ITP) until the expectation value of the field-free Hamiltonian, Eq. (2.22) without the last term, converges to the lowest accessible value [62, 69] or solving the generalized eigenvalue problem (GEVP).

The higher electronic states of the system can be gained either by employing the Gram-Schmidt algorithm in the basis of coherent states [60] or directly from the solution of the GEVP. For a two-nuclei system, propagation of TDSE in imaginary time for a constant inter-nuclear distance would lead to the ground state of the system at that specific inter-nuclear

distance. Implementing this approach for two-nuclei systems, it is necessary to repeat this process for a wide range of inter-nuclear distances to accurately get the potential energy curve of different electronic states of the system [60]. This is quite cumbersome from the computational perspective.

Here, using the SCS method, we introduce another approach which can obtain the electronic state potential energy curves of a two-nuclei system in the absence or presence of an external laser field. This approach only needs the electronic states of the system for an initial inter-nuclear distance where the nucleus-nucleus force is high enough to dissociate the two nuclei. Electronic states of other inter-nuclear distances are computed by propagating the TDSE in real time in the basis of the initial static CS grid considering classical dynamics for the two nuclei.

2.1.2 Classical nuclear motion

Here, to treat the nuclei in the system dynamically, using the well-known Ehrenfest theorem

$$\frac{\mathrm{d}\left\langle \mathbf{p}_j \right\rangle}{\mathrm{d}t} = \left\langle -\boldsymbol{\nabla}\overline{V}_j \right\rangle = \left\langle \overline{\mathbf{F}}_j \right\rangle = M_j \frac{\mathrm{d}^2\left\langle \mathbf{R}_j \right\rangle}{\mathrm{d}t^2}, \tag{2.23}$$

we compute the expectation value of the position of each nucleus $\langle \mathbf{R}_j \rangle$ [61]. In Eq. (2.23), M_j is the nucleus mass, $\overline{V}_j$ is the sum of second and fourth terms of the Hamiltonian in Eq. (2.13) and correspondingly $\overline{\mathbf{F}}_j$ is the total force exerted on the nucleus j.

The expectation value of the electron-nucleus attractive forces can be computed by employing Eq. (2.22)

$$\langle \mathbf{F}_{ij} \rangle = \sum_{kl} \mathbf{F}_{ij_{kl}} D_k^* D_l. \tag{2.24}$$

From Appendix (B) it is straightforward to verify that

$$\mathbf{F}_{ij_{kl}} = \mathscr{Z}_j \left(\frac{4\gamma^3}{\pi} \right)^{1/2} \boldsymbol{\rho}_{ij} F_1\left(\gamma |\boldsymbol{\rho}_{ij}|^2\right) \langle \mathbf{Z}_k | \mathbf{Z}_l \rangle \,, \tag{2.25}$$

where F_1 is the first order Boys function. For the repulsive force between the nuclei we also have

$$\mathbf{F}_{jj'} = \mathscr{Z}_j \mathscr{Z}_{j'} \frac{\mathbf{R}_j - \mathbf{R}_{j'}}{|\mathbf{R}_j - \mathbf{R}_{j'}|^3} \quad , \quad \mathbf{F}_{j'j} = -\mathbf{F}_{jj'}. \tag{2.26}$$

We have applied the classical nuclear dynamics approach to achieve the potential energy curves of the ground state ($1s\sigma_g$) and the first excited state ($2p\sigma_u$) of H_2^+. At first, we computed the ground and the first excited states of the system at an initial inter-nuclear distance ($R = |\mathbf{R}_1 - \mathbf{R}_2| = 1.0\, a.u.$). Then, we propagated each of these electronic states in real time in the absence of any external field by considering classical nuclear dynamics. The initial velocity of the two nuclei is set to zero. The simulation results for dynamic nuclei approach (DN) are plotted in Fig. 2.1 and compared to the results from the static nucleus

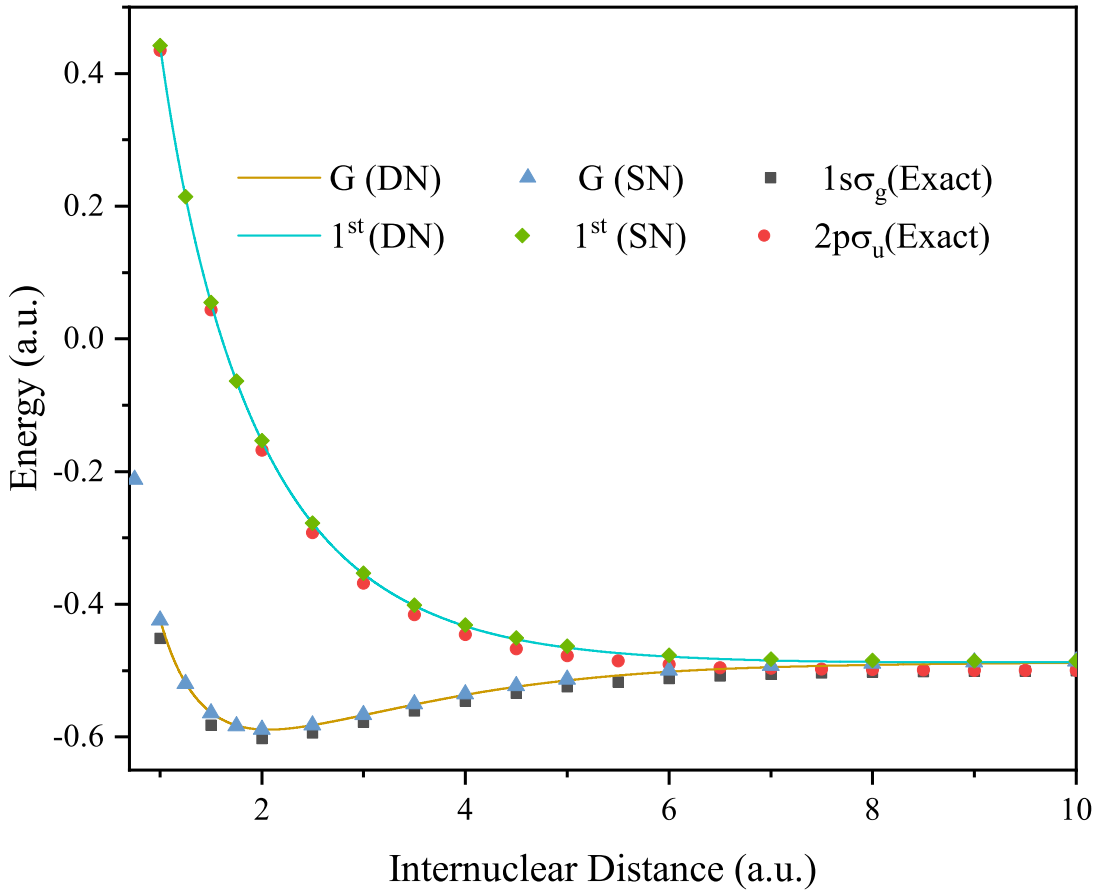

Figure 2.1 Potential energy curve of the ground state ($1s\sigma_g$) and the first excited state ($2p\sigma_u$) of H_2^+ computed employing the new dynamic nucleus (DN) approach. DN results have been compared to the static nucleus approach results (SN) [61] and the exact values [70] . SN results (exact values) are adopted with permission from Journal of Computational Chemistry (Atomic Data and Nuclear Data Tables) ; published by John Wiley and Sons (Elsevier), 2018 (1970).

approach (SN) [61] and the exact values [70]. It is evident from Fig. 2.1 that the DN results present a good agreement with the exact values [70]. In Fig. 2.1, for the ground state, the computation speed for the low inter-nuclear distances (below 1.5 a.u.) is high in that the nuclear dynamics at low inter-nuclear distances are fast. As the inter-nuclear distance gets larger (especially above 4 a.u.) the nuclear dynamics (and consequently the computation speed) becomes slower.

The implemented static CS grid in this section and the next one, which consists of 1000 CS in the internal box and 500 CS in the external box, has been generated using the Gaussian distribution function with $\gamma = 0.7$, compression parameters [62] for the internal box = 0.9 and for the external box = 1.0. Coherent states in the internal box are randomly distributed in the phase space around the origin in x, y, p_x, p_y and p_z directions and between (-6 a.u.,6 a.u.) in z direction. Coherent states in the external box are randomly distributed in the phase space between (-2.5 a.u.,2.5 a.u.) in x, y, p_x and p_y directions, between (-10 a.u.,10 a.u.) in z direction and between (-5 a.u.,5 a.u.) in p_z direction. A similar phase space illustration of

the used coherent state grid can be found at Fig. 2.9.

2.2 High frequency light-matter interaction

For the next round of our investigation, the ground state of H_2^+ at $R = 1.45$ a.u. is subjected to a 5-cycle ultra-short attosecond laser pulse using a wavelength of $\lambda = 70$ nm and different intensities. Attosecond pulses are needed to probe the electronic dynamics which typically takes place on sub-femtosecond time scales. We have assumed that the external laser field is linearly polarized along the z-axis and that the shape of the electric field is given by

$$\mathbf{E}(t) = f(t)E_0 \cos(\omega t)\hat{k}. \tag{2.27}$$

In Eq. (2.27) E_0 is the maximum amplitude of the laser field, ω is the angular field frequency and $f(t) = \sin^2(\frac{t}{\tau}\pi)$ is the envelope shape with the full width half maximum (FWHM) duration of τ.

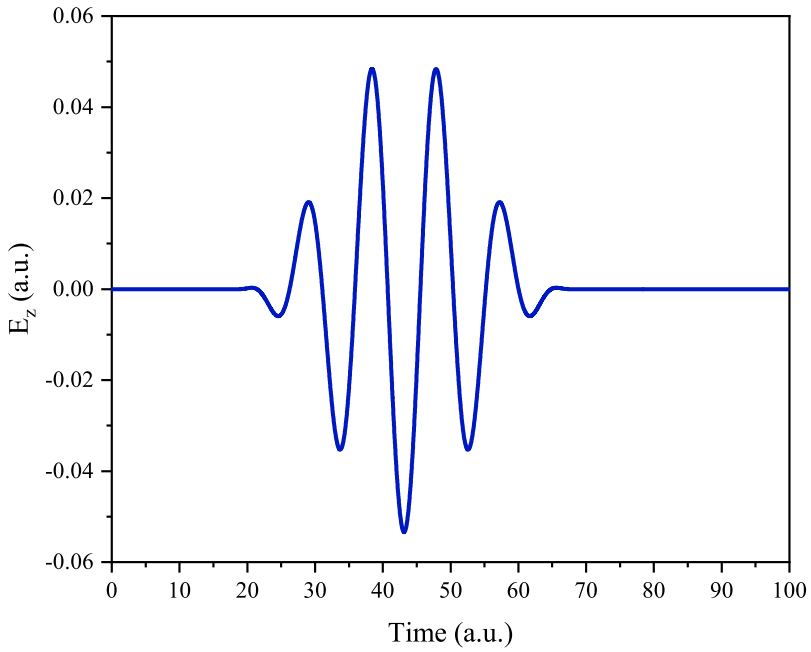

Figure 2.2 The shape of the implemented laser pulse: a 5-cycle attosecond laser pulse with wavelength of 70 nm and intensity of $10^{14}\,\mathrm{W/cm^2}$.

The shape of the used laser pulse is plotted in Fig. 2.2 for the intensity of $10^{14}\,\mathrm{W/cm^2}$. The corresponding energy for a single photon excitation (17.712 eV = 0.6509 a.u.) can be high enough for exciting the ground state of the system to the first excited state at $R = 1.45$ a.u..

In Fig. 2.3 the ground state of H_2^+ is exposed to laser fields with different intensities (from $0.1 \times 10^{14}\,\mathrm{W/cm^2}$ to $2.0 \times 10^{14}\,\mathrm{W/cm^2}$). When the internuclear distance reaches $R = 1.45$ a.u., the system experiences the maximum amplitude of the laser fields.

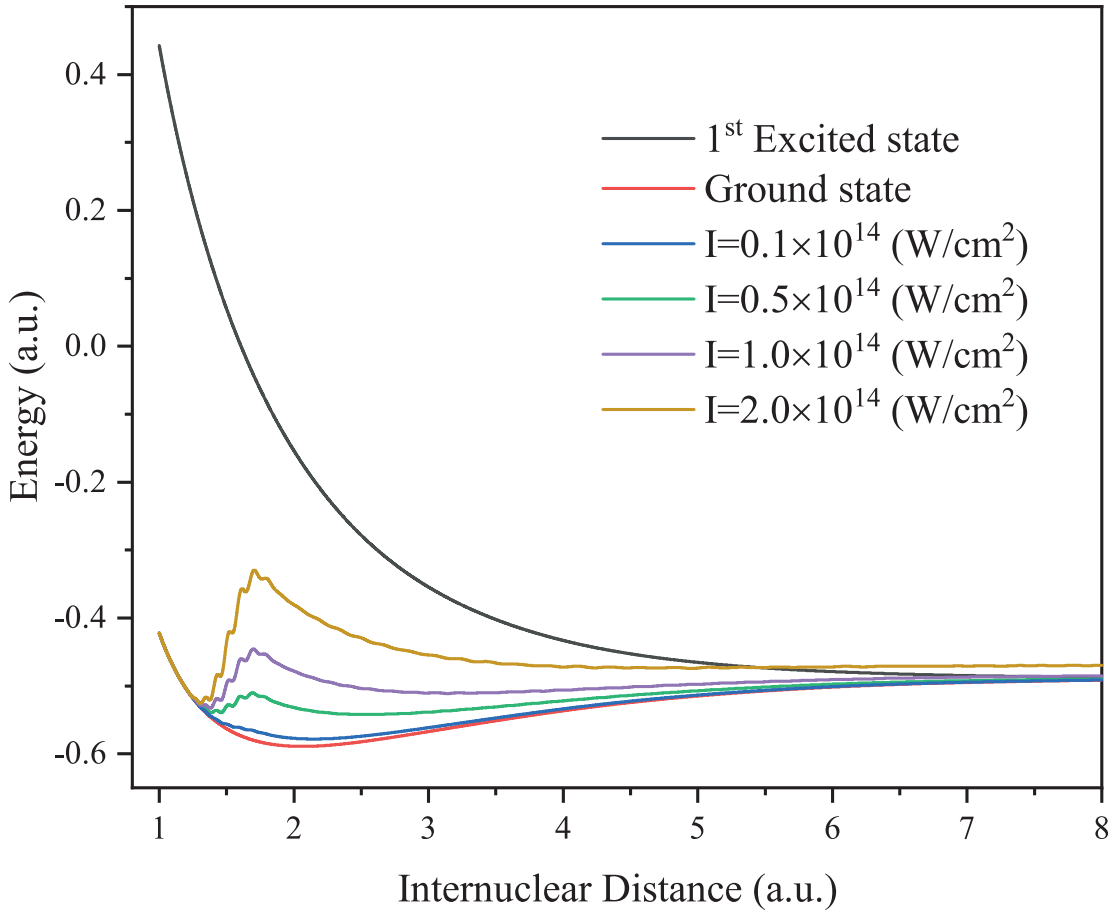

Figure 2.3 Potential energy curve of the electronic states of H_2^+ in the presence of ultra-short laser field with different intensities compared to the ground state and the 1^{st} excited state of the system.

2.2.1 Charge migration in 3D H_2^+

An interesting phenomenon which could happen here is the charge migration between the ground state and the first excited state of the system [21, 71]. The wave function of the resulting coherent superposition state which corresponds to a spatial displacement of the electronic charge is generally expressed by

$$\Psi_s(\mathbf{r},t;\mathbf{R}) = c_g(t)\exp(-iE_g(R)t)\Psi_g(\mathbf{r};\mathbf{R}) + c_u(t)\exp(-iE_u(R)t)\Psi_u(\mathbf{r};\mathbf{R}). \quad (2.28)$$

In general, the inter-nuclear distance $R = |\mathbf{R}| = |\mathbf{R}_1 - \mathbf{R}_2|$ can be varied in time considering classical nuclear dynamics. It is easy to verify that the time-dependent electron density which can migrate from one atom to the other is given by

$$|\Psi_s(\mathbf{r},t;\mathbf{R})|^2 = |c_g(t)|^2|\Psi_g(\mathbf{r};\mathbf{R})|^2 + |c_u(t)|^2|\Psi_u(\mathbf{r};\mathbf{R})|^2 + 2|A|\cos(\alpha(\mathbf{r};\mathbf{R})) \quad (2.29)$$

where

$$A = c_g^*(t)c_u(t)\Psi_g^*(\mathbf{r};\mathbf{R})\Psi_u(\mathbf{r};\mathbf{R}), \quad (2.30)$$

$$\alpha(\mathbf{r},\mathbf{R}) = (E_u(R) - E_g(R))t = \Delta E(R)t. \tag{2.31}$$

One prerequisite for the occurrence of the charge migration, is the existence of the spatial overlap (the third term in Eq. (2.29)) between the electronic wave functions describing the charge in each of the ground and the first excited states [71]. From the periodicity condition of the cos function in the third term of Eq. (2.29), one can easily compute the migration period of the electron density from one atom to the other one as

$$T = \frac{2\pi}{E_u(R) - E_g(R)}. \tag{2.32}$$

In order to compute the population of each electronic state $\Psi_{g/u}$ in the coherent superposition state Ψ_s, implementing the identity operator of coherent states (Eq. (2.10)) one should compute

$$\left|\left\langle \Psi_{g/u}\middle|\Psi_s\right\rangle\right|^2 = \left|\sum_{kl}\left\langle \Psi_{g/u}\middle|\mathbf{Z}_k\right\rangle (\Omega^{-1})_{kl}\left\langle \mathbf{Z}_l|\Psi_s\right\rangle\right|^2. \tag{2.33}$$

Applying Eqs. (2.8) and (2.9) we arrive at

$$\left|\left\langle \Psi_{g/u}\middle|\Psi_s\right\rangle\right|^2 = \left|\sum_{k} C^*_{g/u_k} D_{sk}\right|^2. \tag{2.34}$$

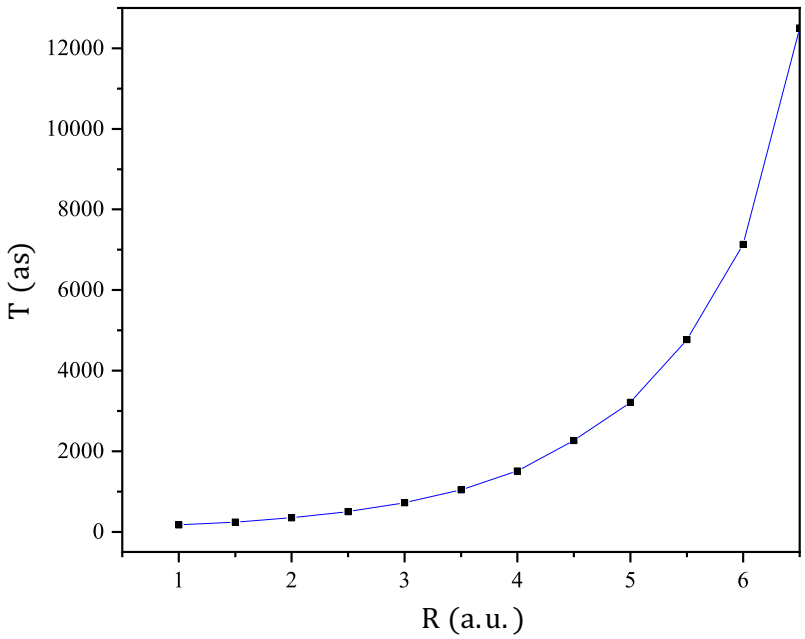

Figure 2.4 The charge migration period (T) computed by employing Eq. (2.32) for different inter-nuclear distances (R) in H_2^+ in the absence of an ultra-short intense laser field.

As it can bee seen from Fig. 2.4, by employing Eq. (2.32) we have computed the period of charge migration between the two nuclei in H_2^+ in terms of the inter-nuclear distance. This figure shows that higher inter-nuclear distances correspond to higher charge migration times between the two nuclei. In Fig. 2.4, the charge migration period in inter-nuclear distances

Table 2.1 Population of the ground state and the 1^{st} excited state in coherent superposition states for different intensities computed at a long time after turning off the laser.

Intensity ($\frac{W}{cm^2}$)	Ground state	1^{st} Excited state
0.1×10^{14}	0.980	0.020
0.5×10^{14}	0.895	0.102
1.0×10^{14}	0.801	0.191
2.0×10^{14}	0.671	0.298

between 1-2 a.u. is relatively low (about 200-300 as) and it gets larger as the inter-nuclear distance grows.

From the population results in Table. 2.1 which are computed (at a long time after turning off the laser) using Eq. (2.34) one can deduce that as the intensity of laser increases, the population of the ground state in the coherent superposition state gets lower and population of the excited states gets higher. In agreement with this deduction, it can be also seen from Fig. 2.3 that coherent superposition states created by lasers with lower intensity are closer to the ground state. Higher laser intensities lead to coherent superposition states with more contributors. For example, the coherent superposition state created by using a laser field with the intensity of $2.0 \times 10^{14} W/cm^2$ (in Fig. 2.3) has more contributors. Table (2.1) and Fig. 2.3 demonstrate that after exposing the ground state of system to an attosecond pulse, some of the population goes to the excited states. As the intensity of the attosecond laser field is increased, a larger population is transferred to the excited states.

Fig. 2.5 shows the expectation value of the electron coordinate along z axis experiencing ultra-short intense laser pulses with four different intensities. One can see that the amplitude of the coordinate expectation value is larger for higher intensities. However, until 2.0 fs the period seems to be the same for all intensities. As the dissociation rate of the two nuclei increases, the period becomes larger for higher intensities (above $t = 2.0$ fs). In addition, we have calculated the change rate of the inter-nuclear distance for the ground state and the first excited state in the absence of a laser field and for the ground state induced by ultra-short laser pulses with different intensities. The results, depicted in Fig. 2.6, show that the lowest (highest) rates of dissociation correspond to the ground (first excited) state in the absence of a laser field.

So far, the implemented static CS grid which consist of a total number of 1500 CS, was enough for studying the physics behind the classical nuclear motion and quantum dynamics of the single electron in H_2^+ in the absence of an external laser field (Sec. 2.1.2) and the charge migration in the presence of an ultra-short (70 nm) intense laser field (Sec. 2.2.1). It was because of the fact that the quiver motion of the single electron was not considerable for such a high frequency laser field.

In the next section, we would discuss how static coherent states perform for H_2^+ induced

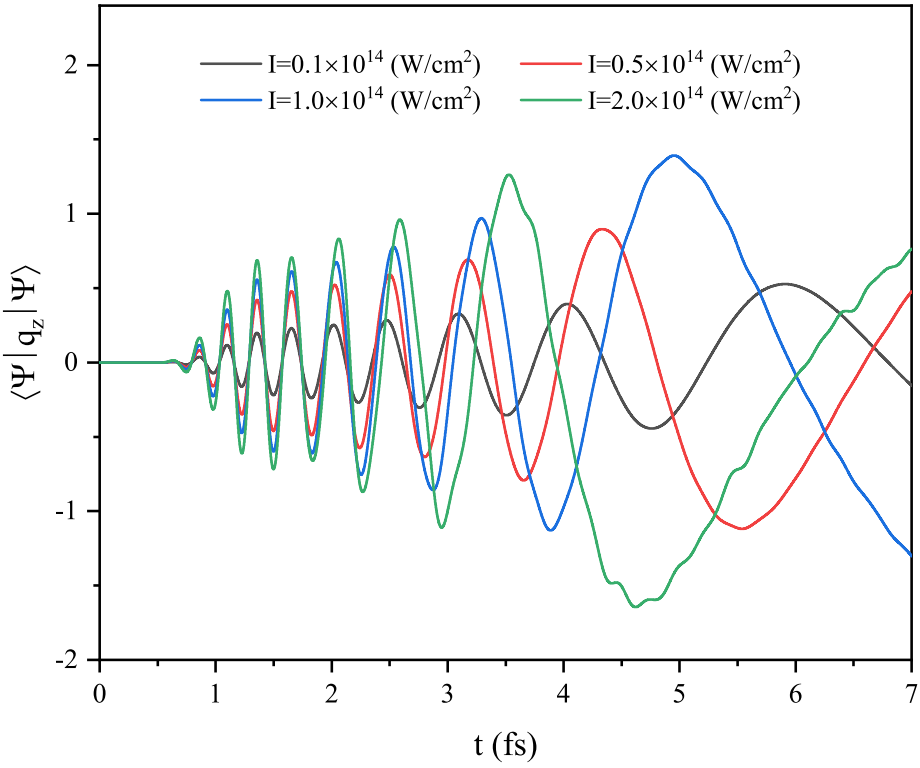

Figure 2.5 Expectation value of the position of the single electron in a laser induced H_2^+ along the z axis. Ultra-short intense laser fields (with four different intensities) strike the ground state of the system in a specific time.

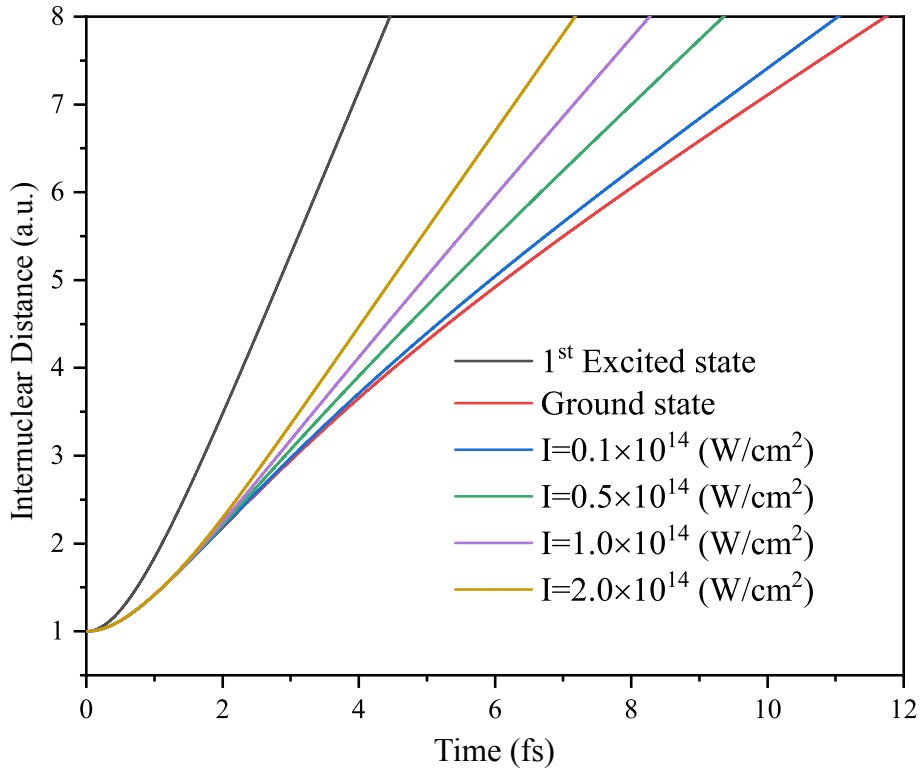

Figure 2.6 Initiating from the ground state, considering classical nuclear dynamics, the inter-nuclear distance of an ultra-short laser induced H_2^+ reaches faster from 1 a.u. to 8 a.u. than the field-free case (the red line). The results are also compared to the fastest one which is related to the 1^{st} excited state of the system in the absence of a laser field (the black line).

by a low-frequency (800 nm) intense laser field, which brings about a much higher quiver radius for the single electron.

2.3 Low frequency light-matter interaction

By exposing atomic and molecular systems to an intense low frequency laser field, among a wide range of phenomena, a remarkable phenomenon occurs in which coherent radiations with high-order multiples of the fundamental frequency of the driving field are generated.

In Sec. 2.3.1, we employ the SCS approach to investigate the so-called high-order harmonic generation (HHG) in the three-dimensional molecular hydrogen ion H_2^+ interacting with a linearly polarized optical field. Next, in Sec. 2.3.2, using the known polarization gating technique we explore the single isolated attosecond pulse generation in H_2^+ .

Same as Sec. 2.2, in both of these applications of the SCS method, we utilize two complementary internal and external CS grid boxes. However, here we need a higher total number of CS to fill a larger physical space in that the system interacts now with a low frequency laser field causing the electron to wander in a larger space.

2.3.1 High-order harmonic generation in 3D H_2^+

The underlying physics of the non-perturbative HHG process, which is a highly nonlinear response of matter to the ultrashort intense laser fields, can be explained by invoking the well-known semi-classical three-step model [54, 72, 73], with quantum mechanical treatment given within the so-called Lewenstein model [53]. In these models, the electron which is freed to the continuum through tunneling ionization is accelerated back by the external laser field and a harmonic photon is emitted via recombination of the electron and its parent ion. The three-step model is schematically depicted in Fig. 2.7. It was predicted theoretically and demonstrated experimentally that the produced HHG spectrum, which falls rapidly in the first few harmonics, produces a broad plateau that ends with a sharp cutoff. This cutoff which corresponds to the maximum kinetic energy K_{max} that an electron can gain upon recombination, can be calculated by the semi-classical three-step model or its quantum-mechanical correction (the Lewenstein model) [53, 74]

$$n_{\text{cutoff}} = \frac{K_{max}}{\hbar\omega_0} = \frac{1}{\hbar\omega_0}\left(3.17U_p + f\left(\frac{I_p}{U_p}\right)I_p\right), \tag{2.35}$$

where I_p is the ionization potential, $U_p = E_0^2/4\omega_0^2$ is the ponderomotive potential, ω_0 is the angular frequency of the laser field, and E_0 is the electric field amplitude. Based on the Lewenstein model, $f(\frac{I_p}{U_p})$ tends to 1.32 as $\frac{I_p}{U_p} \to 0$ and as $\frac{I_p}{U_p} \to \infty$ it approaches to 1, and subsequently the Lewenstein model reduces to the semi-classical three-step model. Third order polynomial fitting to the function curve in Fig. 5 of [53], one can obtain the following

function for $f(\frac{I_p}{U_p})$

$$f\left(\frac{I_p}{U_p}\right) = -0.03592\left(\frac{I_p}{U_p}\right) + 0.00610\left(\frac{I_p}{U_p}\right)^2 - 0.00056\left(\frac{I_p}{U_p}\right)^3 + 1.31875 \quad (2.36)$$

which is relatively accurate for $\frac{I_p}{U_p} < 10$.

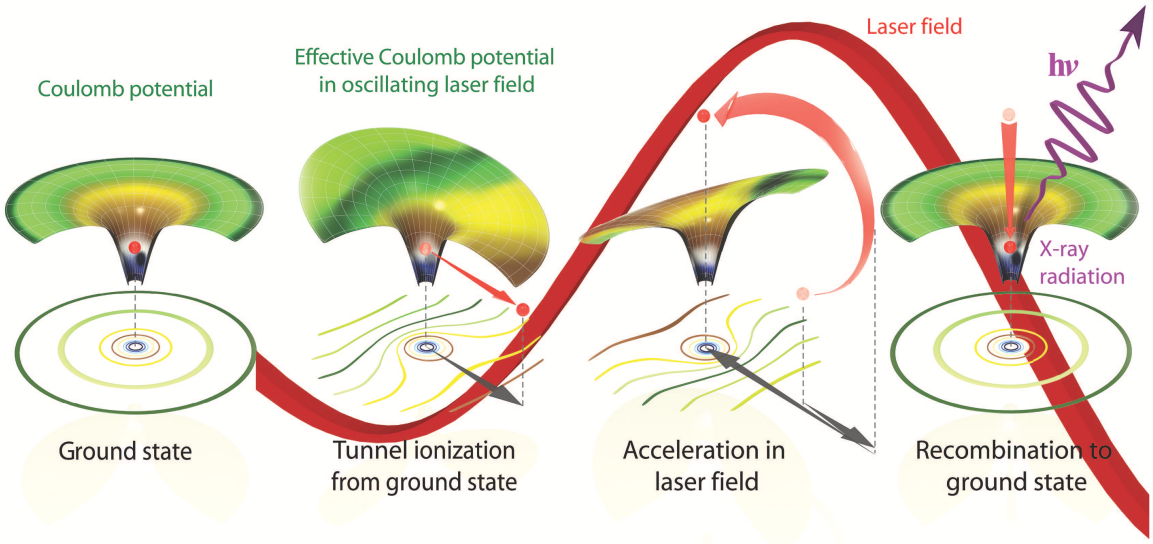

Figure 2.7 Schematic illustration of the HHG process by the semi-classical three-step model. Adopted from [75, 76] .

In this section, starting the real time propagation (RTP) process from the ground state of H_2^+ at two different fixed initial inter-nuclear distances $R = 2\ a.u.$ and $R = 3\ a.u.$, we study the HHG in the length and the velocity gauges exposing the system to a trapezoidal 800 nm 5-cycle linear (along the z axis) laser pulse with the intensity of $I = 10^{14}$ W/cm^2. Such a laser field is depicted in Fig. 2.8 and has the same propagation form of Eq. (2.27). For the applied intensity, n_{cutoff} for H_2^+ at internuclear distances $R = 2.0\ a.u.$ and $R = 3.0\ a.u.$ are predicted by the 3-step model (Lewenstein model) to be approximately 32 (36) and 28 (32), respectively.

Here, we have used a total number of 8000 3D CSs distributed randomly around the two nuclei ($z_{ini}^{x/y} = 0$ and $z_{ini}^{z} = \pm R/2$). The nuclei are considered to be fixed along the z direction. We exclude high energy coherent states and keep coherent states with energies $\langle \mathbf{Z}|H|\mathbf{Z}\rangle < 1.5$ a.u. for the internal box and $\langle \mathbf{Z}|H|\mathbf{Z}\rangle < 2.0$ a.u. for the external one. 3D coordinate (a) and momentum (b) representations of such grid are depicted in the left panel of Fig. 2.9 while the 2D phase space representations of the grid are illustrated in the right panel. Because the induced laser has a polarization along z direction, coherent states are distributed more widely along the z direction than x and y directions. The external box (5000 CSs) is considered to be three times larger than the internal box in all dimensions to capture phenomena occurring beyond the effective Coulombic range. The gamma parameter is set to $\gamma = 1$. The region in proximity of the nuclei should involve more CSs to capture

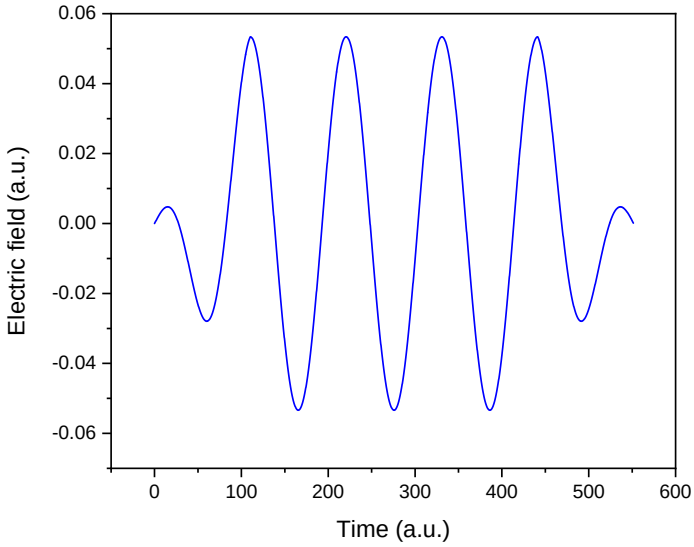

Figure 2.8 Our used trapezoidal 5-cycle 800 nm femtosecond laser pulse with the intensity of 10^{14} W/cm^2. The envelope amplitude rises in the first cycle, remains constant in the following three cycles and falls in the last cycle.

short-range phenomena such as Coulombic potential effects. The size of the constructed grid is considered to be approximately three times larger than the predicted quiver amplitude $\alpha_p = \frac{E_0}{\omega^2} = 16.45\ a.u.$ (for the intensity of $I = 10^{14}$ W/cm^2).

To get the HHG spectrum $D(\omega)$ one needs to compute the squared magnitude of the Fourier transforms (FT) of the expectation value of the electron dipole acceleration $\mathbf{A}_e$ (Eq. (2.39))

$$D(\omega) = \left| \int_0^T \langle \psi | \mathbf{A}_e | \psi \rangle \, H(t) e^{-i\omega t} \mathrm{d}t \right|^2, \tag{2.37}$$

where T is the total pulse duration and

$$H(t) = \frac{1}{2}\left[1 - \cos\left(2\pi \frac{t}{T}\right)\right] \tag{2.38}$$

is the Hanning function which filters nonphysical features (non decaying components) from the HHG spectrum as the Fourier transform is applied over a finite time.

The expectation value of the dipole acceleration of the single electron in H_2^+ can be computed using again the Ehrenfest theorem

$$\langle \psi | \mathbf{A}_i | \psi \rangle = \left\langle -\boldsymbol{\nabla} \overline{V}_i \right\rangle = \left\langle \overline{\mathbf{F}}_i \right\rangle \tag{2.39}$$

where $\overline{V}_i$ is the sum of the second, the third and the last terms of the Hamiltonian in Eq. (2.13) and correspondingly $\overline{\mathbf{F}}_i$ is the total forces exerted on the electron i.

For the expectation value of the nucleus (j) - electron (i) attractive forces $\mathbf{F}_{ji}$, with the

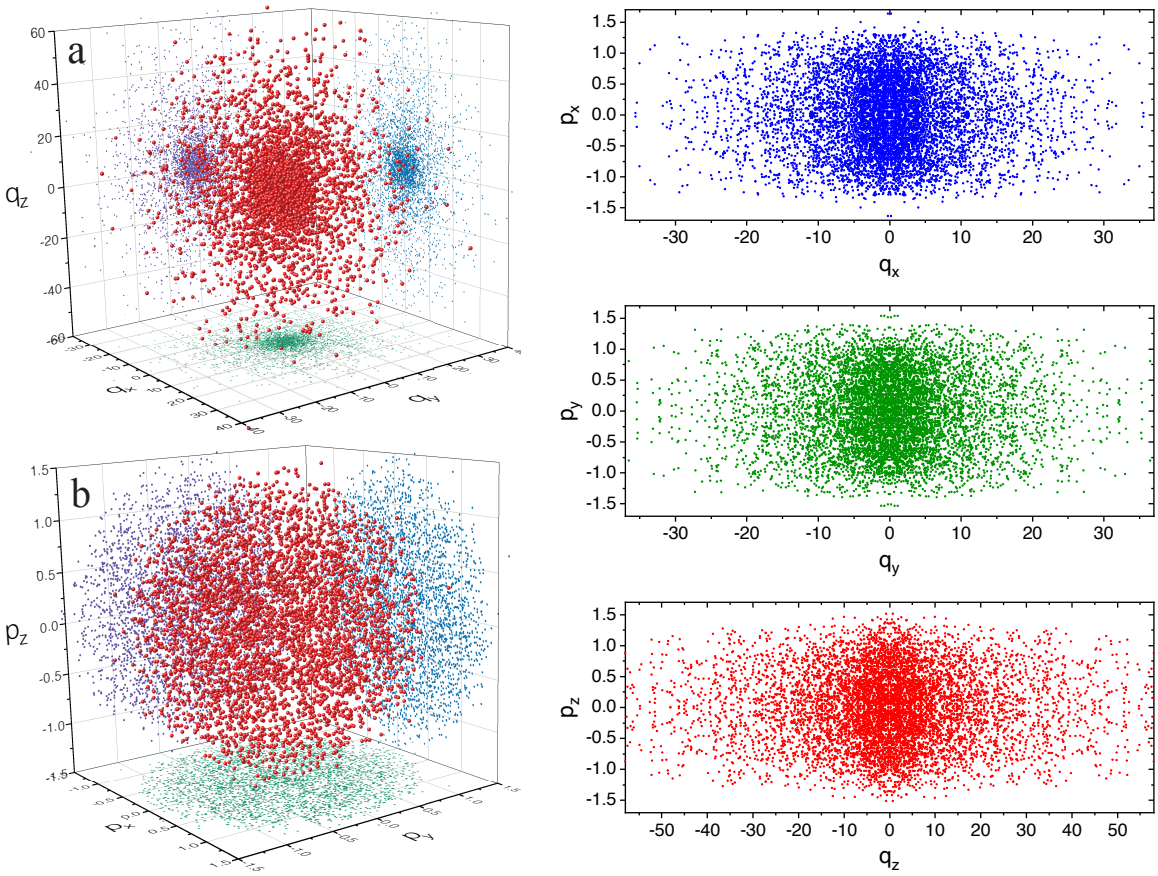

Figure 2.9 Left panel: (a) 3D coordinate space and (b) 3D momentum space representations of a random CS grid (with a total number of 8000 CSs) used for simulating HHG in H_2^+ (at R = 3 a.u.) induced by a 5-cycle linearly polarized laser field in the z- direction (with λ = 800 nm). Right panel: Phase space representations of the same grid.

help of Appendix (B) one can get

$$\langle \mathbf{F}_{ji} \rangle = \sum_{kl} \mathbf{F}_{ji_{kl}} D_k^* D_l \tag{2.40}$$

where

$$\mathbf{F}_{ji_{kl}} = -\left(\frac{4\gamma^3}{\pi}\right)^{1/2} \boldsymbol{\rho}_{ij} F_1\left(\gamma |\boldsymbol{\rho}_{ij}|^2\right) \langle Z_k | Z_l \rangle \tag{2.41}$$

and F_1 is the first order Boys function (Eq. (B.15)).

To prevent nonphysical effects due to the reflection of the wave packet from the boundaries, the coefficients C_k corresponding to each coherent state k are multiplied by a mask function with the form [77]

$$M_{k_j} = \begin{cases} 1 & \left|q_{k_j}\right| < Q_j \\ \cos^{\frac{1}{8}}\left(\frac{\pi}{2} \frac{\left|\left|q_{k_j}\right| - Q_j\right|}{b_j}\right) & \left|q_{k_j}\right| > Q_j \end{cases} \tag{2.42}$$

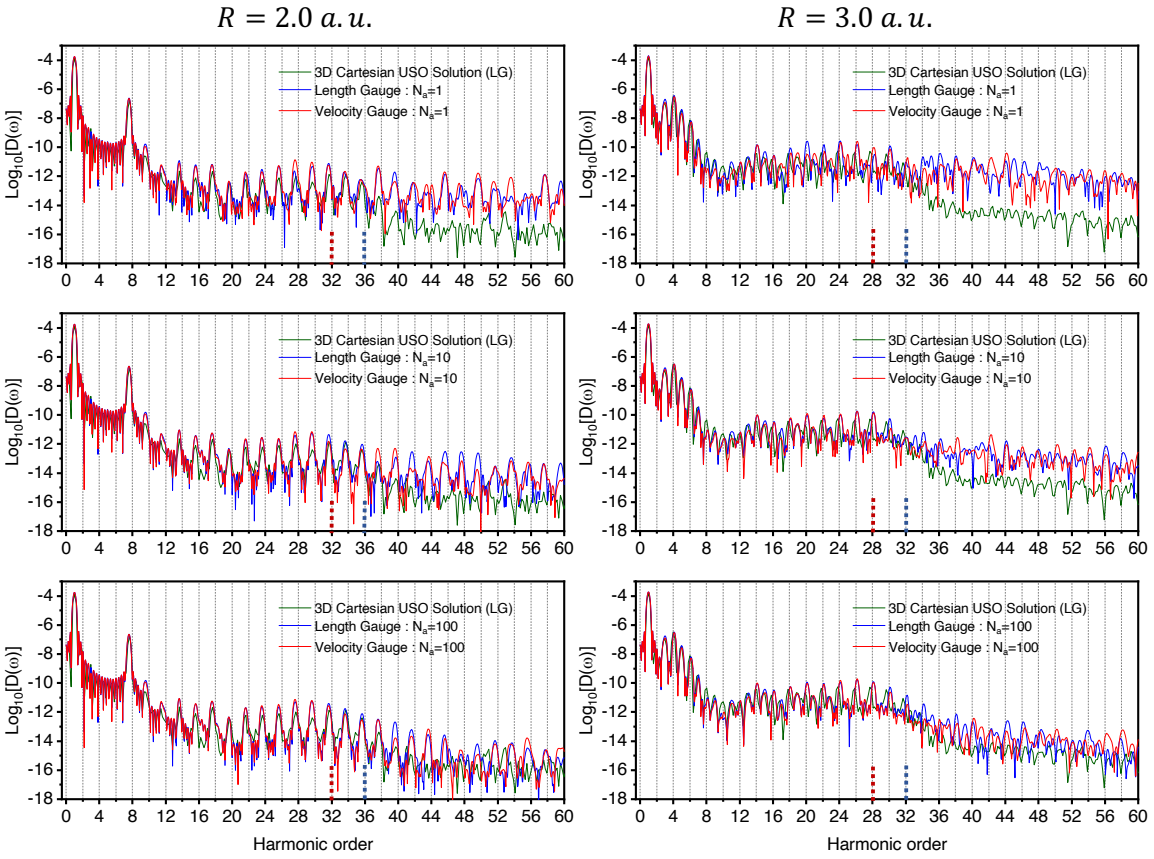

Figure 2.10 The HHG spectrum of H_2^+ , calculated by the SCS method in the length and the velocity gauges at $R = 2.0$ a.u. (left panel) and $R = 3.0$ a.u. (right panel), induced by a 5-cycle trapezoidal 800 nm laser field with the intensity of $I = 10^{14}$ W/cm^2 in comparison with the a 3D Cartesian USO length gauge solution of TDSE . The observed deviation between SCS results and those of the Cartesian USO solver in the above cutoff region are slightly improved by increasing the number of averaged random simulations from $N_a = 1$ (a) up to $N_a = 100$ (c). The red and the blue vertical dashed lines plot the cut-off harmonics, predicted by the 3-step and the Lewenstein models, respectively.

where Q_j gives the boundary point in the j^{th} direction, b_j is the length of absorbing region and q_{k_j} is the position of the k^{th} coherent state in the j^{th} direction.

In Fig. 2.10, we have depicted the resulted HHG spectrum for H_2^+ interacting with a trapezoidal laser field at $R = 2$ a.u. (left panel) and at $R = 3$ a.u. (right panel) in length and velocity gauges which are compared to the length gauge results of a 3D Cartesian unitary split operator (USO) solver of the TDSE [63]. Since coherent states are generated randomly, simulations with the same settings would lead to different grids of coherent states. Consequently, by repeating the simulation and averaging the expectation values of the acceleration of the electron along the z-direction, a lot more CSs can be used. This is an important characteristics of the SCS method which notably improves the results at a relatively small computational cost.

The averaging factor, N_a, defines the number of recurring random simulations. As can be seen in Fig. 2.10, even with only 8000 CS ($N_a = 1$) the HHG spectra obtained from SCS

is in agreement with that of 3D Cartesian USO in the low harmonic regions. In addition, the consistency of SCS with 3D Cartesian USO is acceptable in the plateau region (below cutoff). The inconsistency which arises after cutoff can be slightly improved including more CS into the simulation, i.e. increasing N_a (cf. Fig. 2.10). As it is evident from Fig. 2.10, increasing N_a and hence including more CS into the simulation (up to 800,000 for N_a=100), the results show a better agreement with those of 3D Cartesian USO method. Nevertheless, no sensible changes were seen in the HHG results of SCS as we enlarged the external box or increased the total number of CSs participated into a single simulation (higher than 8000 CSs).

For the 3D Cartesian USO solution of TDSE the grid size is considered to be almost the same as those we used in SCS. However, a total number of 42,250,000 grid points (324, 324 and 400 grid points in the x, y and z directions, respectively) are taken into account. Using such a high number of grid points to compute HHG spectrum of the system is not computationally cost-effective. One can instead exploit the 3D cylindrical USO solution of TDSE [78], which due to its intrinsic cylindrical symmetry is less costly and requires fewer grid points (a total number of 259,200) compared to 3D Cartesian USO.

As can be concluded from the last row of Fig. 2.10, we see an acceptable agreement, especially between the length and the velocity gauges results. Above the cutoff region, there can be many reasons for the incoherency in the harmonic spectrum. The complete consistency between results of different approaches might be unattainable, and it might be reasonable to expect deviation in the calculated spectrum from other methods. Among the possible inconsistency reasons, we could imply the choice of absorption boundaries as a crucial role in lowering the needed box sizes and the inherent differences between dissimilar numerical techniques. It might be the case that the applied mask function Eq. (2.42) is not efficient for reducing the physical box size, and consequently, the number of used static coherent states is not enough to cover the whole space. In Sec. 4.3, we would discuss a more efficient absorber for investigating HHG in the basis of optimized Gaussian basis sets.

2.3.2 Single attosecond pulse generation in 3D H_2^+

Finally, to evaluate the SCS approach in simulations of more complex laser-induced scenarios, the single isolated attosecond pulse (SAP) generation is investigated in H_2^+ using the well-known polarization gating technique [79]. Such a polarization gate is generated without spatial filtering in the central part of the pulse by superposing two left ($-$) and right-hand ($+$) circularly polarized Gaussian pulses propagated in the z direction

$$\mathbf{E}_{\pm}(t) = E_0\, e^{-2\ln 2((t-t_d/2)/\tau_p)^2}(\cos(\omega t+\phi)\hat{x} \pm \sin(\omega t+\phi)\hat{y}) \tag{2.43}$$

in which E_0, t_d, τ_p, ω and ϕ are the field amplitude, time delay between two left ($-$) and right-hand ($+$) circularly polarized pulses, the full width at half maximum (FWHM) of the

the Gaussian shaped pulse, the carrier frequency and the carrier-envelope phase, respectively.

Having computed the $\alpha = x, y$ component of the dipole acceleration $\mathbf{A}(t)$ via Eq. (2.39), the profile of the attosecond pulse for each direction is obtainable superposing different harmonic orders [80]

$$I_\alpha(t) = \left| \sum_q a_\alpha(q) e^{iq\omega t} \right|^2 \tag{2.44}$$

where

$$a_\alpha(q) = \int a_\alpha(t) e^{-iqwt} \mathrm{d}t. \tag{2.45}$$

The time-frequency profiles of the high harmonics $w(\omega, t)$ are obtained via a Morlet wavelet transform of the time-dependent dipole acceleration

$$w(\omega, t) = \sqrt{\frac{\omega}{\pi^{\frac{1}{2}}\sigma}} \int_{-\infty}^{\infty} a_\alpha(t') e^{-i\omega(t'-t)} e^{-\frac{\omega^2(t'-t)^2}{2\sigma^2}} \mathrm{d}t' \tag{2.46}$$

where we set the Gaussian width $\sigma = 2\pi$ in this work.

In order to study how SAP is generated in H_2^+ at $R = 3$ a.u. using SCS, the system is simulated in the presence of a 800 nm 10-cycle laser field which has a polarization gating in the middle of the pulse. Such laser field is formed by combining two 8-cycle left and right-hand circularly polarized Gaussian pulses with both time delay t_d and FWHM of the Gaussian envelope τ_p equal to 2 cycles (i.e., 5.33702 fs or 220.64 a.u.) and the intensity of $I = 3 \times 10^{14}$ W/cm^2 for $\phi = 0$ and $\phi = \pi/2$ similarly to [80].

In Fig. 2.11, we have illustrated the SAP achieved from the SCS approach using the polarization gating technique for carrier envelop phase $\phi = 0$ (left panel) and $\phi = \pi/2$ (right panel). The simulation results in Fig. 2.11 obtained by averaging the expectation value of the acceleration of the single electron along the x and the y directions over 40 different random simulations (each contains a total number of 12000 CSs = 3000 internal CSs + 9000 external CSs). In the first row of Fig. 2.11 we plot the x and the y components of 10-cycle laser pulses for carrier envelope phases $\phi = 0$ (left) and $\phi = \pi/2$ (right). In the second row of Fig. 2.11 we have depicted the profile of the SAP pulse generated from high-order harmonic spectrum of H_2^+ for carrier envelope phases $\phi = 0$ (left) and $\phi = \pi/2$ (right) both in the x and the y directions. The x and the y components of the SAP are created by superposing the the 30th to the 50th orders of plateau harmonics. The third row of Fig. 2.11 delineates the absolute squared of the corresponding Morlet wavelet time profiles in the x direction.

As it is apparent, at the central part of both fields (Fig. 2.11a and Fig. 2.11d)) which are defined as polarization gate, the y component $E_y(t)$ is suppressed and consequently ellipticity of both pulses is changed from circular to linear. Therefore the x component of the pulse $E_x(t)$ becomes the main driving field and hence at the central portion of both pulses, isolated attosecond pulse is generated. This conclusion is in agreement with extremely low intensity taps generated in the y direction for both $\phi = 0$ (Fig. 2.11b) and $\phi = \pi/2$ (Fig.

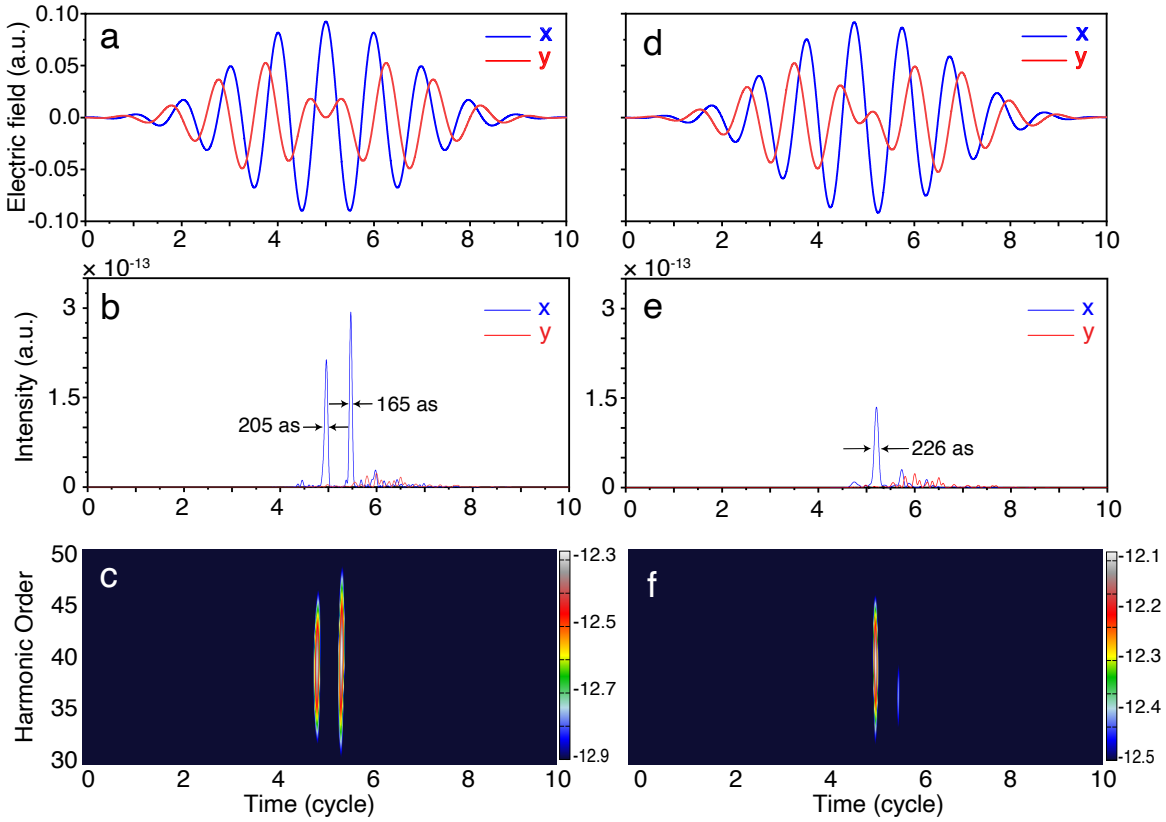

Figure 2.11 Single isolated attosecond pulse generation. Left panel (a-c) for carrier envelop phase $\phi = 0$: and right panel (d-f) for carrier envelop phase $\phi = \frac{\pi}{2}$. The first row (a,d) plots x (blue) and y (red) components of 10-cycle electric field constructed by combining two 8-cycle left and right-hand circularly polarized Gaussian pulses with both time delay t_d and FWHM τ_p equal to 2 cycles and $I = 3 \times 10^{14}$ W/cm^2. The second row (b,e) depicts isolated attosecond pulse from H_2^+ in the x (blue-colored) and the y (red-colored) directions. Since at the gate both fields are primarily polarized in the x direction, the generated pulse amplitudes in the y direction are significantly weaker than their corresponding x counterparts. The last row (c,f) illustrates absolute squared of the corresponding Morlet wavelet time-frequency profiles in the x direction.

2.11e). In the x direction, for the laser pulse with $\phi = 0$, two pulses are generated with a comparable intensity (with duration of 165 as and 205 as), while for the case of $\phi = \pi/2$, only one pulse with a comparable intensity (with duration of 226 as) is left.

3 Adaptive Gaussian basis sets for time-independent problems

In the previous chapter, to study the HHG in H_2^+ (Sec. 2.3.1) we used 8000 random CSs in a single simulation, where for the SAP in Sec. 2.3.2 we used 12000 CSs. Even employing a high number of CSs, we have witnessed that static coherent states were not completely successful in describing HHG of H_2^+ exposed to intense laser fields. The question arises: should we use an even higher number of basis functions to accurately capture the physics behind such laser-induced phenomena? Is there a more elegant and cost-effective approach in which a minimal basis set is constructed and guided to the regions where they are most needed?

In this chapter, as an essential and preliminary step for the time-dependent studies (Chapter 4), we seek to address these questions by introducing an optimization algorithm that quickly finds the optimum configuration of the basis sets and represents the time-independent wave-function of a desired electronic state of the system with high accuracy. The goal is to keep the number of basis states as low as possible and obtain highly accurate values for the electronic state energies of the system.

For the sake of simplicity and because of the fact that coherent states are complex Gaussian wave packets, in Eq. (B.6), we chose s-type Gaussian type orbitals (GTOs) $\mathcal{G}_i^s(\mathbf{r}, \mathbf{r}_i, \alpha_i) = e^{-\alpha_i(\mathbf{r}-\mathbf{r}_i)^2}$ to construct a basis. Functions that resemble hydrogen atomic orbitals, Slater type orbitals (STOs), might seem to be a better option as they correctly describe the cusp at the nuclei, and the asymptotic long-range behavior of the wave-function. However, the GTOs introduced by Boys [81] which are the most common basis sets in quantum chemistry for performing numerical calculations on atoms and molecules, have the advantage of solving molecular integrals analytically and consequently being far less computationally expensive than the STOs.

This work solely represents the wave function on the basis of spherically symmetric s-type GTOs. For optimizing the exponent α_i and the center-position $\mathbf{r}_i$ of each s-type GTO, we employ the first-order Taylor expansion. Doing so, as explained in Secs. 3.1.2 and 3.1.3, during the optimization process, we require the first derivatives of each s-type GTO with respect to the exponent and the center-position. The first derivative with respect to the exponent corresponds to an s-type GTO with the shifted position squared, $(\mathbf{r} - \mathbf{r}_i)^2$, as the

prefactor. This terms is nothing but the summation of three Cartesian d-type GTOs. The first derivative with respect to the position in each direction results in an s-type GTO multiplied by the shifted position in that direction. These terms are simply p-type GTOs along the x, y, and z coordinates.

Many quantum chemistry packages that work with the Cartesian GTOs can provide the Hamiltonian and the overlap matrix elements between different type of GTOs. That is what we need during the optimization procedure presented in this work. It means that our optimization approach has the potential to be integrated into the standard quantum chemistry packages where the variational principle is the primary optimization method.

This chapter is organized as follows: In Sec. 3.1, we briefly explain how one can calculate an electronic state of a quantum system with a high precision using the s-type Cartesian GTOs (Sec. 3.1.1). Next, we discuss the main steps of our developed optimization algorithm in more details: optimization of the exponents of the s-type GTOs in Sec. 3.1.2 and their positions in Sec. 3.1.3. Then, in Sec. 3.2, we apply the introduced optimization technique to different quantum systems. In this chapter, our systems of interest are: 1D harmonic oscillator (Sec. 3.2.1), 1D Morse oscillator (Sec. 3.2.2), 1D Hydrogen atom (Sec. 3.2.3), 1D Hydrogen molecular ion H_2^+ (Sec. 3.2.4), 3D Hydrogen atom (Sec. 3.2.5), and 3D Hydrogen molecular ion H_2^+ (Sec. 3.2.6).

3.1 Theory: accurate computation of a desired electronic state

We represent the wave function of the quantum system as a superposition of N s-type GTOs $\mathcal{G}_i^s(\mathbf{r}, \mathbf{r}_i, \alpha_i) = e^{-\alpha_i(\mathbf{r}-\mathbf{r}_i)^2}$

$$\psi(\mathbf{r}) = \sum_{i=1}^{N} D_i \mathcal{G}_i^s(\mathbf{r}, \mathbf{r}_i, \alpha_i). \tag{3.1}$$

The coefficients D_i and the eigenenergies are calculated by solving the generalized eigenvalue problem (GEVP) of the Schrödinger equation, $\mathrm{HD} = \mathrm{E}\Omega\mathrm{D}$, where H and Ω, respectively are the Hamiltonian and overlap matrices in the basis of GTOs.

As motivated before, our objective is to find the optimum exponents α_i as well as the optimum center-positions $\mathbf{r}_i$ of a set of the s-type GTOs in such a way that using a minimal number of basis functions we reach a high accuracy for the electronic state energy of the system.

To do so, as described in Fig. 3.1, we have developed a three-step iterative optimization scheme: initially, using only the s-type GTOs, the system's wave function is computed. In the second step, explained in Sec. 3.1.2, having added an equal number of auxiliary d-type GTOs to the s-type ones, we re-calculate the wave function. Doing so, we correct all the exponents of the s-type GTOs (Δ_i). In the last step, described in Sec. 3.1.3, after updating the exponents of the s-type GTOs, we re-compute the wave function by implementing a

set of auxiliary p-type GTOs along x, y, and z directions with the same exponents and center-positions as the s-type ones. Accordingly, corrections for the center positions of the s-type GTOs ($\boldsymbol{\delta}_i$) are evaluated and applied. This procedure is iterated until the desired accuracy for an electronic state energy of the system is obtained.

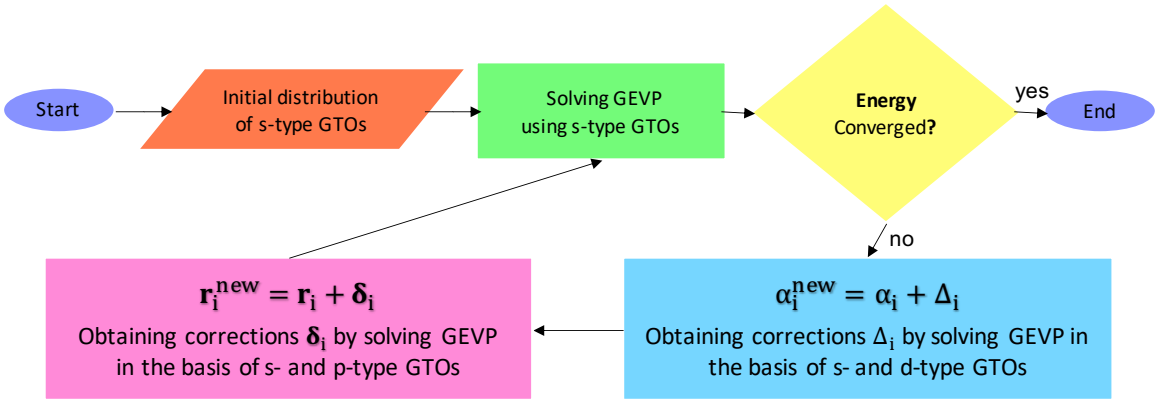

Figure 3.1 Our proposed optimization algorithm for s-type Gaussian basis sets.

3.1.1 Cartesian Gaussian type orbitals (GTOs)

GTOs, unlike STOs, are separable in the Cartesian coordinates. The **Gaussian product rule** upon which the product of two Gaussians centered at $\mathbf{A}$, and $\mathbf{B}$ is itself a single Gaussian centered at $\mathbf{C} = \frac{\alpha\mathbf{A}+\beta\mathbf{B}}{\alpha+\beta}$:

$$\exp\left(-\alpha(\mathbf{r}-\mathbf{A})^2\right)\exp\left(-\beta(\mathbf{r}-\mathbf{B})^2\right) = \exp\left(-\frac{\alpha\beta}{\alpha+\beta}(\mathbf{A}-\mathbf{B})^2\right)\exp\left(-(\alpha+\beta)(\mathbf{r}-\mathbf{C})^2\right), \tag{3.2}$$

and the separability of the Gaussians in Cartesian coordinates greatly simplify the atomic and molecular integrals.

The general form for **3D Cartesian GTOs** [82] reads

$$\mathcal{G}_i^{\boldsymbol{m}}(\mathbf{r},\mathbf{r}_i,\alpha_i) = \mathcal{N}_i^{\boldsymbol{m}}(x-x_i)^{m_x}(y-y_i)^{m_y}(z-z_i)^{m_z}\exp\left(-\alpha_i\left((x-x_i)^2+(y-y_i)^2+(z-z_i)^2\right)\right). \tag{3.3}$$

Solving $\int \mathcal{G}_i^{\boldsymbol{m}}(\mathbf{r},\mathbf{r}_i,\alpha_i)\mathcal{G}_i^{\boldsymbol{m}}(\mathbf{r},\mathbf{r}_i,\alpha_i)\mathrm{d}\mathbf{r} \equiv 1$, for the normalization factors of real-parameter GTOs ($\mathcal{N}_i^{\boldsymbol{m}}$), one can verify that

$$\mathcal{N}_i^{\boldsymbol{m}} = \left(\frac{2\alpha_i}{\pi}\right)^{3/4}(4\alpha_i)^{\frac{l_m}{2}}\left[(2m_x-1)!!(2m_y-1)!!(2m_z-1)!!\right]^{-1/2}, \tag{3.4}$$

where $(2m-1)!! = (2m-1)\cdot(2m-3)\cdots 5\cdot 3\cdot 1$. Moreover, in Eqs. (3.3) and (3.4), $\boldsymbol{m} = m_x\hat{x}+m_y\hat{y}+m_z\hat{z}$, and $l_m = m_x+m_y+m_z$ defines the angular momentum of the basis functions. $l_m = 0$ leads to the 3D Cartesian s-type GTOs with the spherical symmetry,

$$\mathcal{G}_i^{s}(\mathbf{r},\mathbf{r}_i,\alpha_i) = \mathcal{N}_i^{s}\exp\left(-\alpha_i\left((x-x_i)^2+(y-y_i)^2+(z-z_i)^2\right)\right), \tag{3.5}$$

while putting $l_m = 1$, we have three different options for the 3D Cartesian p-type GTOs possessing axial symmetry. Considering $l_m = 2$ one has six different possibilities for the 3D Cartesian d-type GTOs. As mentioned before, the first derivative of the s-type GTO with respect to the exponent α_i corresponds to a linear combination of three Cartesian d-type GTOs, $\mathcal{G}_i^{d_x}$ ($m_x = 2$), $\mathcal{G}_i^{d_y}$ ($m_y = 2$), and $\mathcal{G}_i^{d_z}$ ($m_z = 2$),

$$\mathcal{G}_i^d(\mathbf{r}, \mathbf{r}_i, \alpha_i) = \mathcal{N}_i^d\big((x - x_i)^2 + (y - y_i)^2 + (z - z_i)^2\big) \exp\big(-\alpha_i(\mathbf{r} - \mathbf{r}_i)^2\big). \tag{3.6}$$

The resulting function which possesses spherical symmetry, Eq. (3.6), is actually an s-type GTO. However, to distinguish it from a normal s-type GTO, Eq. (3.5), we call it d-type GTO in this work. Using Eq. (C.9), it is straightforward to verify that $\mathcal{N}_i^d = \frac{4\alpha_i}{\sqrt{15}}\big(\frac{2\alpha_i}{\pi}\big)^{3/4}$.

Reducing the 3D forms to 1D, for **1D Cartesian GTOs** we get

$$\mathcal{G}_i^m(x, x_i, \alpha_i) = \mathcal{N}_i^m(x - x_i)^m \exp\big(-\alpha_i(x - x_i)^2\big), \tag{3.7}$$

where the normalization factor $\mathcal{N}_i^m$ reads

$$\mathcal{N}_i^m = \left(\frac{2\alpha_i}{\pi}\right)^{1/4} (4\alpha_i)^{\frac{m}{2}} [(2m-1)!!]^{-1/2}. \tag{3.8}$$

Although the concept of the angular momentum is irrelevant in 1D, for the sake of consistency, we call the Gaussian functions corresponding to $m = 0$, $m = 1$, and $m = 2$ as 1D s-type GTOs, 1D p-type GTOs, and 1D d-type GTOs, respectively.

GTOs are not orthogonal, and some of them may become linearly dependent if their overlaps get too large. This causes the overlap matrix to lose its positive definiteness. Consequently, the GEVP can no longer be numerically solved. Since our procedure freely optimizes the s-type GTOs, this problem can be sometimes circumvented by adapting the correction percentage parameters, h_α Eq. (3.21a), and $h_\mathbf{r}$ Eq. (3.21b), to values smaller than one. From a numerical point of view, the mentioned problem occurs more frequently using unnormalized GTOs.

Normalized GTOs are only applicable to time-independent scenarios, and somewhat stabilize the possible numerical issues that one can get by leaving the normalization procedure to the GEVP solvers. For the time-dependent scenarios in Chapter 4, however, the GTOs would acquire complex parameters and using the normalization factors $\mathcal{N}_i^m$ for the complex-parameter s-type GTOs violates the complex differentiability condition which is essential to our optimization algorithm. To tackle this problem, we have to work with the unnormalized GTOs ($\mathcal{N}_i^m = 1$) and leave the normalization to the GEVP solvers. Hence, we use unnormalized GTOs unless mentioned otherwise.

3.1.2 Optimizing the exponents of s-type GTOs

To optimize exponents of s-type GTOs, as described in the second step of our optimization scheme in Fig. 3.1, we represent the wave function of the system as a superposition of s-type GTOs with slightly shifted exponents $\alpha_i + \Delta_i$

$$\psi(\mathbf{r}) = \sum_{i=1}^{N} D_i \mathcal{G}_i^s(\mathbf{r}, \mathbf{r}_i, \alpha_i + \Delta_i). \tag{3.9}$$

First-order Taylor expansion of $\mathcal{G}_i^s(\mathbf{r}, \mathbf{r}_i, \alpha_i + \Delta_i)$ around the exponent correction Δ_i leads to a linear combination of one s-type GTO $\mathcal{G}_i^s(\mathbf{r}, \mathbf{r}_i, \alpha_i)$, and a function which can be written as the d-type GTO $\mathcal{G}_i^d(\mathbf{r}, \mathbf{r}_i, \alpha_i)$ introduced in Eq. (3.6),

$$\mathcal{G}_i^s(\mathbf{r}, \mathbf{r}_i, \alpha_i + \Delta_i) = (1 + \Delta_i \mathbb{N}_i^s)\mathcal{G}_i^s(\mathbf{r}, \mathbf{r}_i, \alpha_i) - \Delta_i \mathbb{N}_i^d \mathcal{G}_i^d(\mathbf{r}, \mathbf{r}_i, \alpha_i). \tag{3.10}$$

Hence, substituting Eq. (3.10) in Eq. (3.9), the wave function becomes a superposition of $2N$ GTOs consisting of N s-type and N d-type GTOs,

$$\psi(\mathbf{r}) = \sum_{i=1}^{N} D_i^s \mathcal{G}_i^s(\mathbf{r}, \mathbf{r}_i, \alpha_i) + \sum_{i=N+1}^{2N} D_i^d \mathcal{G}_i^d(\mathbf{r}, \mathbf{r}_i, \alpha_i), \tag{3.11}$$

where $D_i^s = D_i(1 + \Delta_i \mathbb{N}_i^s)$, and $D_i^d = -D_i \Delta_i \mathbb{N}_i^d$. Using the normalized GTOs, one can verify that

$$\text{3D GTOs} \begin{cases} \mathbb{N}_i^s = \frac{3}{4\alpha_i} \\ \mathbb{N}_i^d = \frac{\sqrt{15}}{4\alpha_i} \end{cases}, \qquad \text{1D GTOs} \begin{cases} \mathbb{N}_i^s = \frac{1}{4\alpha_i} \\ \mathbb{N}_i^d = \frac{\sqrt{3}}{4\alpha_i} \end{cases}, \tag{3.12}$$

while employing unnormalized GTOs, one can get

$$\mathbb{N}_i^s = 0 \qquad , \qquad \mathbb{N}_i^d = 1. \tag{3.13}$$

Having evaluated the elements of Hamiltonian (H) and overlap (Ω) matrices over s- and d-type GTOs with the help of Appendix C, we compute the coefficients D_i^s and D_i^d solving the GEVP of the Schrödinger equation

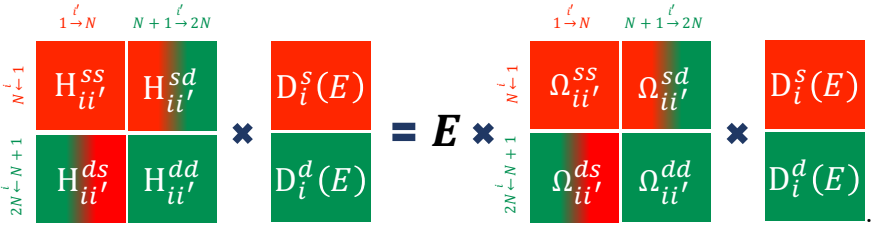

Accordingly, the exponent corrections Δ_i are calculated with

$$\Delta_i = -\frac{1}{\mathbb{N}_i^d \frac{D_i^s}{D_i^d} + \mathbb{N}_i^s}. \tag{3.14}$$

3.1.3 Optimizing the center-positions of s-type GTOs

Next, to evaluate the center-position corrections $\boldsymbol{\delta}_i$, as the last step of our optimization scheme, we represent the wave function of the systems as a superposition of exponent-updated s-type GTOs with slightly shifted center-positions $\mathbf{r}_i + \boldsymbol{\delta}_i$

$$\psi(\mathbf{r}) = \sum_{i=1}^{N} D_i \mathcal{G}_i^s(\mathbf{r}, \mathbf{r}_i + \boldsymbol{\delta}_i, \alpha_i). \tag{3.15}$$

First-order Taylor expansion of $\mathcal{G}_i^s(\mathbf{r}, \mathbf{r}_i + \boldsymbol{\delta}_i, \alpha_i)$ around the center-position correction $\boldsymbol{\delta}_i$ leads to a linear combination of one s-type GTO $\mathcal{G}_i^s(\mathbf{r}, \mathbf{r}_i, \alpha_i)$, and a set of functions which can be written as the p-type GTOs $\mathcal{G}_i^p(\mathbf{r}, \mathbf{r}_i, \alpha_i)$ along the x, y, and z coordinates,

$$\mathcal{G}_i^s(\mathbf{r}, \mathbf{r}_i + \boldsymbol{\delta}_i, \alpha_i) = \mathcal{G}_i^s(\mathbf{r}, \mathbf{r}_i, \alpha_i) + \mathbb{N}_i^p \sum_{j=x,y,z} \delta_i^j \mathcal{G}_i^{p_j}(\mathbf{r}, \mathbf{r}_i, \alpha_i). \tag{3.16}$$

Accordingly, substituting Eq. (3.16) in Eq. (3.15), the wave function becomes a superposition of $4N$ GTOs consisting of N s-type and $3N$ p-type GTOs,

$$\begin{aligned}\psi(\mathbf{r}) = &\sum_{i=1}^{N} D_i^s \mathcal{G}_i^s(\mathbf{r}, \mathbf{r}_i, \alpha_i) + \sum_{i=N+1}^{2N} D_i^{p_x} \mathcal{G}_i^{p_x}(\mathbf{r}, \mathbf{r}_i, \alpha_i) \\ &+ \sum_{i=2N+1}^{3N} D_i^{p_y} \mathcal{G}_i^{p_y}(\mathbf{r}, \mathbf{r}_i, \alpha_i) + \sum_{i=3N+1}^{4N} D_i^{p_z} \mathcal{G}_i^{p_z}(\mathbf{r}, \mathbf{r}_i, \alpha_i),\end{aligned} \tag{3.17}$$

where $D_i^s = D_i$, and $D_i^{p_j} = D_i \mathbb{N}_i^p \delta_i^j$. For the normalized and the unnormalized GTOs we respectively get

$$\mathbb{N}_i^p = \sqrt{\alpha_i}, \tag{3.18}$$

$$\mathbb{N}_i^p = 2\alpha_i. \tag{3.19}$$

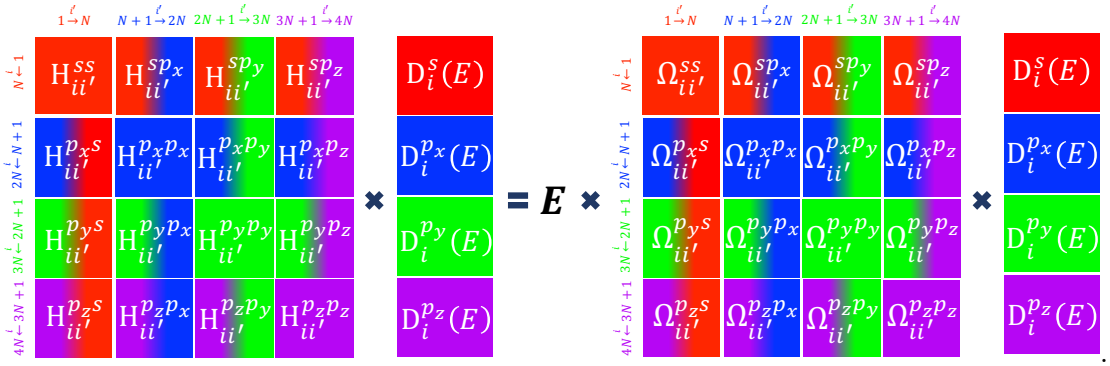

Employing Appendix C, we evaluate the Hamiltonian (H) and the overlap (Ω) matrix elements over s- and p-type GTOs. Subsequently, solving the GEVP of the Schrödinger equation gives us the coefficients D_i^s, $D_i^{p_x}$, $D_i^{p_y}$ and $D_i^{p_z}$. Then, we compute the center-

position corrections δ_i^j using

$$\delta_i^j = \frac{D_i^{p_j}}{\mathbb{N}_i^p D_i^s}. \tag{3.20}$$

3.1.4 Handling large corrections

As we truncate the Taylor expansion after the first order in Eqs. (3.10), and (3.16), the coefficients D_i^d, and $D_i^{p_j}$ should be much smaller than their corresponding coefficients D_i^s to ensure reasonable exponent corrections Δ_i, and center-position corrections δ_i^j. Otherwise, the corrections might get too large and bring about numerical problems. Updating exponents and center-positions of GTOs, to tame possible numerical issues that primarily take place in the time-dependent scenarios, we apply an adapted percentage $(h_\alpha, h_{\mathbf{r}} \leq 1)$ of the computed exponent Δ_i and center-position $\boldsymbol{\delta}_i$ corrections

$$\alpha_i = \alpha_i + h_\alpha \Delta_i, \tag{3.21a}$$

$$\mathbf{r}_i = \mathbf{r}_i + h_{\mathbf{r}} \boldsymbol{\delta}_i. \tag{3.21b}$$

3.2 Systems of interest

In this section, we will see how our optimization approach performs in finding the optimum configuration of minimal grids of s-type GTOs which accurately represent electronic state wave functions of the following 1D and 3D systems: 1D harmonic oscillator (Sec. 3.2.1), 1D Morse Potential (Sec. 3.2.2), 1D Hydrogen atom with soft-core potential (Sec. 3.2.3), 1D Hydrogen molecular ion H_2^+ with soft-core potential (Sec. 3.2.4), 3D Hydrogen atom (Sec. 3.2.5), and 3D Hydrogen molecular ion H_2^+ (Sec. 3.2.6).

Here, s-type GTOs are initially distributed equidistantly along the x axis between $-X_{max}$ and $+X_{max}$ with initial $\alpha = \alpha_{ini}$. Moreover, the correction parameters $h_\alpha = h_x$ are equal to one everywhere unless mentioned otherwise.

3.2.1 1D harmonic oscillator

We begin with the simplest system, the 1D harmonic oscillator

$$\mathrm{H} = -\frac{1}{2}\frac{\mathrm{d}^2}{\mathrm{d}x^2} + \frac{1}{2}kx^2, \tag{3.22a}$$

$$\mathrm{E}_m = \left(m + \frac{1}{2}\right)\omega, \tag{3.22b}$$

$$\psi_m(x) = \frac{1}{\sqrt{2^m m!}}\left(\frac{\omega}{\pi}\right)^{1/4} e^{-\frac{\omega x^2}{2}} \mathcal{H}_m\left(\sqrt{\omega}x\right), \tag{3.22c}$$

with eigenenergies E_m, and eigenfunctions ψ_m. From the Hermite polynomials,

$$\mathcal{H}_m(x) = (-1)^m e^{x^2} \frac{\mathrm{d}^m}{\mathrm{d}x^m}\left(e^{-x^2}\right), \tag{3.23}$$

the exact ground state wave-function $\psi_0(x)$ is easily verified to be a single s-type Gaussian. We consider the oscillator angular frequency $\omega = \sqrt{k} = 1$.

First, by optimizing s-type GTOs with respect to the ground state of the 1D harmonic oscillator, using the associated coefficients D_i for determining the corrections, we have examined how many s-type GTOs are needed to reach the accuracy of 10^{-10} for all the first five electronic energies of the system. Details are reported in Table 3.1.

As explained in Table 3.1, expectedly, just $N = 1$ optimized s-type GTO is sufficient to get a highly accurate energy for the ground state while after the full optimization, allowing the single Gaussian to move, it still stays at $x = 0$. Note that only $N = 9$ optimized s-type GTOs are needed to reach an accuracy of 10^{-11} for the first three electronic states, whereas using the equidistant GTOs, as reported in [83], $N = 241$ s-type GTOs were necessary to reach the same accuracy. Based on our investigation, to obtain an accuracy of 10^{-10} for the first five electronic states, $N = 19$ optimized s-type GTOs are needed.

For $N = 15$, and $N = 19$ we have used the position correction parameters $h_x = 0.6$, and $h_x = 0.5$, respectively.

Table 3.1 1D harmonic oscillator: the ground state is represented by optimizing up to $N = 19$ s-type GTOs (distributed equidistantly between $-X_{max}$ and X_{max} with initial $\alpha = \alpha_{ini}$). The relative errors RE for the first five Eigenenergies E_i of the system are also listed. The fourth column gives the relative error for the ground state energies corresponding to the initial unoptimized basis sets. The fifth column provides the number of optimization iterations. The last column presents the computation time of each optimization procedure (performed on a Core i7-9700 Linux workstation).

N	α_{ini}	X_{max}	Initial RE(E_0)	no. iter	RE(E_0)	RE(E_1)	RE(E_2)	RE(E_3)	RE(E_4)	time (s)
1	1.0	0.0	2.5×10^{-1}	6	2.2×10^{-16}	4.9×10^{-5}	1	1	1	0.051
3	1.0	2.5	2.3×10^{-1}	8	0.0^*	1.9×10^{-4}	2.4×10^{-5}	1	1	0.052
5	1.0	2.5	1.0×10^{-2}	8	2.2×10^{-16}	7.4×10^{-5}	2.3×10^{-6}	1.3×10^{-2}	4.2×10^{-3}	0.052
7	2.0	2.5	1.4×10^{-3}	12	2.2×10^{-16}	1.5×10^{-7}	1.0×10^{-8}	3.0×10^{-5}	2.2×10^{-6}	0.055
9	3.0	2.5	1.4×10^{-4}	12	1.7×10^{-15}	5.1×10^{-11}	1.2×10^{-11}	1.3×10^{-9}	1.2×10^{-7}	0.058
11	3.0	3.0	3.7×10^{-5}	14	0.0^*	4.7×10^{-12}	1.4×10^{-11}	1.5×10^{-9}	4.2×10^{-9}	0.062
13	3.0	3.5	1.6×10^{-5}	10	1.1×10^{-16}	6.9×10^{-14}	2.7×10^{-12}	1.1×10^{-10}	3.8×10^{-9}	0.060
15	3.0	4.0	8.5×10^{-6}	12	3.3×10^{-15}	1.1×10^{-13}	1.9×10^{-12}	5.4×10^{-11}	9.8×10^{-10}	0.062
17	3.0	4.0	6.5×10^{-8}	7	1.9×10^{-15}	8.1×10^{-14}	7.0×10^{-13}	2.3×10^{-11}	6.7×10^{-10}	0.072
19	3.0	4.5	6.5×10^{-8}	7	9.9×10^{-16}	4.5×10^{-13}	1.3×10^{-12}	1.8×10^{-11}	2.6×10^{-10}	0.076

* RE $= 0.0$ means that the double precision machine accuracy is reached.

In Fig. 3.2 (a)-(c), we have plotted the initial and optimum configurations of s-type GTOs and their corresponding probability densities for $N = 5$, $N = 9$, and $N = 19$, respectively. In these figures, the left vertical axis is related to the ground state probability densities and the potential function, whereas the right vertical axis corresponds to the exponents of s-type GTOs. Furthermore, the error bars outline the coefficients $|D_i|$, i.e., the contribution of s-type GTOs in the wave function.

In Fig. 3.2 (a)-(c), the s-type GTOs located at the two ends of the optimized configurations do not represent the ground state wave function as their contributions to the ground state wave function are negligible. These s-type GTOs are essential for representing higher electronic state wave functions with a high precision. As one can conclude from the length of error bars, the middle ones, on the other hand, have the main contribution in describing the ground state wave function.

Moreover, for the mentioned grids of s-type GTOs, the iterative optimization procedures are delineated, respectively in Fig. 3.3 (a)-(c). In Figs. 3.2 and 3.3, it is worthwhile to note that both of the optimized center positions and the optimized exponents keep the symmetry $x \to -x$ during all optimization iterations. This symmetry is required by the potential. As can be seen in Fig. 3.3 (a) and (c), although the exponents of some of the s-type GTOs tend to increase in the first iteration, all of them end up having close exponents. Besides, the center-positions of s-type GTOs get closer to each other at the end.

Additionally, in Fig. 3.4 (a)-(c), we have depicted the resulting relative error convergence for the first five electronic state energies versus the number of optimization iterations. One can note in Fig. 3.4 (a)-(c) how our optimization approach substantially improves the accuracy of the first five electronic state energies in just a few iterations.

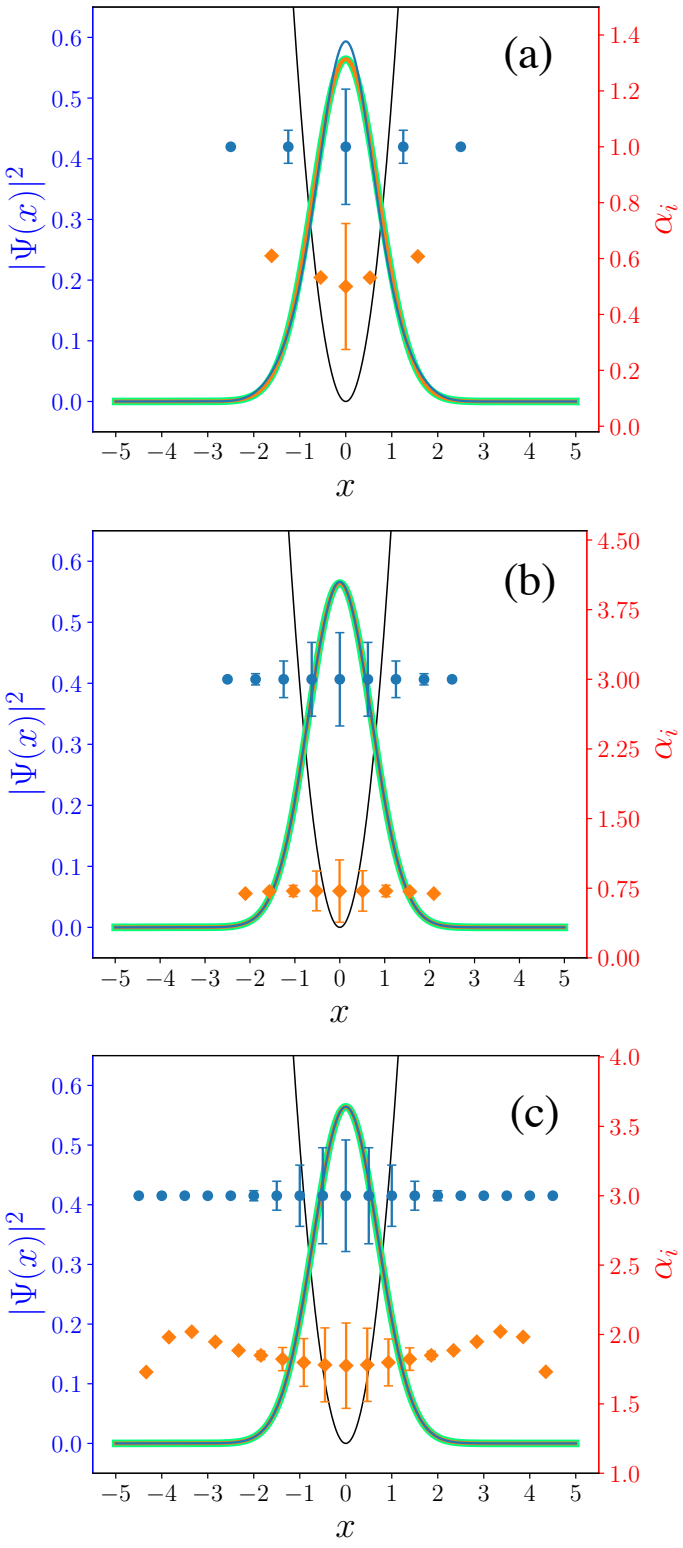

Figure 3.2 1D harmonic oscillator: initial (the blue-colored circles) versus optimum (the orange-colored diamonds) configurations of (a) $N = 5$, (b) $N = 9$, and (c) $N = 19$ s-type GTOs and their corresponding ground state probability densities. The left vertical axis corresponds to the probability densities as well as the potential function, while the right vertical axis is related to the exponents of s-type GTOs. Error bars depict the ground state associated coefficients $|D_i|$. The black, the blue, the orange, and the thick green lines show the potential shape, the initial probability density, the optimum probability density, and the exact probability density, respectively.

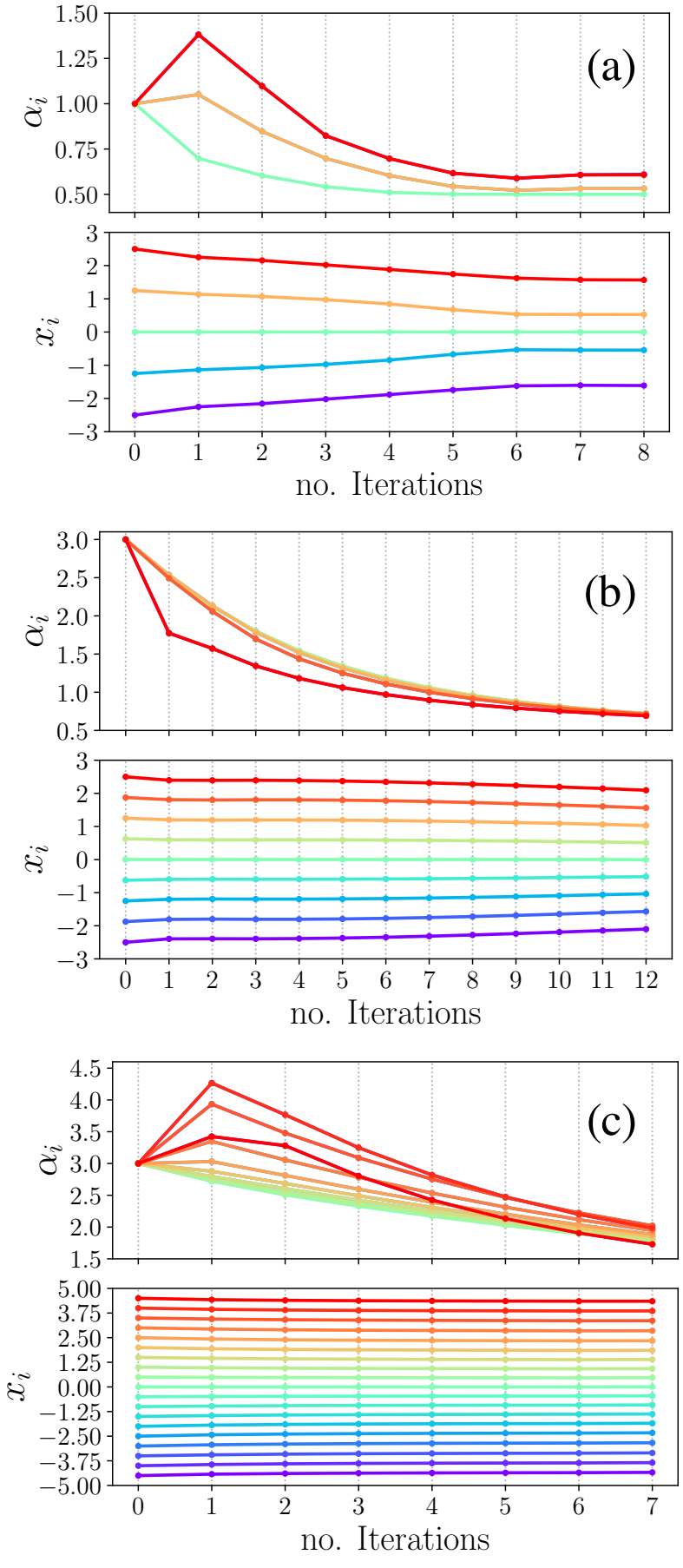

Figure 3.3 1D harmonic oscillator: the center-positions x_i, and the exponents α_i of (a) $N = 5$, (b) $N = 9$, and (c) $N = 19$ s-type GTOs that are iteratively optimized with respect to the ground state energy.

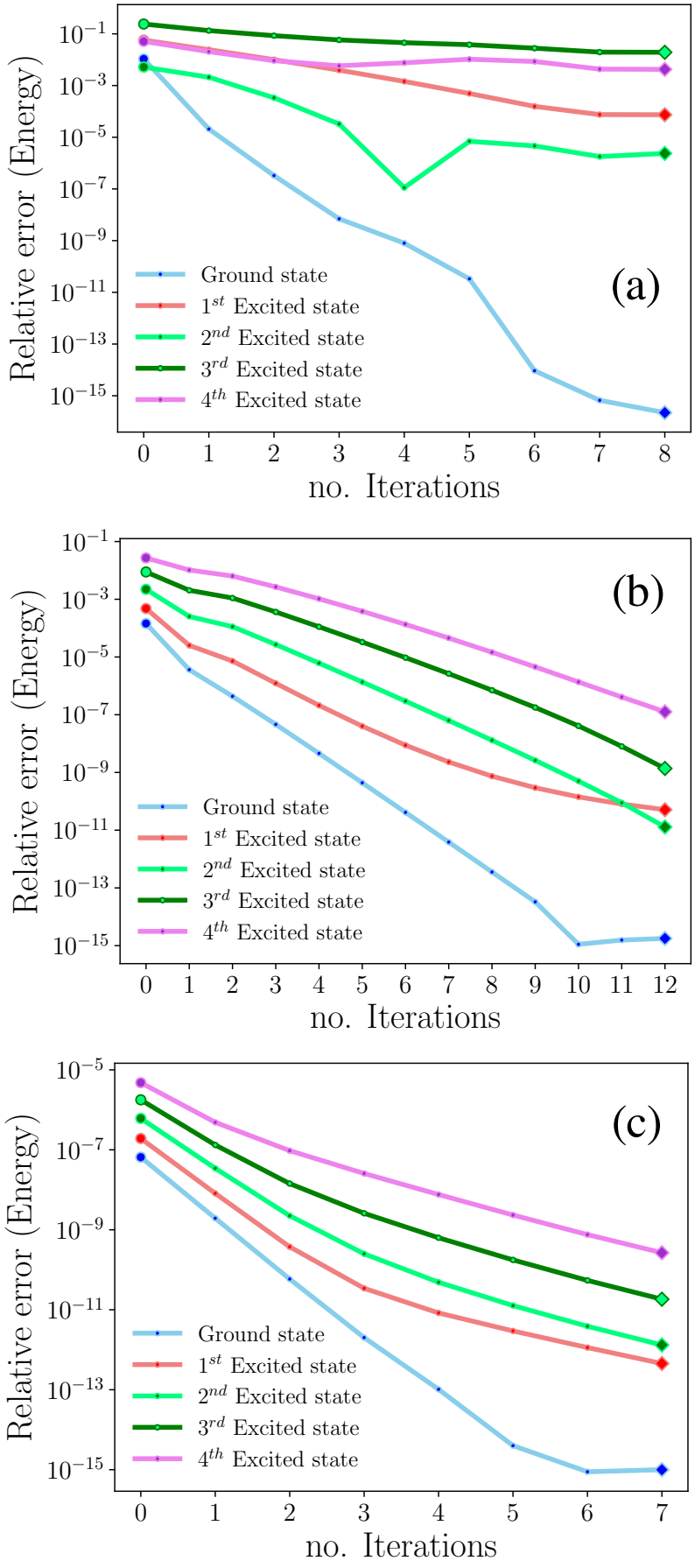

Figure 3.4 1D harmonic oscillator: the relative error of the first five electronic state energies are iteratively improved optimizing (a) $N = 5$, (b) $N = 9$, and (c) $N = 19$ s-type GTOs with respect to the ground state.

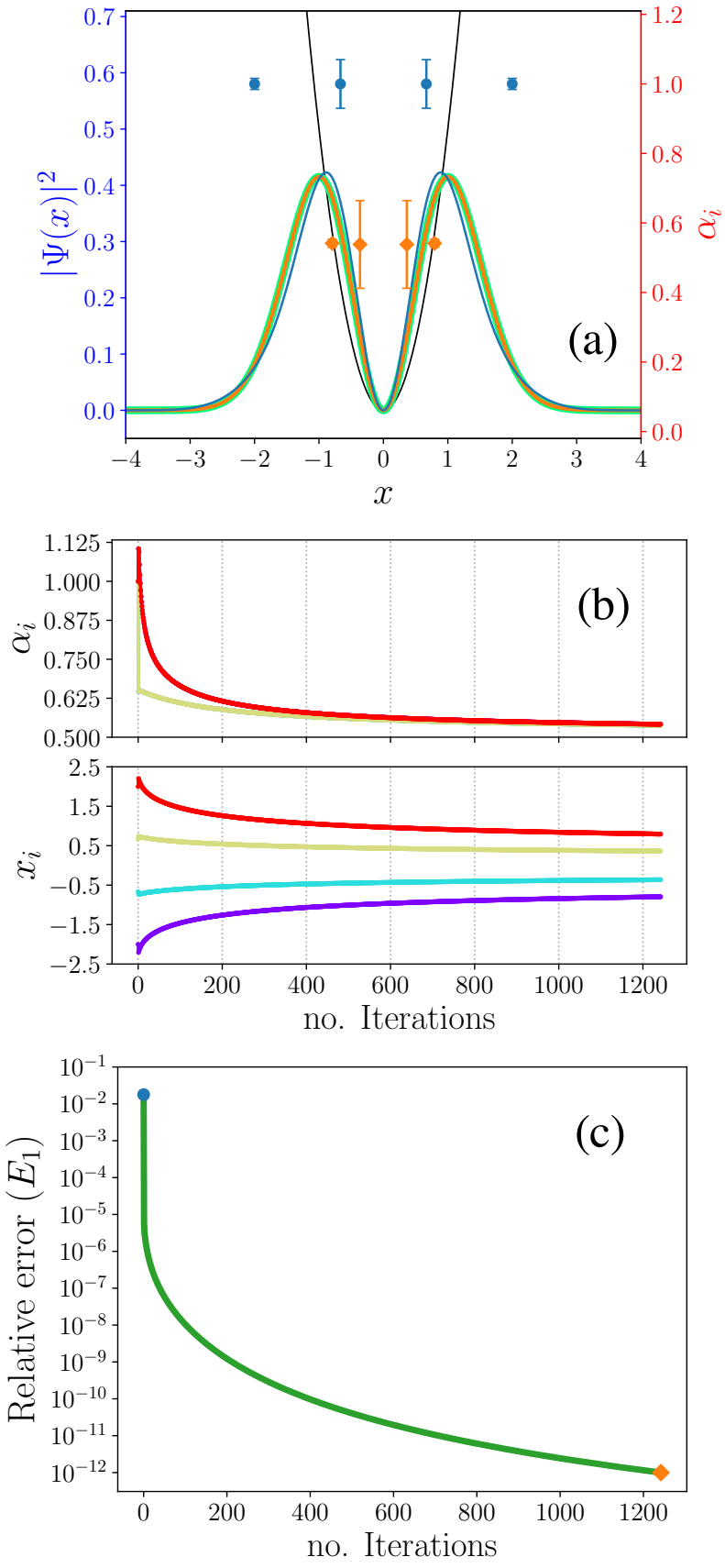

Figure 3.5 1D harmonic oscillator: (a) $N = 4$ equidistant s-type GTOs (blue-colored) are iteratively optimized (orange-colored) to specifically represent the first excited state wave function with a high precision. This figure shares similar properties as Fig. 3.2. (b) Iterative optimization of the center-positions x_i, and the exponents α_i. (c) The resulting relative error for the first excited state energy during the iterative optimization procedure.

Next, by optimizing s-type GTOs with respect to the first excited state, we show that $N = 4$ s-type GTOs are adequate for obtaining an accuracy better than 10^{-12} exclusively for the first excited state of the system. We have plotted in Fig. 3.5 (a), the initial and optimum configurations, their associated probability densities, and the potential shape, wherein error bars indicate the coefficients $|D_i|$. In addition, the iterative optimization procedure is depicted in Fig. 3.5 (b), while the relative error convergence of the first excited state energy is portrayed in Fig. 3.5 (c). For the first excited state, there is no need having a GTO on the center in the initial configuration. After the full optimization, none of the GTOs would end up around the center as well. As it is shown in Fig. 3.5 (a), this is simply because the first excited excited state wave function is zero on the center. In addition, the significant improvement of the first excited energy after 1200 iterations is noticeable in From Fig. 3.5 (c). We can conclude that the more s-type GTOs used the fewer number of iterations are needed for getting a comparable accuracy.

For the harmonic oscillator, no matter which electronic state is used for the optimization procedure, the optimum configuration is symmetric. i.e. the GTOs centered at opposite positions end up having the same exponents.

3.2.2 1D Morse Potential

In the next step, we apply our optimization algorithm to the 1D Morse oscillator

$$\mathrm{H} = -\frac{1}{2}\frac{\mathrm{d}^2}{\mathrm{d}x^2} + D_e(1 - e^{-ax})^2, \tag{3.24a}$$

$$\mathrm{E}_m = a\sqrt{2D_e}(m + \frac{1}{2}) - \frac{1}{2}a^2(m + \frac{1}{2})^2. \tag{3.24b}$$

Since this anharmonic potential explicitly includes the effects of bond breaking, in comparison with the quantum harmonic oscillator, it provides a better approximation for the vibrational structure of a diatomic molecule. The exact energies are given by E_m. Here, similar to [84], we have considered $D_e = 150$ (a.u.), and $a = 0.288$ (a.u.).

As depicted in Figs. 3.6 (a) and (b), we initially distribute $N = 5$ s-type GTOs equidistantly along the x axis with $X_{max} = 2.0$, and $\alpha_{ini} = 3.0$. This configuration produces a relative error of 1.53×10^{-2} for the ground state energy. As it is shown in Fig 3.6 (c), after optimizing the Gaussian basis set in 122 iterations, our procedure obtains the optimum configuration with a relative error better than 10^{-10} for the ground state energy. Since the Morse potential is not symmetric, in contrast to the quantum harmonic oscillator, the final configuration is also found to be not symmetric. As it can be seen in Fig. 3.6 (b), exponents of some GTOs are sharply increased during the first iterations. That is mainly due to the fact that the coefficients D_i associated with the s-type GTOs get much smaller than their auxiliary d-type counterparts. However, they ultimately find their best values as the center-positions are optimized.

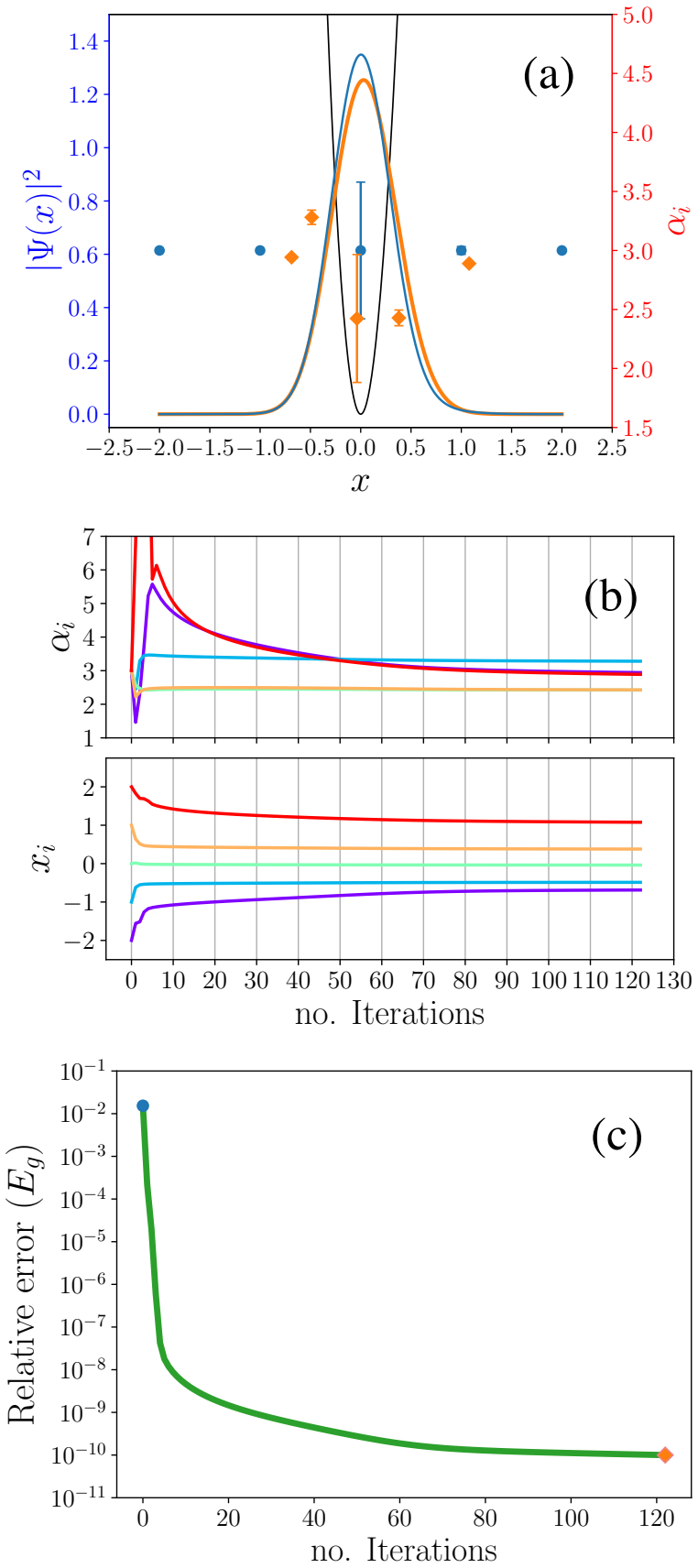

Figure 3.6 1D Morse oscillator: $N = 5$ equidistant s-type GTOs (blue-colored) are iteratively optimized (orange-colored) to accurately represent the ground state wave function. This figure shares similar properties as Fig. 3.2. (b) Iterative optimization of the center positions x_i, and the exponents α_i. (c) The resulting relative error for the ground state energy during the iterative optimization procedure.

3.2.3 1D Hydrogen atom with a soft-core potential

Now, we apply our optimization procedure to obtain a highly accurate ground state energy for the Hydrogen atom modeled by the following 1D soft-core Hamiltonian

$$\mathrm{H} = -\frac{1}{2}\frac{\mathrm{d}^2}{\mathrm{d}x^2} - \frac{1}{\sqrt{x^2+2}}, \tag{3.25a}$$

$$\psi_0(x) = 0.9748\left(1+\sqrt{x^2+2}\right)e^{-\sqrt{x^2+2}}[85], \tag{3.25b}$$

which gives rise to the exact 3D ground state energy ($E_0 = -0.5\ a.u.$).

For this system, in Figs. 3.8, 3.9 and 3.7, and Table 3.2, we show that our algorithm optimizes s-type GTOs no matter if the initial configuration is atomic-centered (even-tempered: $x_i = 0$, $\alpha_i = \alpha_{ini}\gamma^{k_i}$, $k_i = -\frac{n-1}{2}, \cdots, \frac{n-1}{2}$, $\alpha_{ini} = 0.35$, and $\gamma = 2$) or equidistantly distributed ($\alpha_{ini} = 5.0$, and $X_{max} = 5.0$).

Table 3.2 1D Hydrogen atom with a soft-core potential: representing the ground state by atomic and distributed s-type GTOs.

Configuration	h_α	h_x	Initial RE(E_0)	Optimum RE(E_0)	no. iter
9 Atomic	0.5	0.5	1.08×10^{-9}	8.67×10^{-13}	7
9 Distributed	0.5	0.5	1.74×10^{-1}	1.49×10^{-8}	247
19 Distributed	0.5	0.5	2.10×10^{-3}	3.14×10^{-13}	204

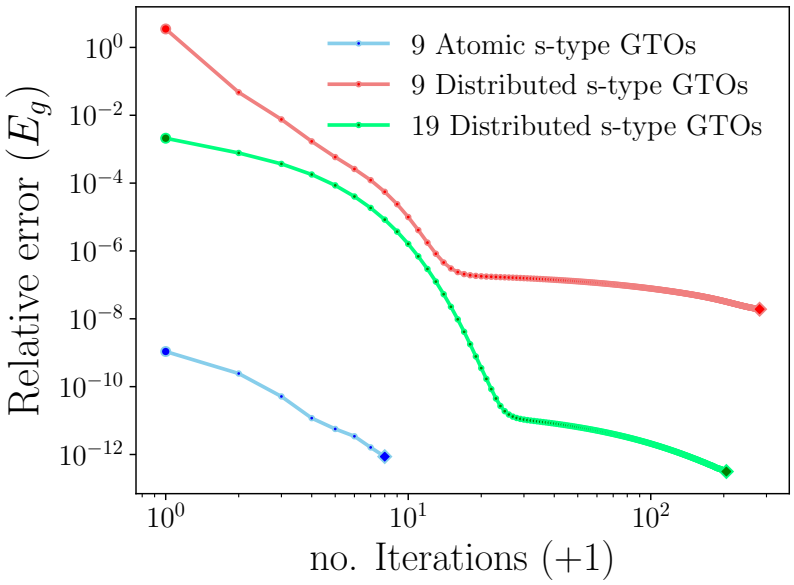

Figure 3.7 1D Hydrogen atom: iterative improvement of the ground state energy using (a) $N = 9$ atomic-centered (even-tempered), (b) $N = 9$ equidistantly distributed, and (c) $N = 19$ equidistantly distributed s-type GTOs being optimized with respect to the ground state.

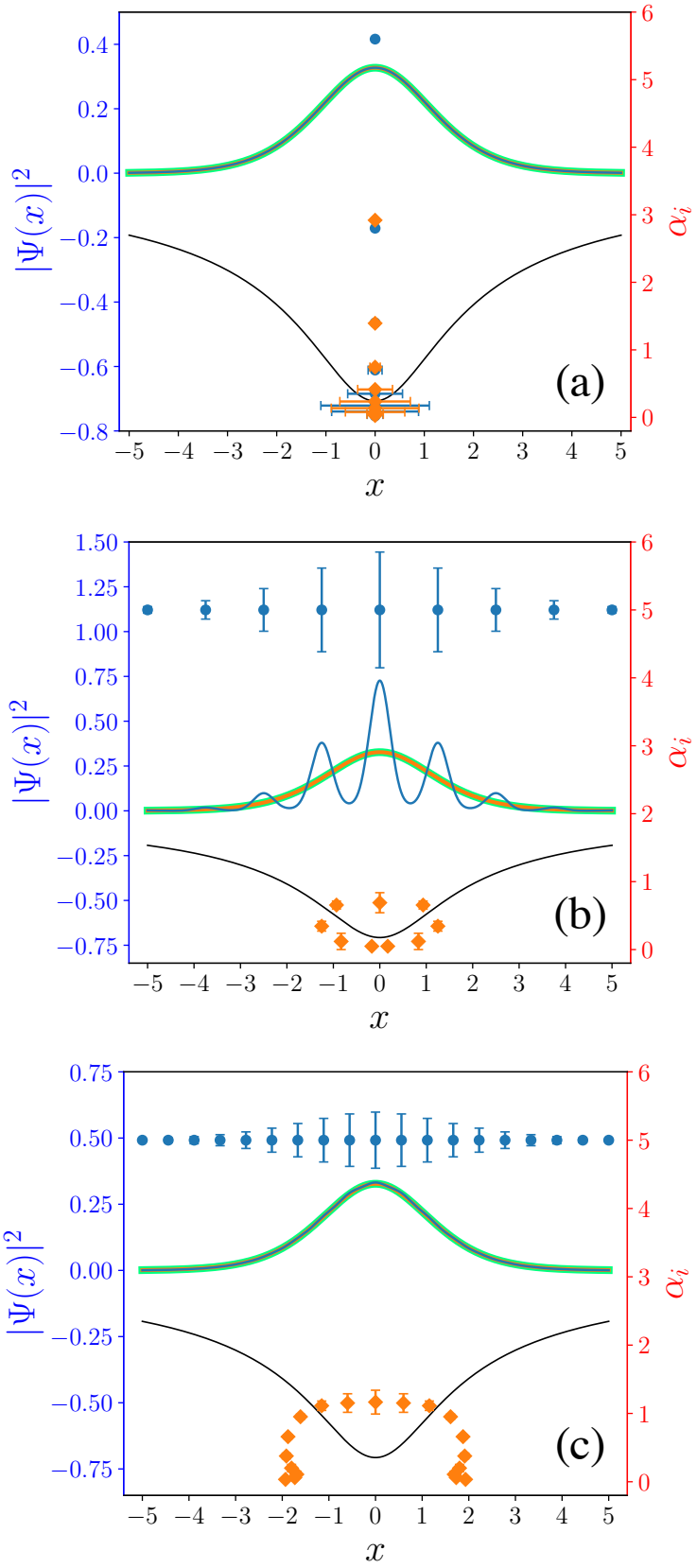

Figure 3.8 1D Hydrogen atom: (a) $N = 9$ atomic-centered (even-tempered), (b) $N = 9$ equidistantly distributed, and (c) $N = 19$ equidistantly distributed s-type GTOs (blue-colored) are iteratively optimized (orange-colored) to accurately represent the ground state wave function. These figures share similar properties as Fig. 3.2.

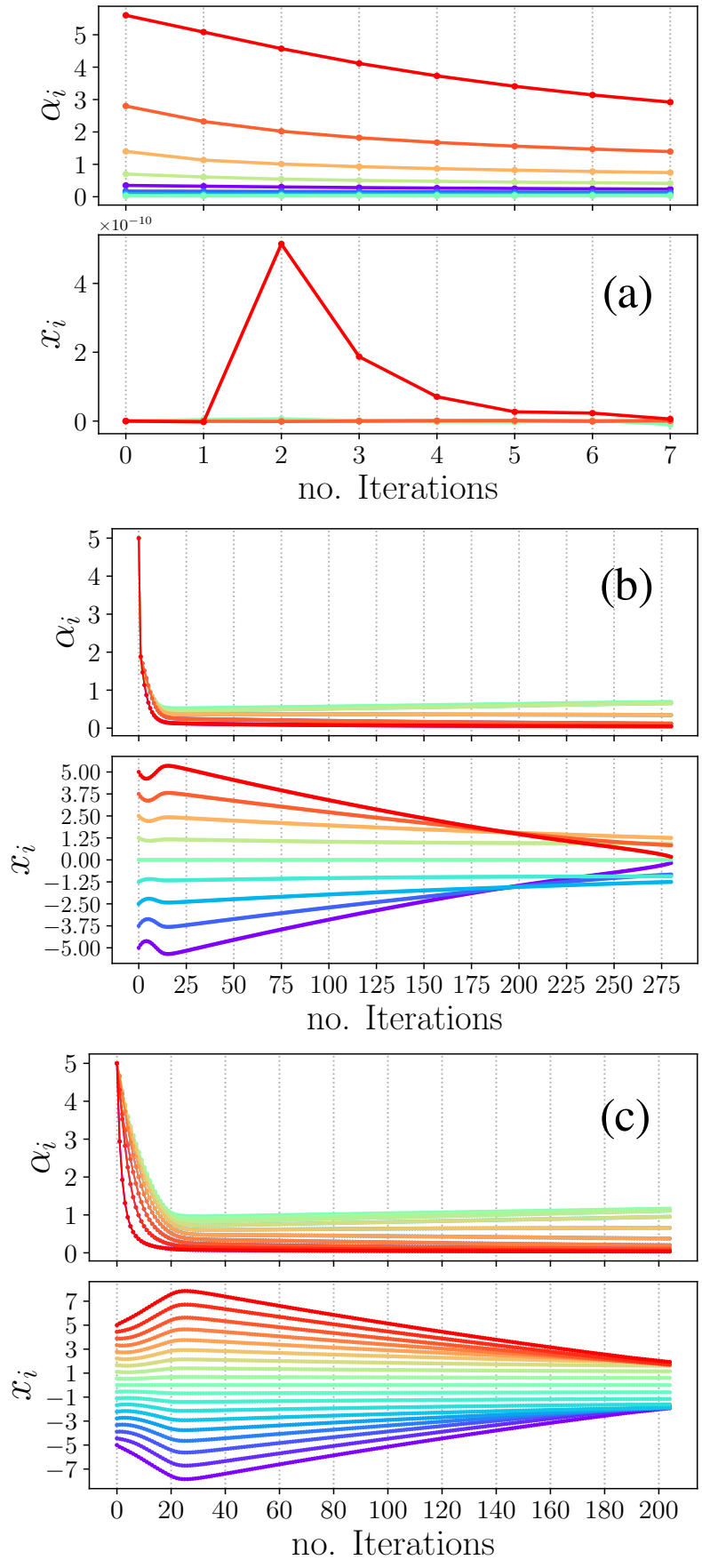

Figure 3.9 1D Hydrogen atom: the center-positions x_i, and the exponents α_i of (a) $N = 9$ atomic-centered (even-tempered), (b) $N = 9$ equidistantly distributed, and (c) $N = 19$ equidistantly distributed s-type GTOs that are iteratively optimized with respect to the ground state energy.

Atomic-centered s-type GTOs are found to be superior for representing the Hydrogen atom. Note from Table 3.2 and Fig. 3.7 that in contrast to the distributed GTOs, even the initial unoptimized atomic-centered s-type GTOs lead to a rather accurate ground state energy. As the exponents of the atomic (even-tempered) GTOs are defined by a geometric series [86], there is less chance of getting high overlap between the GTOs, and consequently, it is less likely to encounter linear dependency problems. Hence, the atomic-centered s-type GTOs are optimized more simply and quickly. Moreover, as shown in Figs. 3.8 (a) and 3.9 (a), while they remain at the center even after the full optimization, $N = 9$ atomic GTOs lead to the relative error of 8.67×10^{-13} for the ground state energy. Optimizing the same number of equidistantly distributed GTOs (with the same initial exponents), as depicted in Figs. 3.8 (b) and 3.9 (b), conceivably due to the linear dependency issues, we did not reach a relative error better than 1.49×10^{-8}. It might be reasonable to expect our optimization method to guide the initial distribution of $N = 9$ s-type GTOs similar to the atomic ones and hence to fill the vertical gap between their optimum ground state energies, the diamonds at the end of the red and the blue lines in Fig. 3.7. However, since we have chosen the initial distribution the simplest possible, i.e., equidistantly, the s-type GTOs become linear dependent as the GTOs with the opposite center-positions get too close to each other. Consequently, it is impossible to have a similar final configuration compared to the atomic ones. By choosing the initial distribution more elegantly and providing the initial configuration to be non-symmetric, one can avoid the possible numerical issues. Then by employing the same number of distributed s-type GTOs, one can obtain the same accuracy as the atomic ones. Nevertheless, the optimization of atomic s-type GTOs is considerably faster and is done in fewer iterations.To get a comparable accuracy to that of atomic GTOs, we had to use $N = 19$ distributed s-type GTOs (Figs. 3.8 (c) and 3.9 (c)) in the simulation. As it can be observed in Fig. 3.7, our optimization algorithm increases the accuracy of distributed GTOs by ten orders of magnitude for $N = 19$ and nine orders of magnitude for $N = 9$. In addition, one can note in Fig. 3.9 (a) - (c) that the exponents of some of the s-type GTOs increase in the first few iterations. However, they all follow a falling trend to the end of the optimization procedure. At the same time, the optimized s-type GTOs locate more densely. Similar to the 1D harmonic oscillator, the final configurations of s-type GTOs which represent the 1D Hydrogen atom ground state found to be symmetric.

3.2.4 1D Hydrogen molecular ion with a soft-core potential

As the last and more complex 1D system, we apply our optimization algorithm to accurately compute the ground state energy (with a relative error better than 1.0×10^{-10}) of the Hydrogen molecular ion H_2^+ at different internuclear distances. This system is modeled by considering the following 1D soft-core Hamiltonian

$$\mathrm{H} = -\frac{1}{2}\frac{\mathrm{d}^2}{\mathrm{d}x^2} - \frac{1}{\sqrt{(x-\frac{R}{2})^2+2}} - \frac{1}{\sqrt{(x+\frac{R}{2})^2+2}} + \frac{1}{R}. \tag{3.26}$$

Table 3.3 1D Hydrogen molecular ion H_2^+ with a soft-core potential: the ground state is represented by equidistantly distributed s-type GTOs at five different internuclear distances.

R (a.u.)	N	α_{ini}	X_{max}	Initial RE(E_0)	Optimum RE(E_0)	no. iter
1.0	14	3.0	5.0	3.22×10^{-2}	9.97×10^{-11}	140
2.0	15	3.0	5.0	8.87×10^{-4}	9.91×10^{-11}	16
4.0	17	3.0	6.0	1.59×10^{-3}	9.66×10^{-11}	11
8.0	22	5.0	8.0	1.65×10^{-1}	9.15×10^{-11}	34
16.0	26	3.1	16.0	1.01×10^{0}	9.98×10^{-11}	771

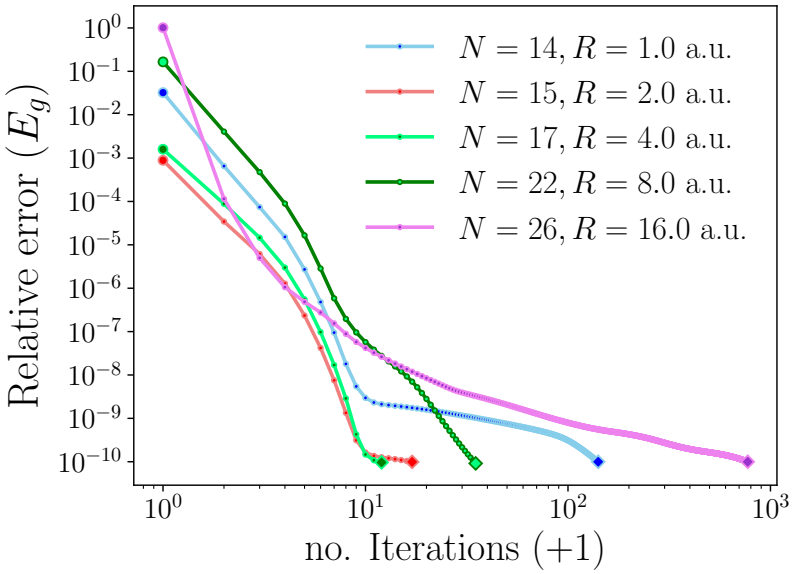

Figure 3.10 1D Hydrogen molecular ion H_2^+ : iterative enhancement of the ground state energy at different internuclear distances $R = 1.0, 2.0, 4.0, 8.0$ and 16.0 a.u.), respectively using $N = 14$, $N = 15$, $N = 17$, $N = 22$, and $N = 26$ equidistantly distributed s-type GTOs which are optimized with respect to the ground state.

In Fig. 3.10, we have plotted of the ground state energy relative error of H_2^+ at different internuclear distances $R = 1.0, 2.0, 4.0, 8.0$ and 16.0 (a.u.). Technical details are reported in Table 3.3. The reference values for the ground state energy of H_2^+ at different internuclear distances are calculated using the Numerov method [32]. As it is evident in Fig. 3.10, and Table 3.3, starting from equidistantly distributions of s-type GTOs (with the same initial exponents), our optimization procedure brings about substantial accuracy improvements for different internuclear distances. Moreover, in Fig. 3.11 (a)-(e), for five different internuclear distances: (a) $R = 1.0$ a.u., (b) $R = 2.0$ a.u., (c) $R = 4.0$ a.u., (d) $R = 8.0$ a.u., and (e)

$R = 16.0$ a.u., we have plotted the initial and optimum configurations of s-type GTOs, their corresponding probability densities, and the potential shapes. The bond between two Hydrogen atoms becomes weaker while the internuclear distance increases. In contrast to the lower internuclear distances in Fig. 3.11 (a)-(d), at the high internuclear distance $R = 16.0$ a.u. delineated in Fig. 3.11 (e) it is not necessary anymore to have s-type GTOs around the central part as the bond between the two Hydrogen atoms is pretty weak. Interestingly, the s-type GTOs representing the system's ground state at the internuclear distance $R = 16$ a.u. intelligently gather around the potential centers that are the most critical physical regions to cover. Expectedly, at high internuclear distances, the ground state energy tends to the ground state energy of the Hydrogen atom ($E_0 = -0.5$ a.u.).

In addition, for the depicted grids of s-type GTOs, the iterative optimization procedure for the center-positions x_i and exponents α_i are delineated in Fig. 3.12 (a)-(e). As we expected, all of the optimized configurations of s-type GTOs are found to be symmetric.

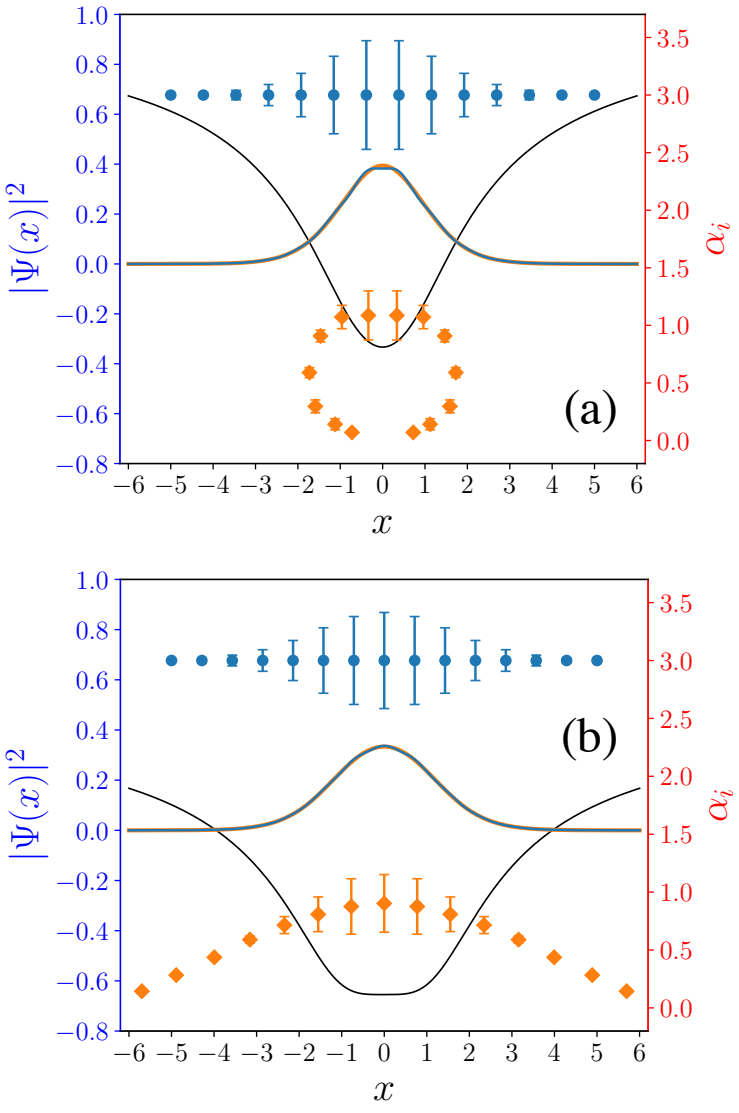

Figure details on the next page.

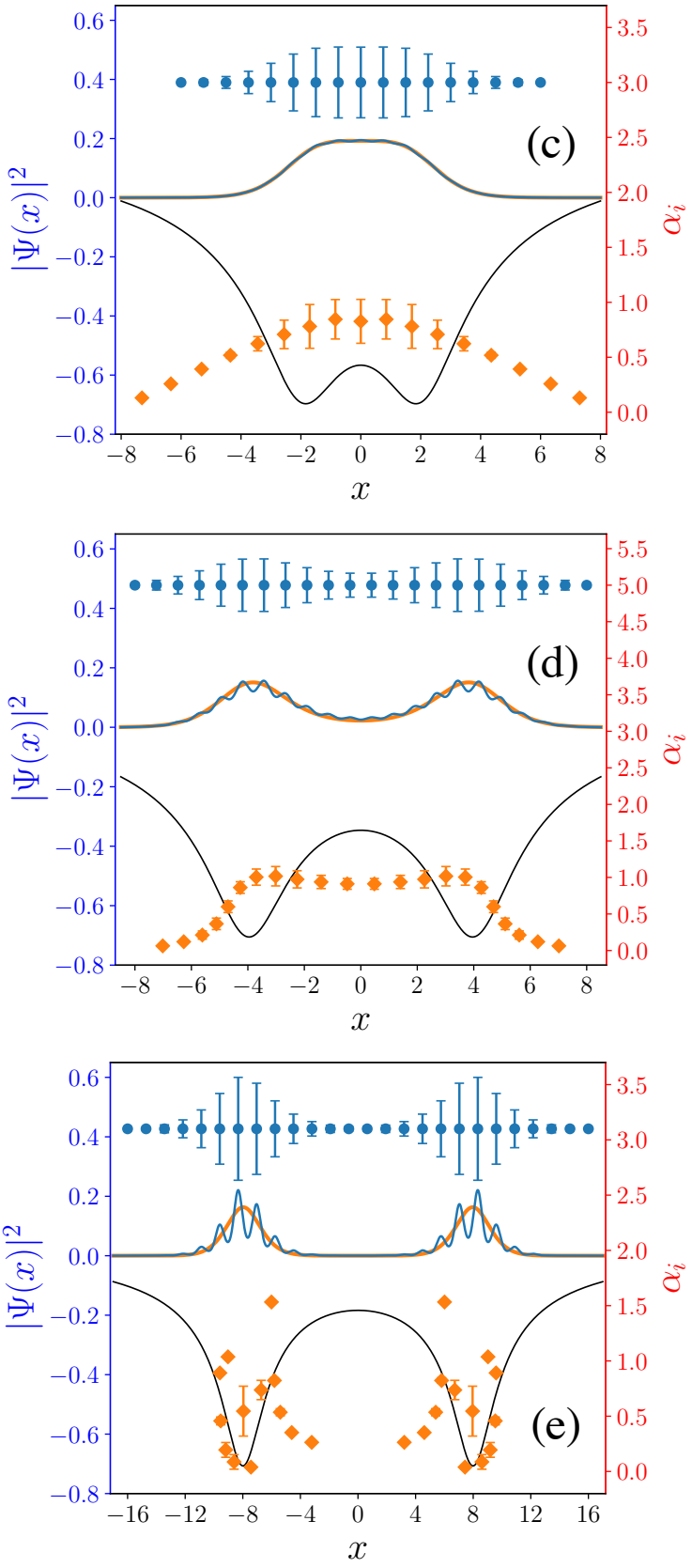

Figure 3.11 1D Hydrogen molecular ion H_2^+ : initial (the blue-colored circles) equidistantly distributed s-type GTOs are optimized (the orange-colored diamonds) to accurately represent the ground state wave function at five different internuclear distances using a 1D soft-core potential. (a) $R = 1.0$ a.u. with $N = 14$ GTOs, (b) $R = 2.0$ a.u. with $N = 15$ GTOs, (c) $R = 4.0$ a.u. with $N = 17$ GTOs, (d) $R = 8.0$ a.u. with $N = 22$ GTOs, and (e) $R = 16.0$ a.u. with $N = 26$ GTOs. The properties of these figures are similar to those of Fig. 3.2.

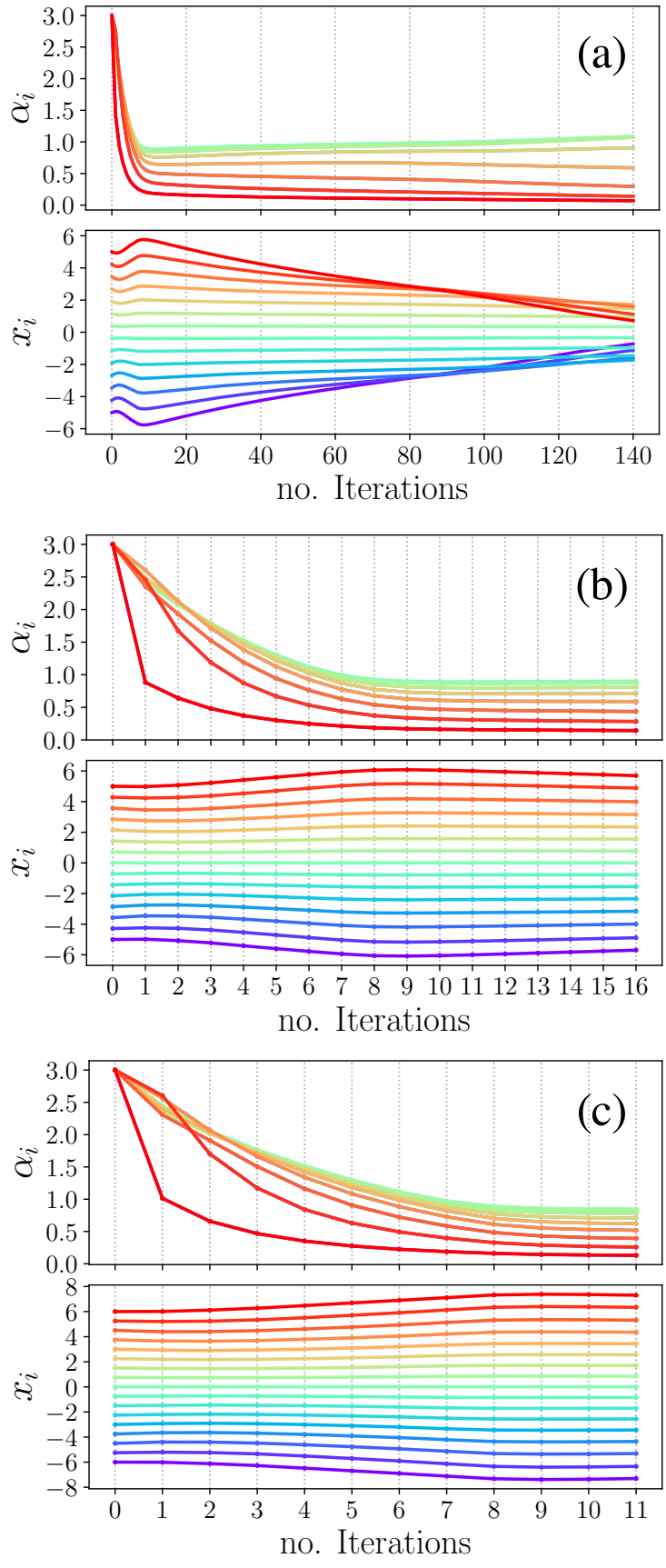

Figure details on the next page.

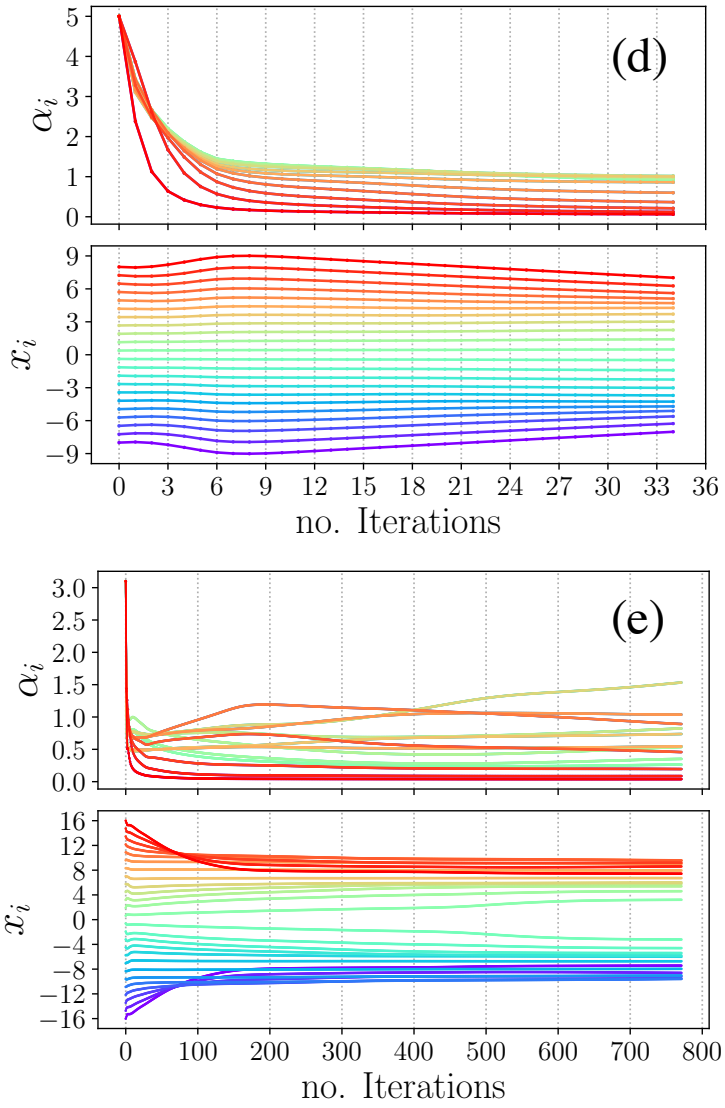

Figure 3.12 1D Hydrogen molecular ion H_2^+ : the iterative optimization procedure of the center-positions x_i, and the exponents α_i of (a) $N = 14$, (b) $N = 15$, (c) $N = 17$, (d) $N = 22$, and (e) $N = 26$ equidistantly distributed s-type GTO, receptively representing the ground state at $R = 1.0$, $R = 2.0$, $R = 4.0$, $R = 8.0$, and $R = 16.0$ a.u.

3.2.5 3D Hydrogen atom

As the first 3D system that we looked into, we applied our optimization approach for precisely representing the ground state wave function of the 3D Hydrogen atom. For this system (please see Appendix C), one needs to calculate matrix elements of the 3D Hamiltonian, $\mathrm{H} = -\frac{1}{2}\boldsymbol{\nabla}^2 - \frac{1}{|\mathbf{r}|}$, as well as those of the 3D overlap operators over 3D s-type and our auxiliary 3D d-type GTOs (for exponent optimizations), and over 3D s-type and auxiliary 3D p-type GTOs (for center-position optimizations). For the matrix elements of the Coulombic potential, as explained in in Appendix C, the first five orders of the Boys function, Eq. (B.15), should be evaluated. However, for the distributed GTOs, it was not feasible to obtain them with a high accuracy for all the center-positions, and consequently the accuracy that we can

get using distributed GTOs is limited .

For 3D Hydrogen atom, we will discuss the performance of our algorithm regarding the optimization of different configurations of s-type GTOs with respect to the ground state energy of the system: first for atomic-centered (even-tempered) GTOs, then for distributed GTOs, and last for a combination of atomic-centered and distributed GTOs.

To initially assign different exponents to N_A atomic-centered s-type GTOs positioned on the center, we use the geometric series, $\alpha_k = \alpha_0 \gamma^k$, where $-\frac{N_A-1}{2} \leq k \leq \frac{N_A-1}{2}$ is used for configurations that have only atomic-centered GTOs, and $k = 1, \cdots, N_A$ is considered when we employ a combination of atomic-centered and distributed GTOs.

Table 3.4 3D Hydrogen atom: optimizing atomic-centered (even-tempered) s-type GTOs to accurately represent the ground state wave function.

N	γ	Initial RE(E_0)	Optimum RE(E_0)	no. iter
3	5.0	2.00×10^{-2}	6.04×10^{-3}	45
5	5.0	4.70×10^{-3}	3.80×10^{-4}	59
7	5.0	2.84×10^{-3}	3.34×10^{-5}	72
9	5.0	2.68×10^{-3}	3.72×10^{-6}	81
11	5.0	2.66×10^{-3}	4.98×10^{-7}	90
13	4.0	6.88×10^{-4}	7.66×10^{-8}	93
15	4.0	6.87×10^{-4}	1.32×10^{-8}	92
17	3.5	2.30×10^{-4}	2.50×10^{-9}	91
19	3.0	4.24×10^{-5}	5.15×10^{-10}	100
21	3.0	4.23×10^{-5}	1.13×10^{-10}	84
23	2.8	1.57×10^{-5}	9.08×10^{-11}	35

In the first part, for the atomic-centered s-type GTOs, we used $\alpha_0 = \frac{8}{9\pi}$ which is analytically obtainable optimizing a single s-type GTO representing the system (please refer to Sec. C.2.8 for more details).

Employing only atomic-centered GTOs, as what we have already witnessed for the 1D case (in Table 3.2 and Fig. 3.7), expectedly we obtain highly accurate results for the ground state energy quickly in less than 100 optimization iterations. As another proof for the fact that atomic-centered GTOs are the best for representing the ground state of the Hydrogen atom, all of the optimized atomic-centered GTOs remain at the center while their exponents change.

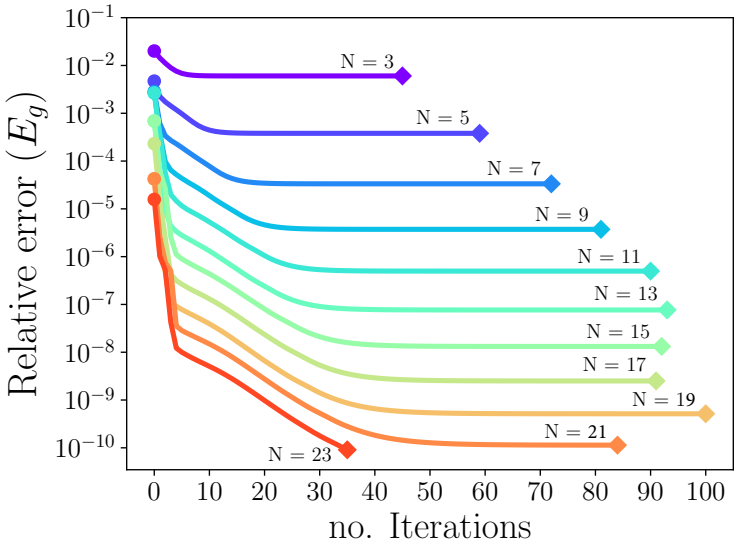

Figure 3.13 3D Hydrogen atom: iterative enhancement of the ground state energy using up to $N = 23$ atomic-centered (even-tempered) s-type GTOs being optimized with respect to the ground state. Circles and diamonds respectively denote the initial and the optimum configurations.

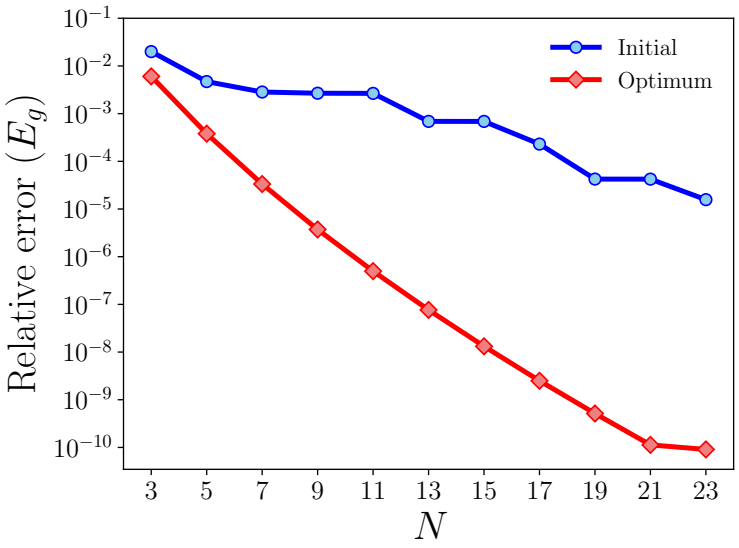

Figure 3.14 3D Hydrogen atom: ground state energy relative errors associated with the initial (even-tempered: the blue-colored circles) and optimum (the red-colored diamonds) configurations of atomic-centered s-type GTOs vs. the number of GTOs.

From Table 3.4, and Figs. 3.13 and 3.14, one can deduce that more than $N = 20$ atomic-centered GTOs should be optimized to reach the desired accuracy of 1.0×10^{-10}, while as reported in [87], employing the same α_0 and with $\gamma = 2.0$, $N = 51$ unoptimized atomic-centered GTOs are required to get a comparable accuracy. It is also comprehensible that the initial ground state energy associated with the unoptimized configurations of atomic-centered s-type GTOs are considerably improved after the optimization procedure.

In the next step, we have examined how our approach performs in optimizing N_D distributed s-type GTOs and their combination with N_A atomic-centered s-type GTOs.

Details are listed in Table 3.5. As can be seen in Table 3.5 and the red-colored line in Fig. 3.15, optimizing only $N_D = 27$ distributed GTOs, we quickly reach the accuracy 7.99×10^{-5} for the ground state energy of 3D Hydrogen atom, while as reported in [87], to reach a comparable accuracy, a combination of $N_D = 125$ distributed and $N_A = 30$ atomic-centered s-type GTOs is necessary.

Table 3.5 3D Hydrogen atom: optimizing a combination of N_A atomic-centered (even-tempered with $\alpha_0 = \alpha_{ini}$) and N_D equidistantly distributed s-type GTOs (between $-X_{max}$ and X_{max}) to accurately represent the ground state wave function.

Approach	N_A	N_D	N	γ	α_{ini}	X_{max}	RE(E_0^{ini})	RE(E_0^{opt})	no. iter	time(s)
LCDAO *	30	$5 \times 5 \times 5$	155	2	$8/9\pi$	3.1457	9.48×10^{-5}	-	-	-
LCDAO *	30	$13 \times 13 \times 13$	2227	2	$8/9\pi$	9.4373	2.20×10^{-7}	-	-	-
Optimized	0	$3 \times 3 \times 3$	27	-	0.2	3.0	1.61×10^{-1}	7.99×10^{-5}	980	10.72
Optimized	12	$3 \times 3 \times 3$	39	3.0	0.2	3.0	2.18×10^{-4}	4.99×10^{-8}	332	6.83

* LCDAO: Linear combination of distributed and atomic orbitals reported in [87].

In the same work [87], increasing the number of distributed s-type GTOs to $N_D = 2197$, an accuracy of 2.20×10^{-7} was achieved. In contrast, we do not need to include such high numbers of s-type GTOs into the simulation in order to get higher precisions. Adding only $N_A = 12$ atomic-centered s-type GTOs to our minimal distributed basis set ($N_D = 27$), as the blue-colored line in Figure 3.15 shows, our optimization approach leads much faster to the accuracy of 4.99×10^{-8}. As we already discussed, atomic-centered GTOs are necessary for obtaining high accuracies. It is not feasible to reach higher accuracies employing distributed s-type GTOs in that continuous evaluation of the higher orders of Boys functions is not accurately doable for all GTOs positions.

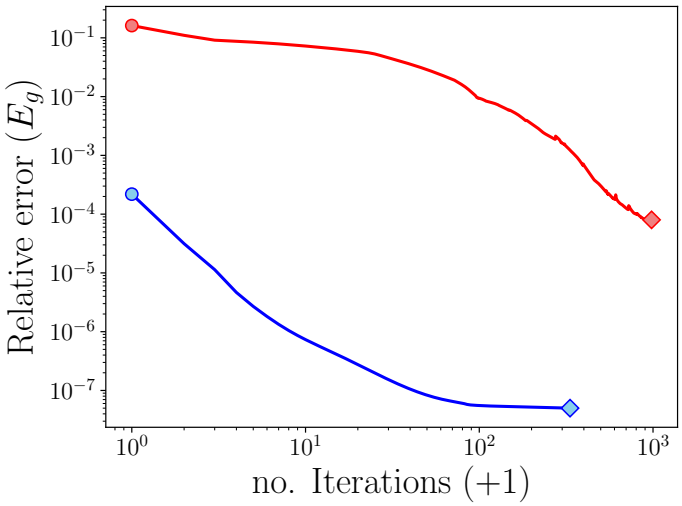

Figure 3.15 3D Hydrogen atom: iterative improvement of the ground state energy employing $N_D = 3 \times 3 \times 3$ distributed s-type GTOs (red-colored) and a combination of $N_D = 3 \times 3 \times 3$ distributed s-type GTOs and $N_A = 12$ atomic-centered s-type GTOs (blue-colored) which are optimized with respect to the ground state. Circles and diamonds, respectively, indicate the initial and the optimum configurations.

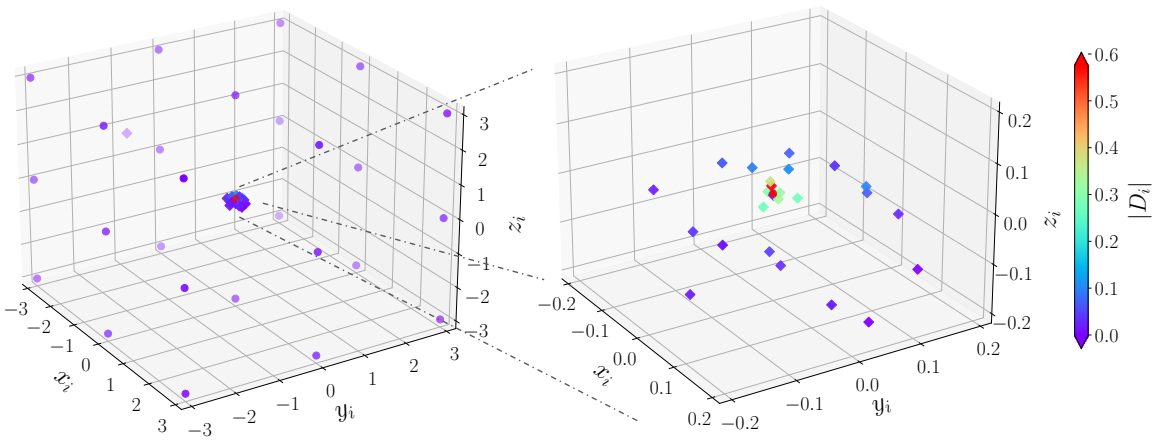

Figure 3.16 3D Hydrogen atom: the ground state wave function is represented by superposing $N_D = 3 \times 3 \times 3$ distributed GTOs. Circles show the initial configuration and the diamonds portray the optimum configuration. The color map indicates the normalized coefficients $|D_i|$ associated with the initial and the optimum configurations. The right hand side figure is the enlargement of the central part.

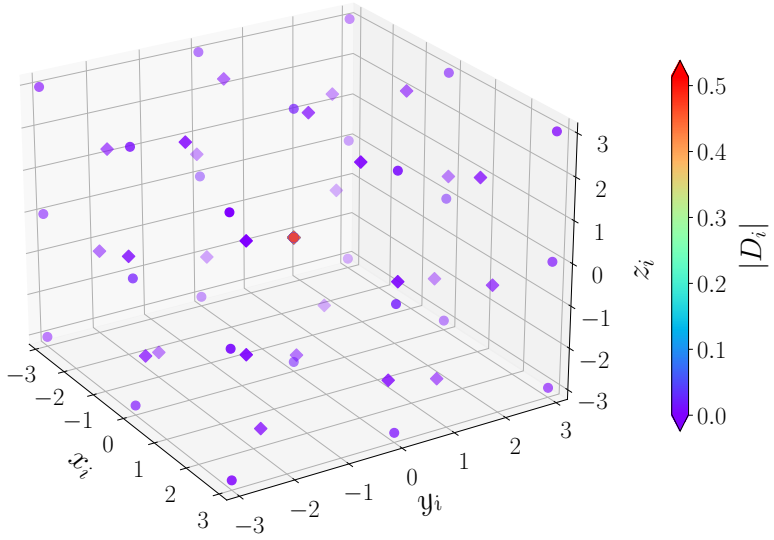

Figure 3.17 3D Hydrogen atom: the ground state wave function is represented by superposing $N_D = 3 \times 3 \times 3$ distributed s-type GTOs and $N_A = 12$ atomic-centered ones. This figure shares the same properties as Fig. 3.16 .

In addition, in Figs. 3.16, and 3.17 , respectively, we have depicted the initial and optimum configurations associated with only $N_D = 27$ distributed s-type GTOs and their combination with $N_A = 12$ atomic-centered s-type GTOs. The color map indicates the normalized coefficients $|D_i|$ which show to what extent each GTO contributes into the wave function. It can be seen from Fig. 3.16 that the optimally distributed s-type GTOs (diamonds) gather ultimately around the origin where they are needed most. On the contrary, as can be seen in Fig. 3.17, having $N_A = 12$ atomic-centered s-type GTOs, there is no more need for distributed GTOs to gather around the center. In both Figures, it can also be verified that the

ones located on or around the center have the highest contributions in representing the wave function.

For the combination case, we used the correction parameters $h_\alpha = h_{\mathbf{r}} = 0.5$.

3.2.6 3D Hydrogen molecular ion

As the last system that we discuss in this chapter, to represent the ground state wave function of the 3D Hydrogen molecular ion H_2^+ , $H = -\frac{1}{2}\boldsymbol{\nabla}^2 - \frac{1}{|\mathbf{r}-\mathbf{R}_1|} - \frac{1}{|\mathbf{r}-\mathbf{R}_2|} + \frac{1}{R}$, at the internuclear distance $R = |\mathbf{R}_2 - \mathbf{R}_1| = 2.0$ a.u., we have applied our approach for optimizing a minimal basis set of $N = 3 \times 3 \times 3 = 27$ distributed s-type GTOs.

Table 3.6 3D Hydrogen molecular ion at $R = 2.0$ a.u.: comparison of the relative error of the ground state energy obtained in this work optimizing a total of 27 distributed s-type GTOs and another approach which employs a high number of unoptimized s-type GTOs in combination with a set of higher-order atomic ones.

Approach	N^{type} Atomic	N^{type} Distributed	N	RE(E_0)*
LCDAO**	$2 \times (30^s)$	$9^s \times 9^s \times 21^s$	1761	3.68×10^{-3}
LCDAO**	$2 \times (30^s + 10^p)$	$9^s \times 9^s \times 21^s$	1821	2.53×10^{-4}
LCDAO**	$2 \times (30^s + 10^p + 5^d)$	$9^s \times 9^s \times 21^s$	1881	5.898×10^{-6}
v6z: MOLPRO***	$6^s + 5^p + 4^d + 3^f + 2^g + 1^h$	0	182	3.52×10^{-6}
Optimized	0	$3^s \times 3^s \times 3^s$	27	3.49×10^{-6}

* Relative errors are computed using the most recent and accurate reported value [88].

** LCDAO: Linear combination of distributed and atomic orbitals reported in [87].

*** v6z: MOLPRO: used as the reference in [87].

In Table 3.6, we have compared our results with two other approaches that use GTOs as basis functions. Note the considerable differences in the number and types of the GTOs used in the different approaches. Optimizing only $N_D = 27$ distributed s-type GTOs, we reach an accuracy better than those of the other mentioned approaches. In Fig. 3.18, we have depicted how the relative error of the ground state energy decreases starting from 2.25×10^{-1}. The best accuracy from the LCDAO approach reported in [87], is obtained employing $N_D = 1701$ equidistantly distributed s-type GTOs in combination with not only s-type atomic centered GTOs, but also p-type, and d-type ones. In the same work, the used reference value was obtained from the MOLPRO program package employing up to h-type GTOs.

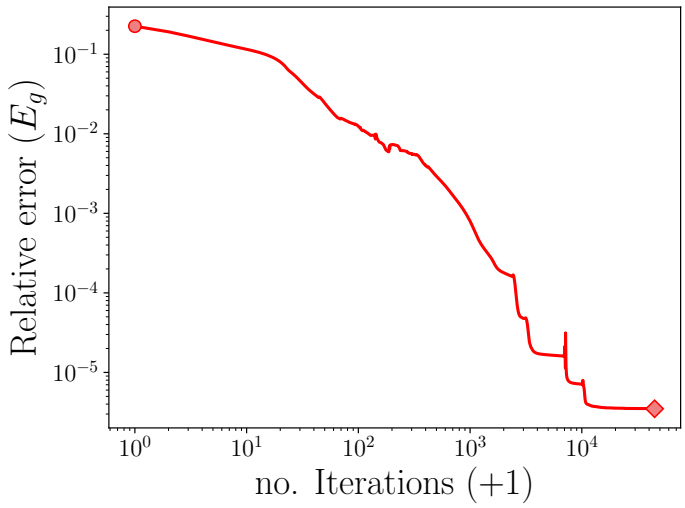

Figure 3.18 3D Hydrogen molecular ion: iterative optimization of the ground state energy employing $N_D = 3 \times 3 \times 3$ distributed s-type GTOs being optimized with respect to the ground state. Circles and diamonds respectively denote the initial and the optimum configurations.

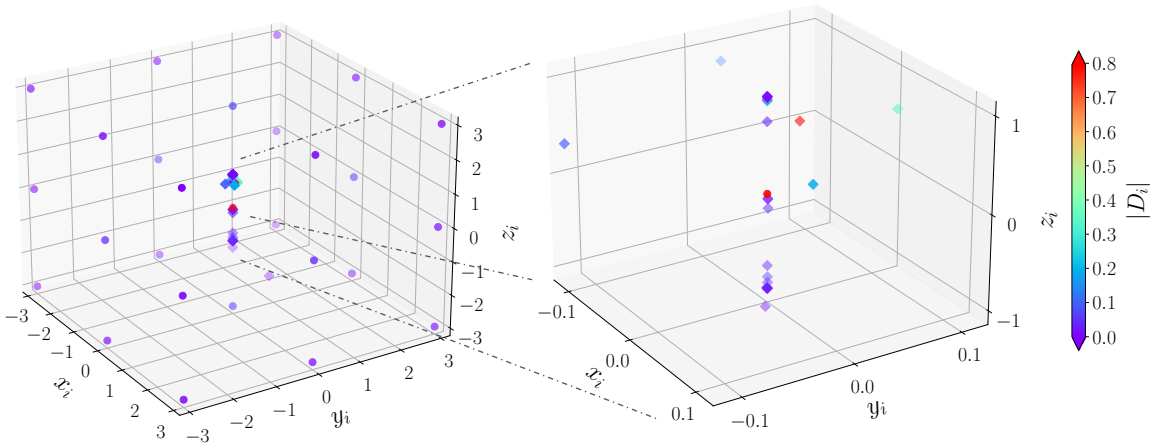

Figure 3.19 3D Hydrogen molecular ion: ground state wave function is represented by superposing $N_D = 3 \times 3 \times 3$ distributed GTOs. This figure shares the same properties as Fig. 3.16.

In Fig. 3.19, we have plotted the initial and optimum configurations of $N_D = 3 \times 3$ distributed s-type GTOs. As can be seen in the magnified figure on the right, the used s-type GTOs end up in the most critical physical regions, i.e., around the origin and the positions of the two nuclei. Similar to 1D case depicted in Fig. 3.11 (b), at the investigated internuclear distance $R = 2.0$ a.u., the two atoms are strongly bonded. Hence, we need to have s-type GTOs around the two nuclei and on the central part. As before, the color map denotes the normalized coefficients $|D_i|$, showing the contribution of each GTO in the wave function. For this part, we set the correction parameters $h_\alpha = h_\mathbf{r} = 0.1$.

4 Moving Gaussian basis sets for time-dependent problems

In this chapter, we will use our optimization procedure for the time evolution of the wave function employing 1D s-type GTOs. First, in Sec. 4.1, we explain in detail how the wave function time evolution is done on the basis of 1D s-type GTOs. In addition, in Sec. 4.1.1 we point out how the s-type GTOs are optimized at each time step. In Sec. 4.1.2, we describe how we compute the auto-correlation function. Next, in Sec. 4.2, as an initial performance assessment of our time-dependent optimization algorithm, we apply the time evolution optimization process on two eigenstates (the ground state and the second excited state) of the 1D harmonic oscillator. Moreover, shifting the initial wave functions to the left along the x axis, we assess the optimized s-type GTOs representing two new wave functions that are not eigenstates of the system anymore.

Ultimately, in Sec. 4.3, we implement our time-dependent optimization approach for studying the HHG spectra in two 1D laser-induced systems: the 1D Hydrogen atom (Sec. 4.3.1), and the 1D ionized Hydrogen molecule (Sec. 4.3.2).

Here, all of the reference results are obtained using the split-step Fourier method (SSFM) [89]. In addition, the time step $dt = 0.1$ (a.u.) is used everywhere for the time evolution process unless mentioned otherwise.

4.1 Theory: time evolution of the wave-function

The initial wave function $|\psi(t)\rangle$, which is accurately represented by an optimized grid of the s-type GTOs, is propagated in real-time using the time-evolution operator, $e^{-\mathrm{i}\mathrm{H}\Delta t}$, to get the time evolved wave function

$$|\psi(t+\Delta t)\rangle = e^{-\mathrm{i}\mathrm{H}\Delta t}\,|\psi(t)\rangle = e^{-\mathrm{i}\mathrm{H}\Delta t}\sum_{i=1}^{N} D_i^{s_t}\,|\mathcal{G}_i^{s_t}\rangle\,, \tag{4.1}$$

where

$$D_i^{s_t} = \sum_{j=1}^{N} {\Omega_{ij}^{s_t s_t}}^{-1} C_j^{s_t} \quad , \quad C_j^{s_t} = \langle \mathcal{G}_j^{s_t} | \psi(t) \rangle\,. \tag{4.2}$$

Strang splitting the time evolution operator [90]

$$e^{-\mathrm{iH}\Delta t} \approx e^{-\frac{1}{2}\mathrm{iV}\Delta t} e^{-\mathrm{iT}\Delta t} e^{-\frac{1}{2}\mathrm{iV}\Delta t} + \mathcal{O}\left(\Delta t^3\right), \tag{4.3}$$

inserting the position space identity $\int_{-\infty}^{\infty} \mathrm{d}x \, |x\rangle \langle x|$ twice, and the momentum space unity $\int_{-\infty}^{\infty} \mathrm{d}p \, |p\rangle \langle p|$ once, and using $\langle x|p\rangle = \frac{1}{\sqrt{2\pi}} e^{\mathrm{i}px}$, from Eq. (4.1), it is straightforward to get

$$\begin{aligned} |\psi(t+\Delta t)\rangle \approx \sum_{i=1}^{N} D_i^{st} \int_{-\infty}^{\infty} \mathrm{d}x'' \, |x''\rangle \, e^{-\frac{\mathrm{iV}(x'')\Delta t}{2}} \frac{1}{\sqrt{2\pi}} \int_{-\infty}^{\infty} \mathrm{d}p' e^{-\frac{\mathrm{i}p'^2 \Delta t}{2}} e^{\mathrm{i}p'x''} \times \\ \frac{1}{\sqrt{2\pi}} \int_{-\infty}^{\infty} \mathrm{d}x' e^{-\frac{\mathrm{iV}(x')\Delta t}{2}} e^{-\mathrm{i}p'x'} \mathcal{G}_i^{st}(x'). \end{aligned} \tag{4.4}$$

Taylor expanding $\mathrm{V}(x')$ up to the second order around the real part of the s-type GTOs center-positions and reordering its terms, one can verify that

$$e^{-\frac{\mathrm{iV}(x')\Delta t}{2}} = e^{-c_i} e^{-a_i (x' - b_i)^2}, \tag{4.5}$$

where

$$a_i = \frac{\mathrm{i}\Delta t}{4} \frac{\mathrm{d}^2 \mathrm{V}(x')}{\mathrm{d}x'^2}\Big|_{x'=\mathcal{R}(x_i)}, \tag{4.6a}$$

$$b_i = \mathcal{R}(x_i) - \frac{\frac{\mathrm{dV}(x')}{\mathrm{d}x'}\Big|_{x'=\mathcal{R}(x_i)}}{\frac{\mathrm{d}^2 \mathrm{V}(x')}{\mathrm{d}x'^2}\Big|_{x'=\mathcal{R}(x_i)}}, \tag{4.6b}$$

$$c_i = \frac{\mathrm{i}\Delta t}{2} \left(\mathrm{V}(\mathcal{R}(x_i)) - \frac{\left(\frac{\mathrm{dV}(x')}{\mathrm{d}x'}\Big|_{x'=\mathcal{R}(x_i)} \right)^2}{2 \frac{\mathrm{d}^2 \mathrm{V}(x')}{\mathrm{d}x'^2}\Big|_{x'=\mathcal{R}(x_i)}} \right). \tag{4.6c}$$

Substituting $\mathcal{G}_i^{st}(x') = e^{-\alpha_i^{st}\left(x' - x_i^{st}\right)^2}$ in Eq. (4.4), and utilizing the Gaussian product rule, Eq. (3.2), and the Gaussian integral, Eq. (C.9), it is straightforward to get

$$|\psi(t+\Delta t)\rangle \approx \sum_{i=1}^{N} D_i^{st} \left(\frac{a'}{\gamma} \right)^{1/2} \mathcal{A} \int_{-\infty}^{\infty} \mathrm{d}x'' \, |x''\rangle \, e^{-\frac{\mathrm{iV}(x'')\Delta t}{2}} e^{-a'(x'' - b')^2}, \tag{4.7}$$

where

$$\gamma = a_i + \alpha_i^{st}, \tag{4.8a}$$

$$\beta = \frac{a_i \alpha_i^{st}}{\gamma}, \tag{4.8b}$$

$$b' = \frac{a_i b_i + \alpha_i^{st} x_i^{st}}{\gamma}, \tag{4.8c}$$

$$a' = \frac{\gamma}{1 + 2\mathrm{i}\gamma\Delta t}, \tag{4.8d}$$

$$\mathcal{A} = e^{-c_i} e^{-\beta(b_i - x_i))^2}. \tag{4.8e}$$

To simplify the mathematical identities in Eq. (4.8), and the upcoming Eqs. (4.10), and (4.14), we have eliminated the sub-indices for the left hand side variables. The wave function at the new time step, $|\psi(t+\Delta t)\rangle$, can be represented as a superposition of the same s-type GTOs representing the wave function at the previous time step $|\psi(t)\rangle$. In this manner, their contribution to the wave function, i.e. the coefficients $D_i^{s_t}$ get updated through the time evolution while the exponents, $\alpha_i^{s_t}$, and center-positions, $x_i^{s_t}$, remain unchanged. However, we know that a low number of s-type GTOs optimized with respect to a time-independent electronic state would not suffice to get accurate results in the time-dependent process, especially in the presence of external potentials. Hence, in an iterative procedure, we consecutively optimize the exponents and the center-positions of s-type GTOs at each time step. For the sake of simplicity, we fix the number of iterations. Instead, one could keep performing the optimization process until a certain criterion is met. One criterion can be the convergence for the expectation value of an observable. As explained in Sec. 4.1.1, for optimizing the center-positions and the exponents of s-type GTOs, we respectively employ auxiliary p-type and d-type GTOs.

In a general manner, multiplying Eq. (4.7) from the left to $\langle \mathcal{G}_l^{m_t}|$, using the unnormalized 1D GTOs from Eq. (3.7), and applying the Gaussian product rule, one can obtain

$$C_l^{m_{t+\Delta t}} \approx \sum_{i=1}^{N} D_i^{s_t} \left(\frac{a'}{\gamma}\right)^{1/2} \mathcal{A} e^{-\beta'\left(x_l^{s_t *}-b'\right)^2} \int_{-\infty}^{\infty} \mathrm{d}x''(x''-x_l^{s_t *})^m e^{-\frac{\mathrm{i}\mathrm{V}(x'')\Delta t}{2}} e^{-\gamma'(x''-b'')^2}, \tag{4.9}$$

where $C_l^{m_{t+\Delta t}} = \langle \mathcal{G}_l^{m_t}|\psi(t+\Delta t)\rangle$, and

$$\gamma' = \alpha_l^{s_t *} + a', \tag{4.10a}$$

$$\beta' = \frac{\alpha_l^{s_t *} a'}{\gamma'}, \tag{4.10b}$$

$$b'' = \frac{\alpha_l^{s_t *} x_l^{s_t *} + a' b'}{\gamma'}. \tag{4.10c}$$

Taylor expanding $\mathrm{V}(x'')$ up to the second order around the real part of the remaining Gaussian center in Eq. (4.9), b'', and reordering its terms, one can show that

$$e^{-\frac{\mathrm{i}\mathrm{V}(x'')\Delta t}{2}} = e^{-c_{b''}} e^{-a_{b''}(x''-b_{b''})^2}, \tag{4.11}$$

where

$$a_{b''} = \frac{\mathrm{i}\Delta t}{4} \frac{\mathrm{d}^2\mathrm{V}(x'')}{\mathrm{d}x''^2}\Big|_{x''=\mathcal{R}(b'')}, \tag{4.12a}$$

$$b_{b''} = \mathcal{R}(b'') - \frac{\frac{\mathrm{d}\mathrm{V}(x'')}{\mathrm{d}x''}\Big|_{x''=\mathcal{R}(b'')}}{\frac{\mathrm{d}^2\mathrm{V}(x'')}{\mathrm{d}x''^2}\Big|_{x''=\mathcal{R}(b'')}}, \tag{4.12b}$$

$$c_{b''} = \frac{\mathrm{i}\Delta t}{2}\left(\mathrm{V}(\mathcal{R}(b'')) - \frac{\left(\frac{\mathrm{dV}(x'')}{\mathrm{d}x''}|_{x''=\mathcal{R}(b'')}\right)^2}{2\frac{\mathrm{d}^2\mathrm{V}(x'')}{\mathrm{d}x''^2}|_{x''=\mathcal{R}(b'')}}\right). \tag{4.12c}$$

Applying the Gaussian product rule leads to

$$C_l^{m_{t+\Delta t}} \approx \sum_{i=1}^{N} D_i^{s_t}\left(\frac{a'}{\gamma}\right)^{1/2}\mathcal{A}\mathcal{B}\int_{-\infty}^{\infty}\mathrm{d}x''(x''-x_l^{s_t*})^m e^{-\gamma''(x''-b''')^2}, \tag{4.13}$$

where

$$\gamma'' = a_{b''} + \gamma', \tag{4.14a}$$

$$\beta'' = \frac{a_{b''}\gamma'}{\gamma''}, \tag{4.14b}$$

$$b''' = \frac{a_{b''}b_{b''} + \gamma' b''}{\gamma''}, \tag{4.14c}$$

$$\mathcal{B} = e^{-\beta'\left(x_l^{s_t*}-b'\right)^2} e^{-c_{b''}} e^{-\beta''(b_{b''}-b''))^2}. \tag{4.14d}$$

Ultimately, employing Eq. (C.9), it is straightforward to obtain the following analytical expressions, respectively for s-type, p-type and d-type GTOs

$$C_l^{s_{t+\Delta t}} \approx \sum_{i=1}^{N} D_i^{s_t}\left(\frac{\pi a'}{\gamma\gamma''}\right)^{1/2}\mathcal{A}\mathcal{B}, \tag{4.15a}$$

$$C_l^{p_{t+\Delta t}} \approx \sum_{i=1}^{N} D_i^{s_t}(b''' - x_l^{s_t*})\left(\frac{\pi a'}{\gamma\gamma''}\right)^{1/2}\mathcal{A}\mathcal{B}, \tag{4.15b}$$

$$C_l^{d_{t+\Delta t}} \approx \sum_{i=1}^{N} D_i^{s_t}\left(1 + 2\gamma''(b''' - x_l^{s_t*})^2\right)\left(\frac{\pi a'}{4\gamma\gamma''^3}\right)^{1/2}\mathcal{A}\mathcal{B}. \tag{4.15c}$$

4.1.1 Time-dependent optimization of s-type GTOs

To optimize the center-positions of s-type GTOs, similar to the optimization process mentioned in Sec. 3.1.3, we represent the wave function at each new time step $|\psi(t+\Delta t)\rangle$ employing N s-type GTOs, $|\mathcal{G}_k^{s_t}\rangle$, and N auxiliary p-type GTOs, $|\mathcal{G}_k^{p_t}\rangle$

$$|\psi(t+\Delta t)\rangle = \sum_{k=1}^{N} D_k^{s_t p_t\top}|\mathcal{G}_k^{s_t p_t}\rangle = \sum_{k=1}^{N} D_k^{s_t}|\mathcal{G}_k^{s_t}\rangle + \sum_{k=1}^{N} D_k^{p_t}|\mathcal{G}_i^{p_t}\rangle, \tag{4.16}$$

where $|\mathcal{G}_k^{s_t p_t}\rangle = |\mathcal{G}_k^{s_t}\rangle \oplus |\mathcal{G}_k^{p_t}\rangle = \begin{pmatrix}|\mathcal{G}_k^{s_t}\rangle \\ |\mathcal{G}_k^{p_t}\rangle\end{pmatrix}$, and $D_k^{s_t p_t} = D_k^{s_t} \oplus D_k^{p_t} = \begin{pmatrix}D_k^{s_t} \\ D_k^{p_t}\end{pmatrix}$. Multiplying the l^{th} s-type and p-type GTOs as a single vector, $\langle\mathcal{G}_l^{s_t p_t}|$, from the left to $|\psi(t+\Delta t)\rangle$, we

get the coefficients $C_l^{s_t p_t}$

$$C_l^{s_t p_t} = \langle \mathcal{G}_l^{s_t p_t} | \psi(t+\Delta t) \rangle = \langle \mathcal{G}_l^{s_t} | \psi(t+\Delta t) \rangle \oplus \langle \mathcal{G}_l^{p_t} | \psi(t+\Delta t) \rangle = C_l^{s_t} \oplus C_l^{p_t}. \quad (4.17)$$

The coefficients $C_l^{s_t}$, and $C_l^{p_t}$ are computable employing Eqs. (4.15a), and (4.15b), respectively. In the time-independent optimization procedure, we had to solve the GEVP to obtain the coefficients $D_i^{s_t}$, and $D_i^{p_t}$. On the contrary, here we calculate them using Eq. (4.2)

$$D_k^{s_t p_t} = \sum_{l=1}^{N} {\Omega_{kl}^{s_t p_t}}^{-1} C_l^{s_t p_t} = D_i^{s_t} \oplus D_i^{p_t}, \quad (4.18)$$

where, ${\Omega^{s_t p_t}}^{-1}$, the inverse of the overlap matrix over s-type, and p-type GTOs is schematically explained in Sec. 3.1.3. There is no need for evaluating the Hamiltonian matrix elements over s-type, and p-type GTOs in the time-dependent part. One can compute the center-positions corrections using Eq. (3.20) after obtaining the $D_k^{s_t}$, and $D_k^{p_t}$.

Following the same approach explained for optimizing the center-positions (Eqs. 4.16, 4.17, and 4.18), and employing N auxiliary d-type GTOs $\left|\mathcal{G}^{d_t}\right\rangle$ instead of N p-type GTOs $|\mathcal{G}^{p_t}\rangle$, one can optimize the exponents of s-type GTOs during the time evolution process as well.

4.1.2 Auto-correlation function

To calculate the auto-correlation function, $\mathbb{A}(t) = \langle \psi(t) | \psi(0) \rangle$, using the identity operator of the s-type GTOs, $\mathbb{I} = \sum_{i,j=1}^{N} |\mathcal{G}_i^s\rangle \, {\Omega_{ij}^{ss}}^{-1} \left\langle \mathcal{G}_j^s \right|$, twice, one can verify that

$$\mathbb{A}(t) = \langle \psi(t) | \psi(0) \rangle = \sum_{j,k=1}^{N} \Omega_{jk}^{s_t s_0} D_j^{s_t^*} D_k^{s_0}, \quad (4.19)$$

where, with the help of Eq. (4.2), we have

$$D_j^{s_t^*} = \sum_{i=1}^{N} C_i^{s_t^*} {\Omega_{ij}^{s_t s_t}}^{-1} \quad , \quad C_i^{s_t^*} = \langle \psi(t) | \mathcal{G}_i^{s_t} \rangle \, , \quad (4.20a)$$

$$D_k^{s_0} = \sum_{l=1}^{N} C_l^{s_0} {\Omega_{kl}^{s_0 s_0}}^{-1} \quad , \quad C_l^{s_0} = \langle \mathcal{G}_l^{s_0} | \psi(t=0) \rangle \, . \quad (4.20b)$$

Employing Eq. (C.2), it is easy to calculate the overlap between the j^{th} time-evolved and the i^{th} initial s-type GTOs

$$\Omega_{jk}^{s_t s_0} = \left\langle \mathcal{G}_j^{s_t} \middle| \mathcal{G}_k^{s_0} \right\rangle = \left(\frac{\pi}{\gamma_{jk}^{s_t s_0}} \right)^{1/2} e^{-\beta_{jk}^{s_t s_0} \left({x_j^{s_t}}^* - x_k^{s_0} \right)}, \quad (4.21a)$$

$$\gamma_{jk}^{s_t s_0} = \alpha_j^{s_t *} + \alpha_k^{s_0} \quad , \quad \beta_{jk}^{s_t s_0} = \frac{\alpha_j^{s_t *} + \alpha_k^{s_0}}{\gamma_{jk}^{s_t s_0}}. \tag{4.21b}$$

Performing no optimization during the time-dependent process, the exponents and center-positions of the s-type GTOs are not changed. In this case, as mentioned before, just the coefficients are updated and it simply yields $\Omega_{jk}^{s_t s_0} = \Omega_{jk}^{s_0 s_0}$.

4.2 Time evolution of 1D harmonic oscillator

To assess the time-dependent optimization approach explained in Sec. 4.1, we evolve the ground state and the 2^{nd} excited state wave functions of the 1D harmonic oscillator over a total time duration of 25 (a.u.). This time interval covers two and ten natural cycles of the ground state and the 2^{nd} excited state, respectively. We begin with the optimum configurations of s-type GTOs obtained from the time-independent optimization procedure described in Sec. 3.1. Experiencing no external potential, no matter if the initial s-type GTOs representing these two eigenstates are optimized during the time evolution or not, the probability density of their wave functions should remain unchanged during the time evolution process and a good accuracy should be achieved for the auto-correlation function. Shifting the initial wave functions along the x axis to the left by -0.5 (a.u.), we make two new wave functions for which the initial configurations of s-type GTOs are not going to be sufficient for getting a good accuracy for the auto-correlation function as they are no longer eigenstates of the system. Hence, the s-type GTOs must be optimized to give the desirable accuracy for the auto-correlation function.

Table 4.1 The ground state time evolution of the 1D harmonic oscillator using an optimum s-type GTO. The second column gives the relative error maximum value of $|\mathbb{A}(t)|$ during the whole time evolution $T = 25$ (a.u.).

(a) As an eigenstate of the system

	dt	max RE($\lvert\mathbb{A}(t)\rvert$)	no. iter
No Opt	0.1	9.77×10^{-6}	-
Full Opt	0.1	7.10×10^{-13}	10

(b) The position shifted wave function

	dt	max RE($\lvert\mathbb{A}(t)\rvert$)	no. iter
No Opt	0.1	2.24	-
Full Opt	0.1	4.76×10^{-5}	10
Full Opt	0.01	4.81×10^{-6}	10
Full Opt	0.1	8.88×10^{-13}	50

We begin our assessment by representing the ground state of the system using a single s-type GTO with the optimum parameters $x = 0$, and $\alpha = 0.5$. As mentioned in Sec. 3.2.1, this optimized s-type GTO suffices to get the exact ground state energy. In Table 4.1 (a), and Fig. 4.1, we have compared the probability density of the ground state and the accuracy of the auto-correlation function from an unoptimized s-type GTO and the one optimized in 10 iterations at each time step. Taylor expanding the potential up to the second-order, Eq. (4.5),

is sufficient for getting the exact harmonic oscillator potential, Eq. (3.22). Consequently, for an eigenstate of the system, one might expect to get a high accuracy for the probability density and the auto-correlation function. However, the intrinsic error of $\mathcal{O}[\Delta t^3]$ in the Strang splitting of the time evolution operator (Eq. (4.3)) restricts the achievable accuracy.

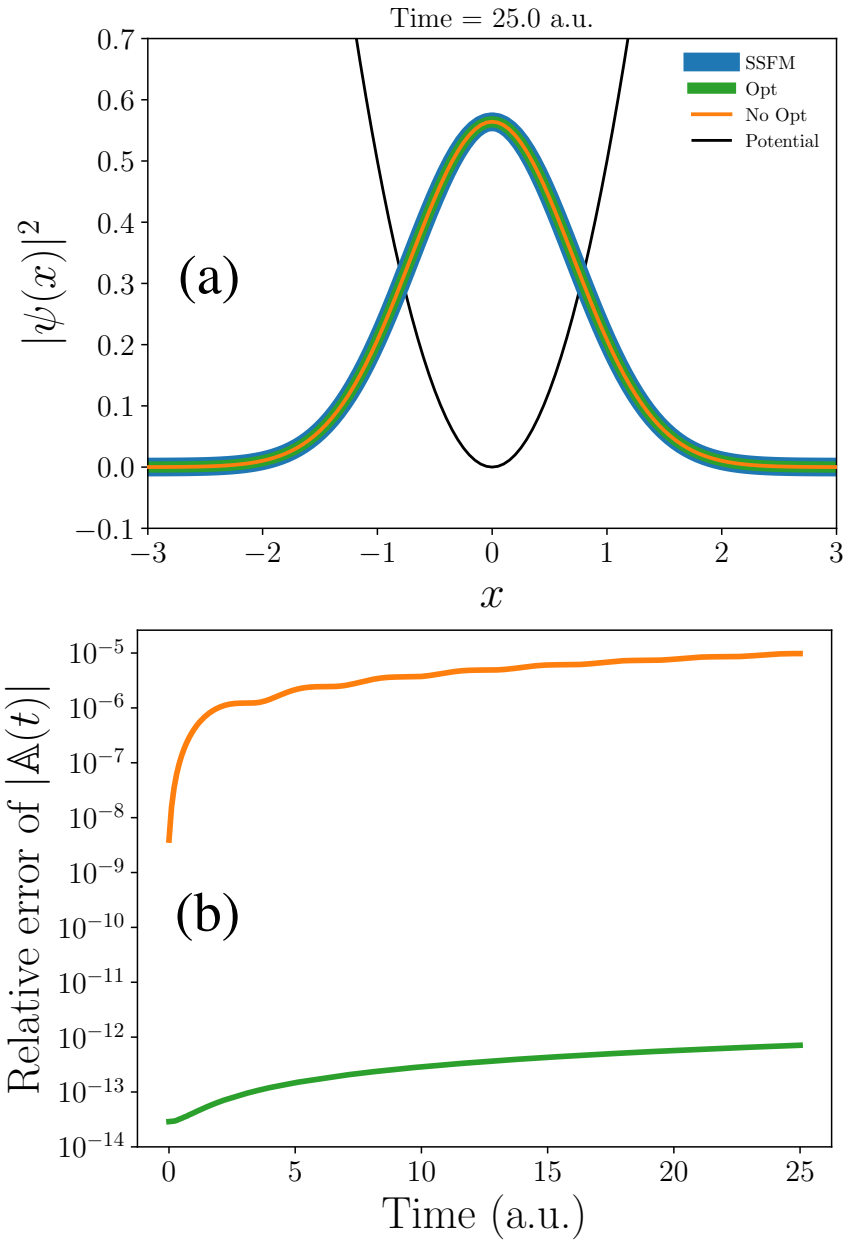

Figure 4.1 The ground state time evolution of the 1D harmonic oscillator using a single s-type GTO. (a) The probability density at time t as specified on top of the figure. (b) The relative error of the absolute value of the auto-correlation function $|\mathbb{A}(t)|$ during the time evolution with the SSFM result (the blue thick line in (a)) as the benchmark. The black line in (a) plots the potential. The orange lines correspond to the unoptimized s-type GTO. The green lines are related to the s-type GTO optimized at each time step in 10 iterations.

As reported in Table 4.1 (a), and plotted Fig. 4.1 (b), optimizing the single s-type GTO during the time evolution process brings about seven orders of magnitude higher accuracy for the absolute value of the auto-correlation function, $|\mathbb{A}(t)|$. Hence, we conclude that

our optimization approach compensates for the intrinsic error of the Strang split-operator method.

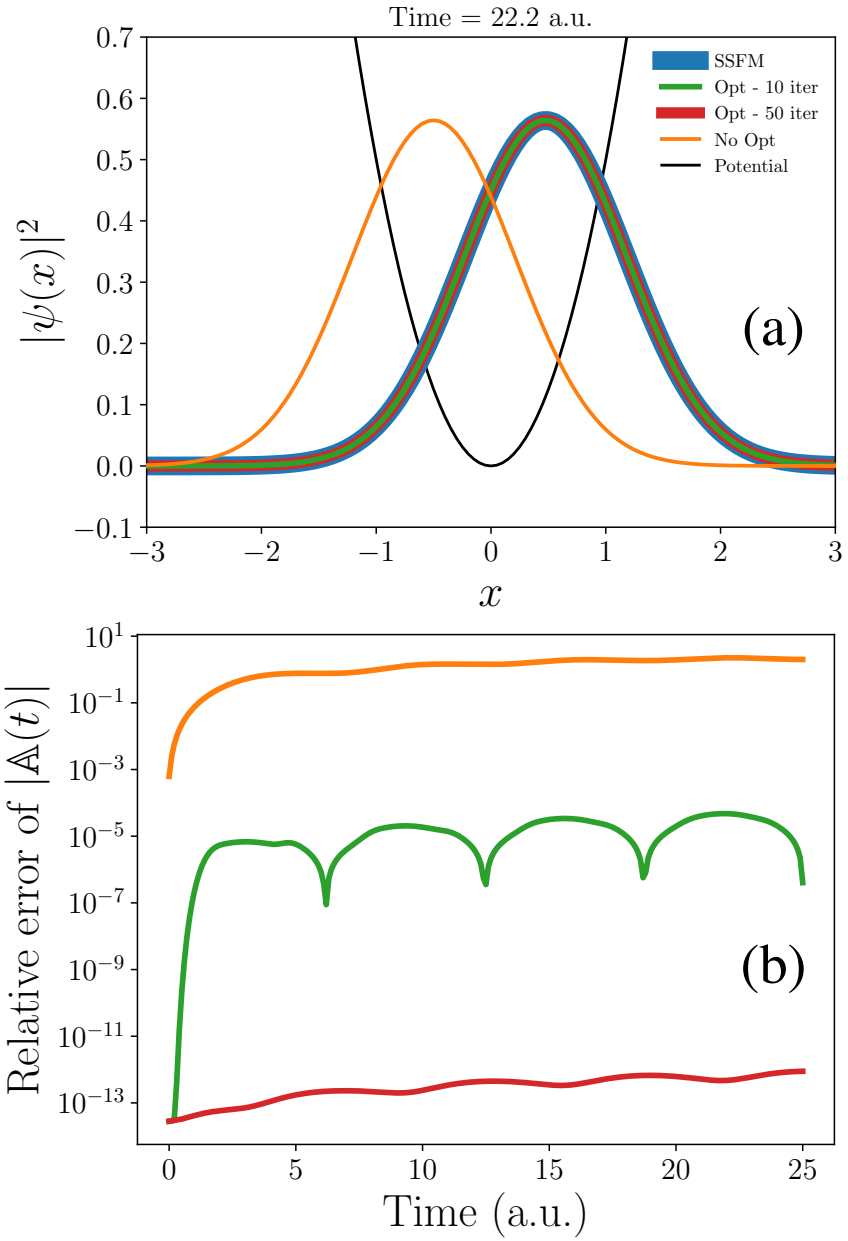

Figure 4.2 As Fig. 4.1 but for the ground state wave function of the 1D harmonic oscillator shifted along the x-axis by -0.5 (a.u.). The red lines correspond to the optimized s-type GTO increasing the number of iterations to 50.

Next, to create a non-eigenstate wave function, we have shifted the initial ground state wave function along the x axis to the left by -0.5 (a.u.). For the time evolution of this wave function, in Table 4.1 (b), and Fig. 4.2, we compare the results of the unoptimized s-type GTO, and two optimized ones that are calculated doing 10 and 50 iterations at each time step. Fig. 4.2 (a) depicts the probability density of the wave function at time $t = 22.2$ (a.u.) at which the maximum difference between the unoptimized and the SSFM results occurs. The new wave function goes back and forth four times during the time evolution. As depicted

in Fig. 4.2 (a), the probability density from the unoptimized (time-independent) s-type GTOs is in complete disagreement with those of the optimized ones (the green line with 10 iterations and the thick red line with 50 iterations). We witness an accuracy improvement in the auto-correlation function from the s-type GTOs optimized in 10 iterations, the green line depicted in Fig. 4.2 (b), whenever the wave function comes back to the initial state. As mentioned in Table 4.1 (b), decreasing the time step to $dt = 0.01$ did not yield a better result than 4.81×10^{-6} for the relative error maximum value of $|\mathbb{A}(t)|$ optimizing the single s-type GTO. From Table 4.1 (b), and Fig. 4.2 (b), one can note the significant improvement of the auto-correlation function accuracy (more than 13 orders of magnitude) from the unoptimized GTO to the optimized one with 50 iterations.

Now, we explore the time evolution of the 2^{nd} excited state represented by five s-type GTOs. The initial configuration is obtained from the time-independent optimization procedure explained in Sec. 3.1. Beginning with the initial configuration of $X_{max} = 2.0$, $\alpha_{ini} = 2.0$, and the correction percentages of $h_x = h_\alpha = 0.9$, resulted in the accuracy of 7.45×10^{-11} for the 2^{nd} excited state energy after the time-independent optimization procedure.

Table 4.2 The 2^{nd} excited state time evolution of the 1D harmonic oscillator using five optimum s-type GTOs. The second column provides the relative error maximum value of $|\mathbb{A}(t)|$ during the whole time evolution $T = 25$ (a.u.).

(a) As an eigenstate of the system

	dt	max RE($\lvert\mathbb{A}(t)\rvert$)	no. iter
No Opt	0.1	1.09×10^{-7}	-
Full Opt	0.1	3.83×10^{-9}	10

(b) The position shifted wave function

	dt	max RE($\lvert\mathbb{A}(t)\rvert$)	no. iter
No Opt	0.1	0.87	-
Full Opt	0.1	2.34×10^{-5}	4
Full Opt	0.01	3.56×10^{-7}	4
Position Opt	0.1	1.67×10^{-7}	4

As we reported in Table. 4.2 (a), and depicted in Fig. 4.3 (b), although we see a nice agreement in the probability density in Fig. 4.3 (a), using unoptimized s-type GTOs for the 2^{nd} excited state time evolution leads to a lower accuracy for the auto-correlation function than what we obtain optimizing them in 10 iterations at each time step of the time-dependent process. Similar to the ground state, we compensate the Strang splitting error in the time evolution of an eigenstate by optimizing the s-type GTOs. Moreover, the fluctuations in the

auto-correlation function obtained from the unoptimized GTOs, the orange line in Fig. 4.3 (b), are mainly because of the same error.

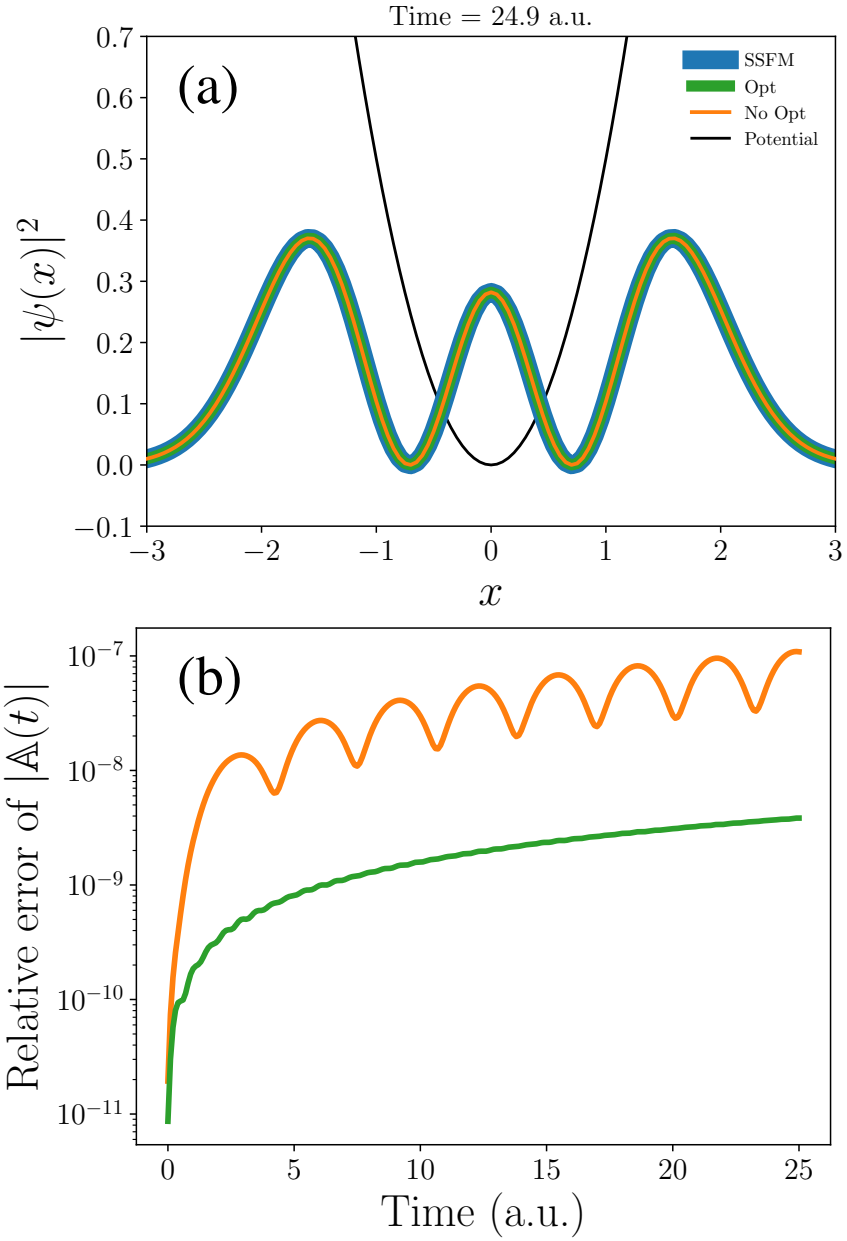

Figure 4.3 As Fig. 4.1 but for the 2^{nd} excited state time evolution of the 1D harmonic oscillator using five optimum s-type GTOs.

Again, to generate a non-eigenstate, we shift the 2^{nd} excited state wave function along the x axis to the left by -0.5 (a.u.). In Fig. 4.4 (a), we have plotted the probability density of this wave function at time $t = 21.6$ (a.u.) calculated from the (time-independent) unoptimized s-type GTOs (the orange line), the full optimization of the s-type GTOs (the green line), and the center-position optimized ones (the thick red line). As opposed to the optimized results, the unoptimized one is not coherent with the exact SSFM result (the thick blue line).

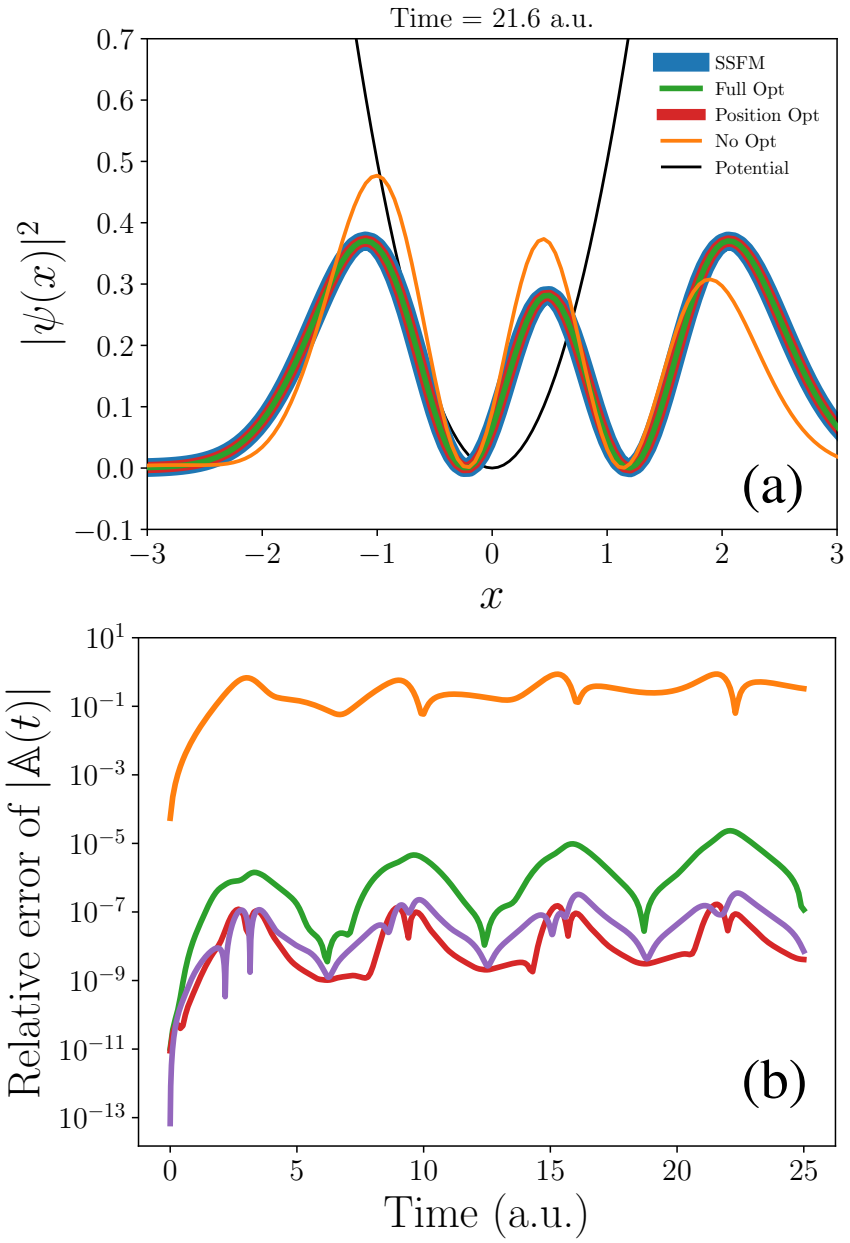

Figure 4.4 As Fig. 4.1 but for the 2^{nd} excited state wave function of the 1D harmonic oscillator shifted along the x-axis by -0.5 (a.u.). Here, the number of optimization iterations is equal to 4. The red lines are obtained optimizing only the center-positions of s-type GTOs. The purple line in (b) is calculated doing full optimization and decreasing the time step from $dt = 0.1$ (a.u.) to $dt = 0.01$ (a.u.).

In addition, as reported in Table. 4.2 (b), and delineated in Fig. 4.4 (b), there is a huge difference in accuracy between the unoptimized s-type GTOs and the optimized ones. In Fig. 4.4 (b), we have shown that optimizing only the center-positions of the s-type GTOs (the red line) brings about a more accurate result compared to the one obtained from full optimization of both of the exponents and the center-positions (the green line). The result from the position optimization is even better than the one from the full optimization with the lower time step $dt = 0.01$ (the purple line). The four main fluctuations in the auto-correlation functions are related to the wave function traveling four times forward and backward along

the x-axis during the whole time evolution interval $T = 25$ (a.u.). In Fig. 4.5 (a) and (b), we have plotted the time-dependent trajectory of the s-type GTOs calculated from the position optimization (the red lines in Fig. 4.4) and from the full optimization (the green lines in Fig. 4.4), respectively. We have denoted the initial s-type GTOs by the light circles and the final ones by the solid diamonds. One can note in Fig. 4.5 (b) that the position optimized s-type GTOs end up exactly on their initial positions. Comparing the results of these two optimization approaches, because of more numerical stability, allowing just for the position corrections leads to higher accuracy for the auto-correlation function in a simpler manner. The instability issues of the full optimization approach could be improved in the future.

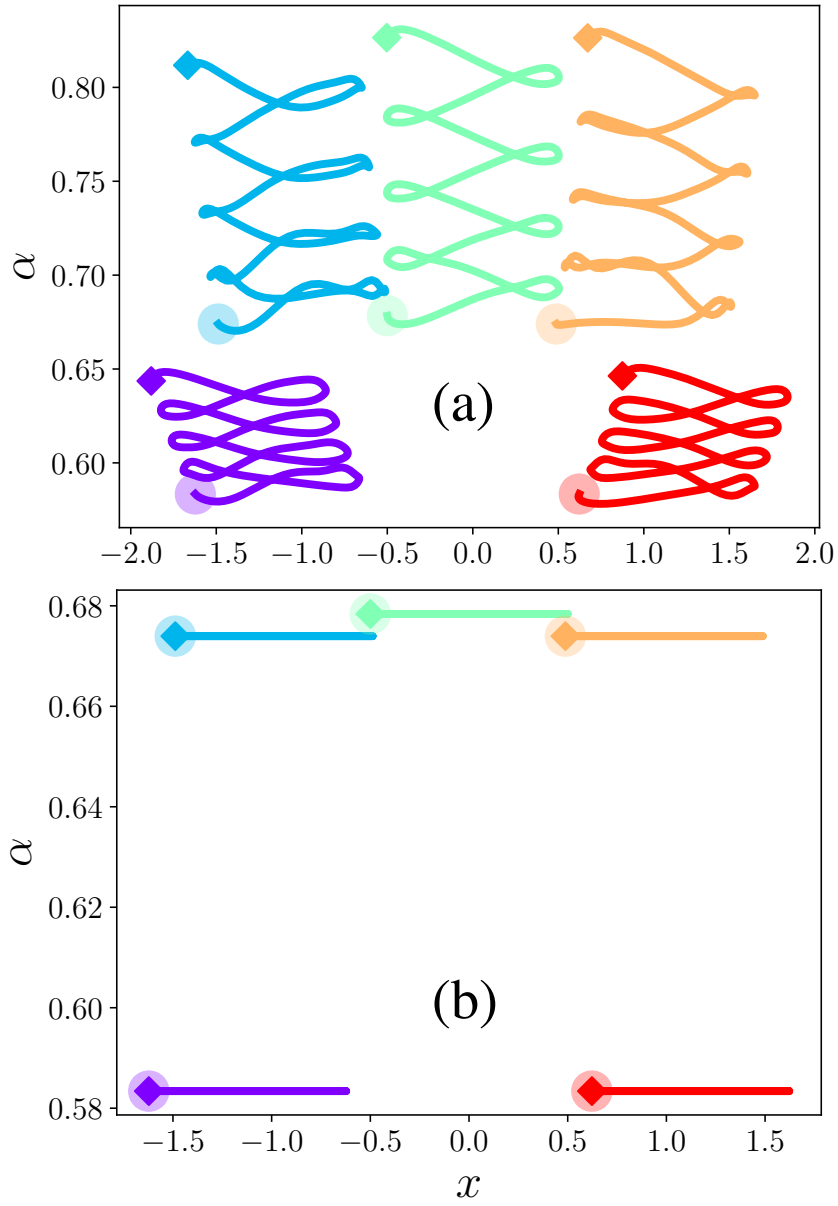

Figure 4.5 Time dependent optimization procedure of the five s-type GTOs used for the shifted 2^{nd} excited state time evolution of the 1D harmonic oscillator. (a) Full optimization (the green line in Fig. 4.4). (b) Optimizing only the center-positions (the red line in Fig. 4.4).

4.3 High-order harmonic generation using s-type GTOs

As the last and most important part of this thesis, we examine the performance of our developed optimization approach for HHG spectra of the 1D Hydrogen atom (Sec. 4.3.1) and the 1D Hydrogen molecular ion at the internuclear distance $R = 2.0$ a.u. (Sec. 4.3.2) experiencing a 5-cycle 800 nm intense laser field.

In this chapter, to calculate the HHG spectrum $D(\omega)$, we compute the squared magnitude of the Fourier transforms of the electron dipole acceleration expectation value in the length gauge. Here, to eliminate the nonphysical effects which occur in the numerical simulations getting interference between the wave packet in the interior region and the reflections from the grid boundaries [91], we employ a complex absorbing potential (CAP)

$$V_{CAP} = -ia|x - x_c|^b \Theta(\pm(x - x_c)), \tag{4.22}$$

where Θ is the Heaviside function. Parameters a, b, and x_c denote the CAP strength, the CAP order and the CAP position. We found this type of absorbing boundary more efficient and easier to tune than the mask function employed in Sec. (2.42). For the HHG calculations in this chapter, we have used the absorber parameters of $a = 0.0016$, $b = 2$, and x_c equal to 2.5 $\times$ the quiver radius, which is the excursion amplitude in the oscillatory motion of the electron, $\frac{E_0}{\omega^2}$, where E_0 is the magnitude of the electric field and ω is the laser frequency. These parameters serve our purpose of getting agreement with the exact results regardless of the studied system (H atom or H_2^+ ion) or the intensity and the envelope shape of the external laser field. We just need to use a sufficient number of s-type GTOs for each scenario. Using larger CAP positions makes no considerable difference in the spectra up to 3-5 harmonic orders after the cut-off predicted by the Lewenstein model. It only brings about longer tails for the HHG spectra.

In the following sections, we initiate the time evolution process from a set of equidistantly distributed s-type GTOs that accurately represent the ground state wave function of the system. To avoid possible numerical issues such as the linear dependency problems during the time evolution of the studied systems in the next sections, we optimize the s-type GTOs in a more numerically stable manner. We compute all the center-position corrections using the procedure explained in Sec. 4.1.1. However, when we update the positions at each time step, we compute the mean correction, averaging over all the calculated position corrections, $\overline{\delta} = h_x \sum_{n=1}^{N} \delta_n / N$, and re-distribute the s-type GTOs in the real space equidistantly again increasing their distance from $dx_{old} = x_{n+1} - x_n$ to $dx_{new} = dx_{old} + 2\mathcal{R}(\overline{\delta})$, where dx_{new} is the new distance between the real parts of the center-positions, and dx_{old} is their last one. Since the calculated corrections are complex, to keep the positions of the s-type GTOs complex and not to lose the small but positive effects of the imaginary part of the mean correction, we add $\mathcal{I}(\overline{\delta})$ to the position of all the s-type GTO. In addition, we adjust their widths accordingly without employing any d-type GTOs that we used so far for optimizing

the exponents of the s-type GTOs. At each optimization iteration of the center-positions, we update all the exponents of the s-type GTOs by dividing their last common value by the relative distance between the real parts of the positions, $\alpha_{new} = \alpha_{old}/(dx_{new}/dx_{old})$. This way, the covered physical region is widened and narrowed intelligently during the time-dependent procedure. Whenever the s-type GTOs are distributed more widely, their widths are also increased correspondingly. On the contrary, when the distance between the s-type GTOs gets lower, their exponents get higher, and consequently, their widths become narrower.

In all of the following sections, we have used the initial inter-distance of $dx_{ini} = 0.4$ (a.u.), the initial exponents of $\alpha_{ini} = 3.0$ (a.u.). The corresponding initial configuration result in a highly accurate ground state wave function. At each time step, the optimization procedure is done in 4 iterations adjusting the position correction percentage of $h_x = 0.05$

4.3.1 1D Hydrogen atom with a soft-core potential

As the first laser-induced scenario, using $N = 101$ equidistantly distributed s-type GTOs, we study the HHG spectrum in the 1D Hydrogen atom with the soft-core potential employed in Sec. 3.2.3. We use a 5-cycle 800 nm laser field with the intensity of $I = 10^{14}$ W/cm^2 and a Gaussian envelope shape. This laser pulse contributes to the quiver radius of 16.45 (a.u.) at the peak intensity. Employing Eq. (2.35), the corresponding cutoff harmonics predicted by the 3-step and the Lewenstein models are 21 and 23, respectively. $N = 101$ equidistantly distributed s-type GTOs result in the relative error of 3.98×10^{-13} for the ground state energy.

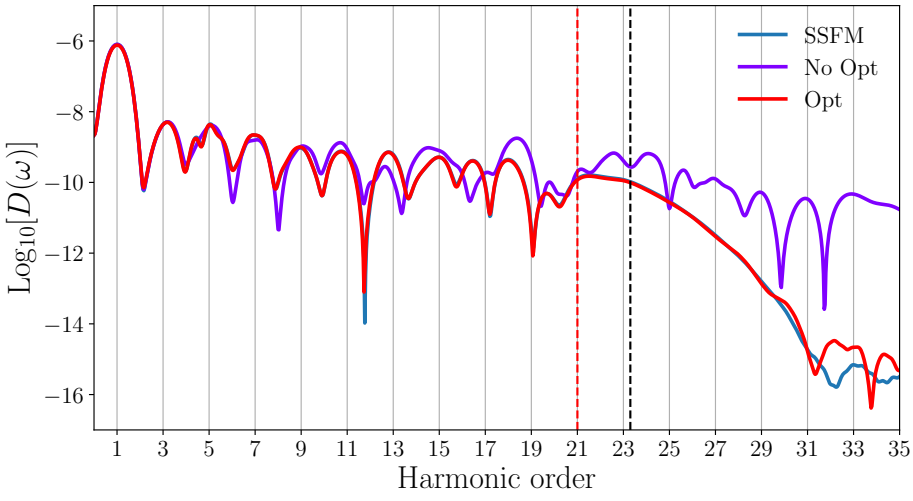

Figure 4.6 The HHG spectrum from the 1D Hydrogen atom induced by a Gaussian envelope-shaped 5-cycle 800 nm laser field with the intensity of $I = 10^{14}$ W/cm^2 employing 101 equidistantly distributed s-type GTOs. The blue line depicts the reference result computed using the SSFM method. The purple line corresponds to the unoptimized s-type GTOs. The red line is obtained by optimizing the s-type GTOs during the time evolution process. The red and black vertical dashed lines plot the cut-off harmonics, predicted by the 3-step and the Lewenstein models, respectively.

In Fig. 4.6, we have compared the HHG resulted from the unoptimized equidistantly distributed s-type GTOs and the ones that we optimize during the time evolution process. We have used the SSFM method as our benchmark. As it is evident in Fig. 4.6, we obtain excellent agreement between the optimized and the SSFM results up to the last few harmonics. In contrast, the HHG spectrum from the unoptimized GTOs does not even agree with the SSFM one in the plateau region after the first few harmonics.

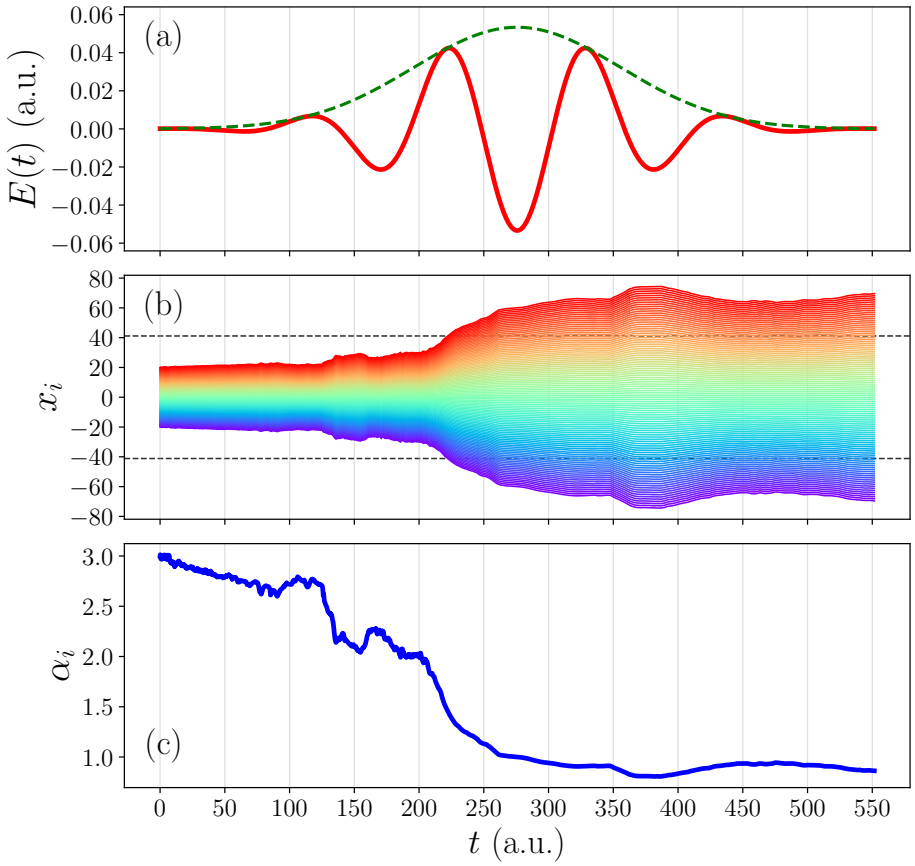

Figure 4.7 The 1D Hydrogen atom: (a) The used Gaussian envelope-shaped 5-cycle 800 nm laser field with the intensity of $I = 10^{14}$ W/cm^2. The envelope function is denoted by the green dashed line. (b) The time-dependent trajectories of the center-positions of the optimized s-type GTOs. (c) Their adjusted exponents. The two black horizontal dashed lines in (b) show the CAP positions, which are $\pm$ 2.5 $\times$ the quiver radius.

To understand the reason for the discrepancy of the HHG spectrum from the unoptimized s-type GTOs and the SSFM one, we have delineated in Fig. 4.7 (a) the used laser profile, (b) the time-dependent optimization trajectories of the center-positions of the equidistantly distributed s-type GTOs, and (c) their adopted exponents. From Fig. 4.7 (b), we can see how the optimized s-type GTOs cover a larger physical region when needed. Their distance is increased up to almost four times the initial one during the time-dependent procedure. When the laser field reaches the peak amplitude, we experience the most considerable widening of the basis set.

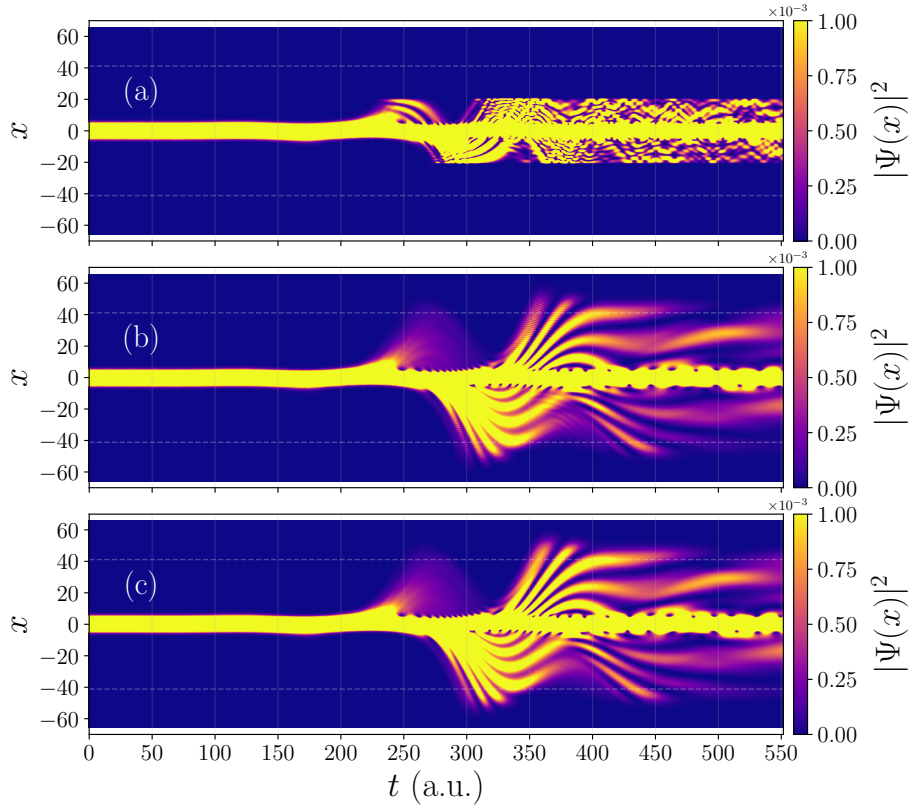

Figure 4.8 The 1D Hydrogen atom: probability density from (a) unoptimized s-type GTOs, (b) optimized s-type GTOs, and (c) SSFM. The two light horizontal dashed lines denote the CAP positions.

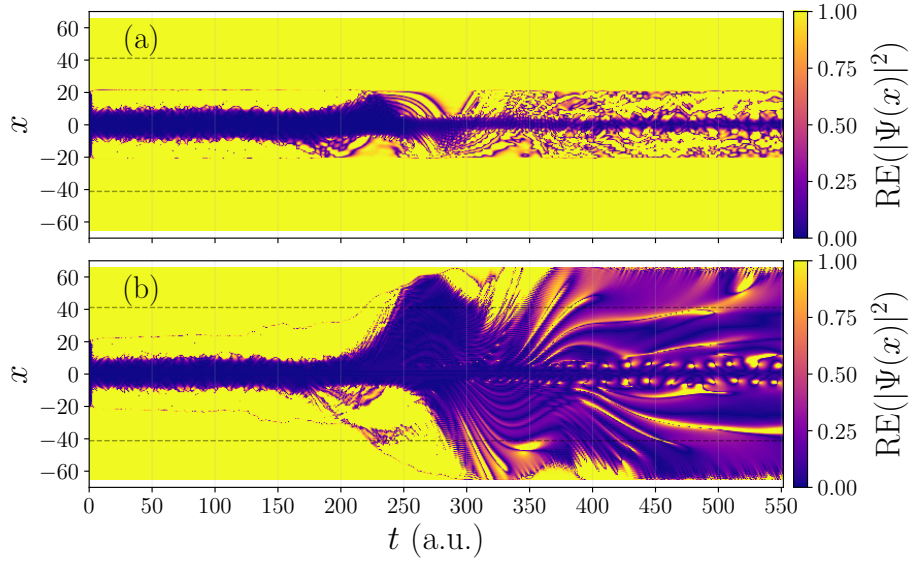

Figure 4.9 The 1D Hydrogen atom: the relative error of the probability density from (a) unoptimized s-type GTOs, (b) optimized s-type GTOs. The two dark horizontal dashed lines depict the CAP positions.

Afterwards, the distance between the s-type GTOs does not change significantly. As can be seen in Fig. 4.7 (c), the exponents are adjusted accordingly. The larger the distance between the s-type GTOs, the smaller their exponents (the larger the widths). One can also note in

Fig. 4.7 (b) that the CAP absorbers at $\pm$ 2.5 $\times$ the quiver radius do not abruptly absorb the wave function, and there are still some parts of the wave function on the wings (as will be shown in Fig. 4.8) that should be appropriately represented. For this reason, we see the s-type GTOs are distributed more widely (up to about $\pm$ 4.5 $\times$ the quiver radius) to cover the areas beyond the CAP positions.

In Fig. 4.8, we have compared the probability densities resulting from (a) the unoptimized s-type GTOs, (b) the optimized ones, and (c) the SSFM. We have suppressed the high probability densities to make the ionization fraction and the subtle differences visible. Moreover, in Fig. 4.9, we have plotted the corresponding relative errors. As it is apparent in Fig. 4.8 (a), the space covered by the unoptimized s-type GTOs is too small, and they are unable to capture the wave function. In contrast, the optimized ones spread time-dependently in space adjusted to the dynamics. The resulting wave function compares favorably to the SSFM one, as plotted in Fig. 4.8 (b). From Fig. 4.9, it can also be conceived that optimized s-type GTOs (b) lead to much more accurate results than the unoptimized ones (a), especially when the wave function has spread. Furthermore, as can be seen in Figs. 4.8, and 4.9, s-type GTOs are required on both sides, and after the initial fluctuations synchronous with the laser pulse amplitude, the wave function becomes symmetric. This shows that the symmetric collective optimization scheme of our approach is valid.

4.3.2 1D ionized Hydrogen molecule with a soft-core potential

Ultimately, as motivated in the introduction part of Chap. 3, to address the issues that we experienced in the 3D H_2^+ after the cutoff using a high number of static coherent states in Sec. 2.3.1, we have applied our time-dependent optimization approach for investigating HHG

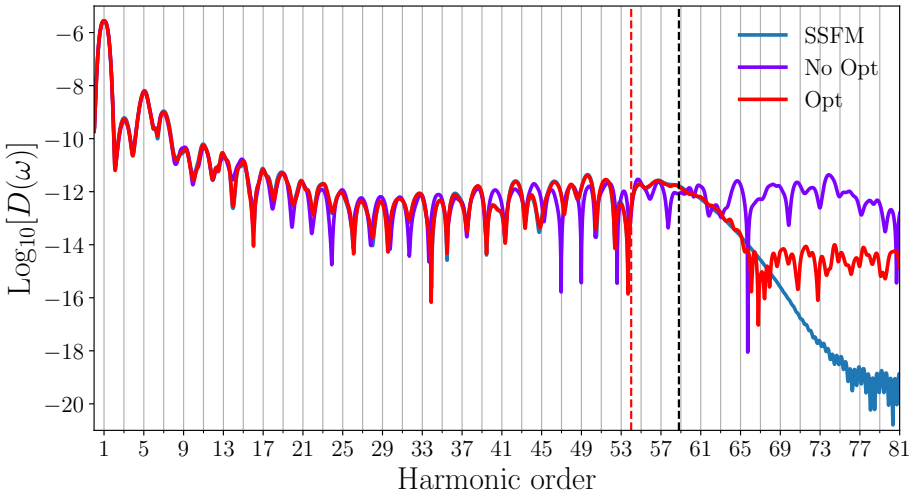

Figure 4.10 The HHG spectra from the 1D Hydrogen molecular ion H_2^+ at the internuclear distance $R = 2.0$ (a.u.) introduced to a $\sin^2$ envelope-shaped 5-cycle 800 nm laser field with the intensity of $I = 3 \times 10^{14}$ W/cm^2 using $N = 181$ equidistantly distributed s-type GTOs. This figure shares the general properties of Fig. 4.6.

in the 1D ionized Hydrogen molecular ion H_2^+ at the inter-nuclear distance $R = 2.0$ (a.u.) exposed to a $\sin^2$ envelope-shaped 5-cycle 800 nm laser pulse with the intensity of $I = 3 \times 10^{14}$ W/cm^2. For this intensity, we have used $N = 181$ equidistantly distributed s-type GTOs, which bring about the relative error of 10^{-12} for the ground state energy. The mentioned laser field corresponds to the quiver radius of 28.50 (a.u.), and the cutoff harmonics of about 54, and 59 predicted by the 3-step and the Lewenstein models, respectively.

In Fig. 4.10 we have depicted the HHG spectrum calculated from the optimized equidistantly distributed s-type GTOs and the unoptimized ones in comparison with the SSFM result. As one can see from Fig. 4.10, our optimization approach achieves a nice agreement with the SSFM results up to 5-7 harmonic orders after the cutoff predicted by the Lewenstein model. Using only $N = 181$ s-type GTOs, we obtained good agreement over 3-4 orders of magnitude in the cutoff drop. In contrast, the unoptimized HHG spectra are inadequate for covering the time-dependent physical region and obtaining an agreement with the SSFM results even for the plateau harmonics before the cutoff.

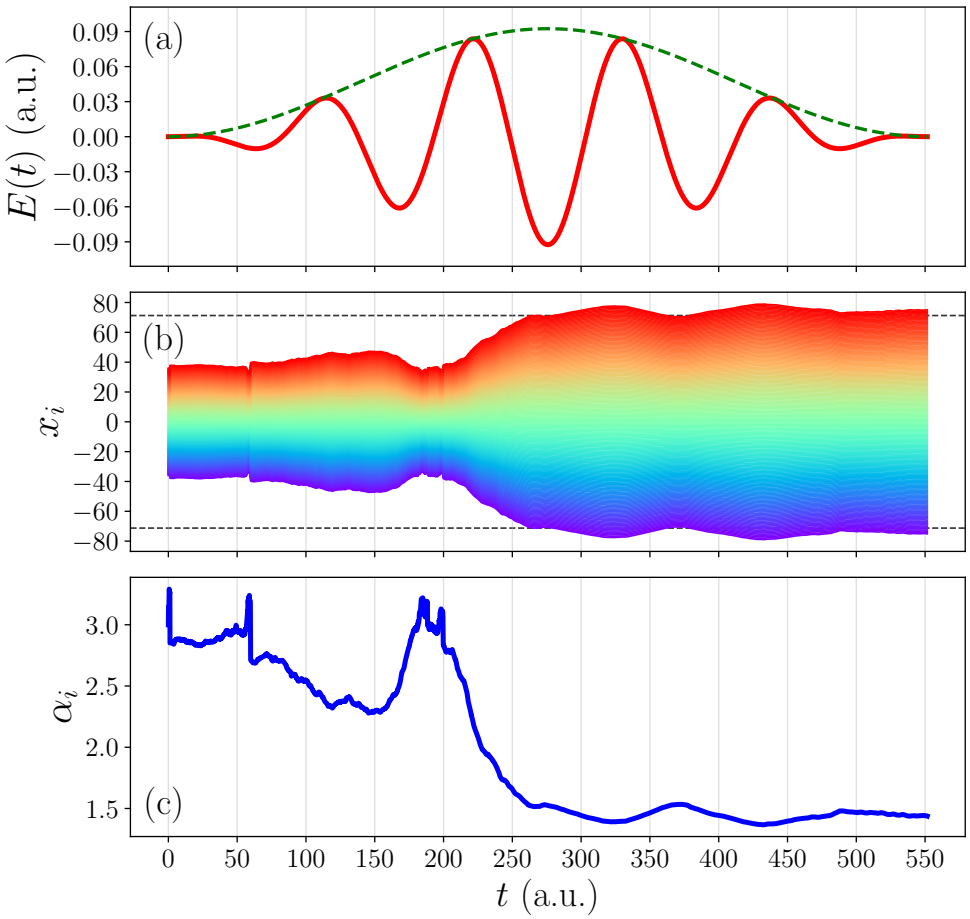

Figure 4.11 The 1D Hydrogen molecular ion H_2^+ at the internuclear distance $R = 2.0$ (a.u.): (a) The employed $\sin^2$ envelope-shaped 5-cycle 800 nm laser field with the intensity of $I = 3 \times 10^{14}$ W/cm^2. (b) The time-dependent trajectories of the center-positions of the optimized s-type GTOs. (c) Their adjusted exponents. This figure has the same properties as Fig. 4.7.

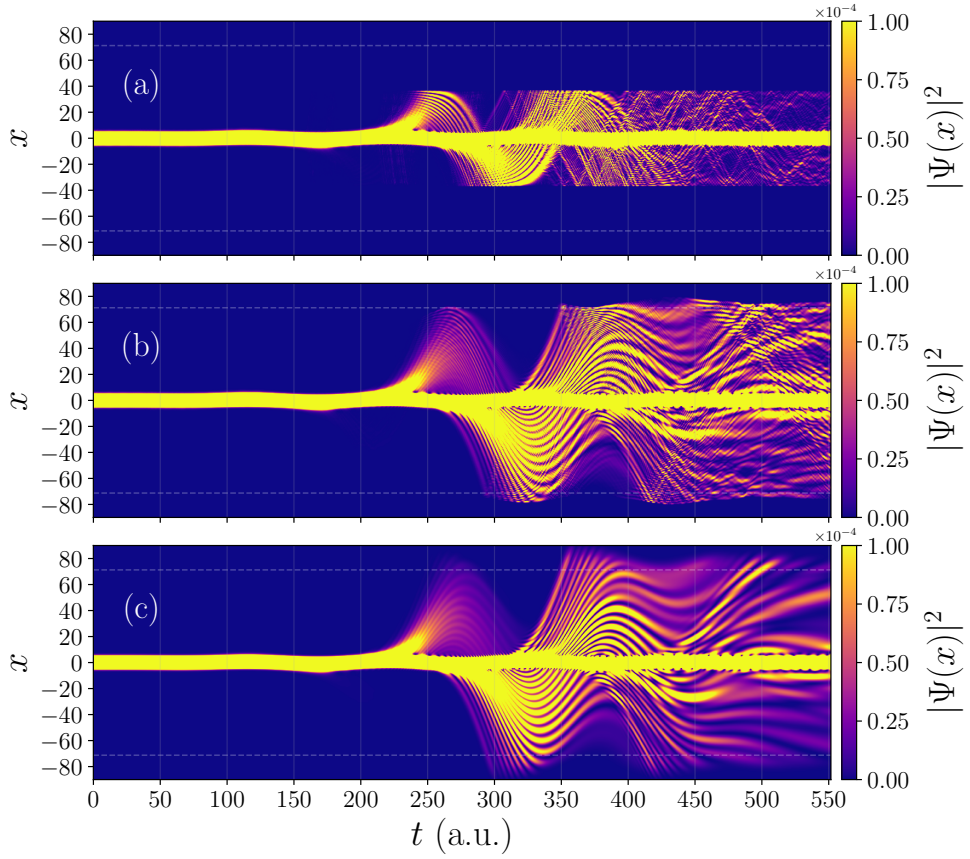

Figure 4.12 The 1D Hydrogen molecular ion H_2^+ at the internuclear distance $R = 2.0$ (a.u.): probability density from (a) unoptimized s-type GTOs, (b) optimized s-type GTOs, and (c) SSFM. The two light horizontal dashed lines delineate the CAP positions.

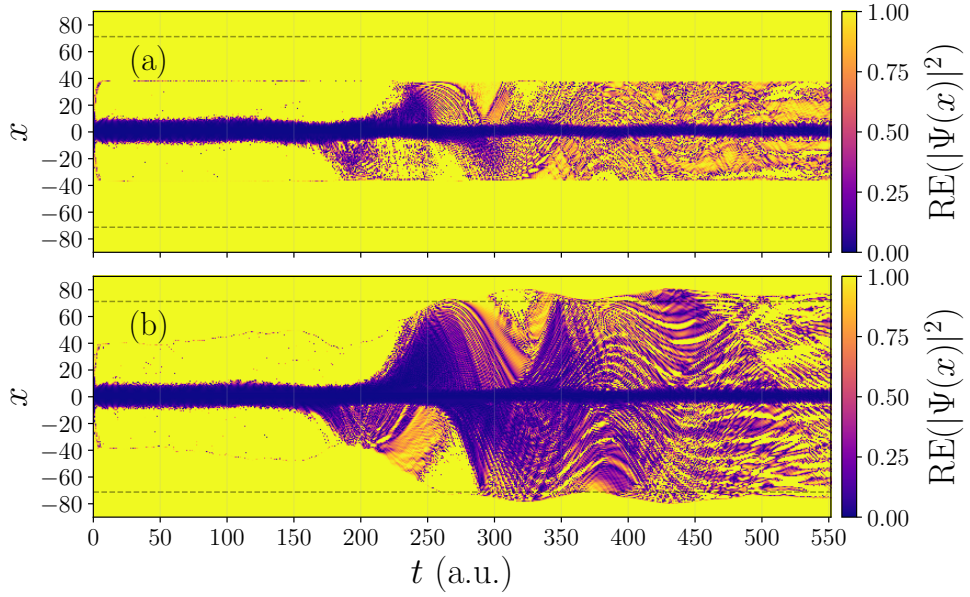

Figure 4.13 The 1D Hydrogen molecular ion H_2^+ at the internuclear distance $R = 2.0$ (a.u.): the relative error of the probability density from (a) unoptimized s-type GTOs, (b) optimized s-type GTOs. The two dark horizontal dashed lines show the CAP positions.

In Fig. 4.11, we have delineated the employed laser profile (a), the time-dependent

optimization procedure of the s-type GTOs for (b) the center-positions of $N = 181$ s-type GTOs, and (c) their corresponding exponents. As it is notable from Fig. 4.11 (b), expansion and contraction of the s-type GTOs happen multiple times during the time evolution process. Similar to what was mentioned for the 1D Hydrogen atom (Fig. 4.7), the largest spreading of the s-type GTOs occurs close to the peak amplitude of the laser pulse, after which the s-type GTOs do not undergo significant changes as the basis set is already wide enough to cover the physical region. We also note that as the wave function has non-zero values on the wings beyond the absorber positions, the s-type GTOs are automatically spread (up to about $\pm$ 2.7$\times$ the quiver radius) so that they represent the wave function best.

We have plotted in Figs. 4.12, and 4.13, the probability densities of the 1D H_2^+ and their corresponding relative errors with respect to the SSFM from (a) the unoptimized s-type GTOs, and (b) the optimized ones. What we discussed in the last paragraph of the previous section for the probability densities of the Hydrogen atom essentially carries over for the 1D H_2^+ . A subtle feature that makes the H_2^+ problem more intricate is the possible interference due to the two ions. Here, one sees slight differences between the optimized s-type GTOs (stronger interference pattern) and the SSFM wave function, which are absent in the atomic case.

5 Conclusions and Outlooks

Seeking a proper and efficient way of using Gaussian wave packets for directly solving the time-dependent Schrödinger equation (TDSE), we first employed static coherent states (SCS) for representing the electronic wave function of single-electron atomic and molecular systems subjected to intense laser fields in a different range of frequencies. Doing so, we studied the molecular dissociation and the charge migration in the 3D Hydrogen molecular ion H_2^+ exposed to a high-frequency laser pulse treating the nuclei classically. We calculated the related potential energy curves of H_2^+ in the absence and presence of the external laser field and found substantial charge localization as the molecular bond distance was increased. This charge localization was reflected in the exponential increase in the expected charge migration period as a function of the bond length.

Next, we employed a high number of SCS for full-dimensional quantum simulation of high-order harmonic generation (HHG) process in H_2^+ at two different internuclear distances introduced to linearly polarized low-frequency intense laser pulses both in the length and velocity gauges. In addition, we studied the single attosecond pulse (SAP) generation in H_2^+ using the polarization gating technique, which combines two delayed counter-rotating circular laser pulses and opens up a gate at the central portion of the superposed pulse. Although the SCS method can be potentially suggested for full-dimensional quantum simulation of higher dimensional systems such as the Hydrogen molecule exposed to an external intense laser field, it fell short to reach a good agreement for the HHG spectra of H_2^+ with those of a 3D unitary split-operator (USO) solver keeping the number of employed SCS small enough to make it computationally feasible for systems with higher degrees of freedom (DOF). To construct a more suitable basis, we developed an approach to guide a set of Gaussian wave packets in such a way that the number of used basis functions is kept as low as possible while maintaining high accuracy.

We introduced a computationally robust and efficient procedure for optimizing both of the exponents α_i and the center-positions $\mathbf{r}_i$ of the simplest Gaussian basis functions, the s-type Gaussian-type orbitals (GTOs), by employing two auxiliary higher-type GTOs resulted from the first-order Taylor expansion. We applied our developed optimization approach for accurately representing a desired electronic state wave function of different quantum systems: the 1D harmonic oscillator, the 1D Morse oscillator, the 1D Hydrogen atom, the 1D

Hydrogen molecular ion, the 3D Hydrogen atom, and the 3D H_2^+ . We compared our results of optimizing a low number of s-type GTOs to other approaches which use a high number of different types of non-optimized GTOs. We showed that one needs a considerably lower number of the optimized s-type GTOs to obtain highly accurate electronic state energies. Our approach optimizes not only the distributed s-type GTOs but also the atomic-centered (even-tempered) s-type GTOs and their combinations.

Integrating our optimization approach into the time evolution process of the wave function, we firstly assessed its performance for computing the time-evolved ground and second excited states wave functions of the harmonic oscillator. For these two eigenstates of the studied system, we showed that our optimization approach compensates for the intrinsic error of the Strang splitting of the time evolution operator resulting in more accurate results for the auto-correlation function than the non-optimized case. Moreover, for non-eigenstate initial wave functions, we demonstrated how our optimization approach guides the used s-type GTOs at each time step bringing about a significant agreement with the exact result where the non-optimized s-type GTOs fail to represent the time-dependent wave function properly.

Finally, coming back to HHG studies in atomic and molecular systems exposed to intense laser fields, we applied a numerically more stable version of our optimization technique to investigate HHG in the 1D Hydrogen atom and the 1D H_2^+ . We introduced an expansion and contraction optimization scheme in which, at each time step of the time evolution process, the s-type GTOs are re-distributed equidistantly. We used a relatively small number of equidistantly distributed s-type GTOs constructed in a small spatial region. Initially, they result in a highly accurate ground state energy for the studied system. We showed how the optimized s-type GTOs are naturally guided in a wider physical region when needed. We also illustrated that the most considerable widening of the basis set occurs as the laser field reaches the peak amplitude, after which their distribution is not significantly expanded until the end of the time-dependent process. The HHG spectra obtained from the time-dependent optimized s-type GTOs exhibit an excellent agreement with the exact results while the unoptimized ones were unable to achieve such agreement even in the plateau region of the spectrum after the first few harmonic orders.

The obvious next step would be to extend the introduced time-dependent optimization approach to 3D problems. Moreover, since this approach can handle ionized propagating wave packets, it can also be implemented for studying above-threshold ionization. In addition, due to the small numbers of the optimized basis functions, it should be possible to tackle more complicated systems such as the Hydrogen molecule considering both electrons active.

Appendices

A Atomic units

The appearance of expressions in atomic physic is greatly simplified using the so-called Hartree atomic units (a.u.) which are known as the units in the electron's world. The prerequisite for specifying atomic units is considering the elementary charge e, the electron mass m, the reduced Planck's constant $\hbar$ (angular momentum), and the Coulomb constant $\frac{1}{4\pi\epsilon_0}$ as unity: $e \equiv m \equiv \hbar \equiv 4\pi\epsilon_0 \equiv 1$. Applying these units in terms of the properties of the simple hydrogen atom, the following important physical quantities can be easily obtained in atomic units:

- **Unit of length:** Bohr radius
$$a_0 = \frac{\hbar^2}{me^2} \equiv 1 \text{ a.u.} = 5.291772108 \times 10^{-11} \text{ m}$$
- **Unit of velocity:** Velocity if an electron in the first Bohr orbit
$$v_0 = \frac{e^2}{\hbar} \equiv 1 \text{ a.u.} = 2.1876912633 \times 10^6 \text{ m/s}$$
- **Unit of time:** Time for an electron to travel a distance of a_0 with a velocity of v_0
$$\tau_0 = \frac{a_0}{v_0} = \frac{\hbar^3}{me^4} \equiv 1 \text{ a.u.} = 2.418884326505 \times 10^{-17} \text{ s}$$
- **Unit of frequency:** Inverse of the unit of time
$$\nu_0 = \frac{1}{\tau_0} = \frac{me^4}{\hbar^3} \equiv 1 \text{ a.u.} = 4.413413733365 \times 10^{16} \text{ Hz}$$
- **Unit of energy:** Hartree energy or twice the binding energy of the hydrogen atom
$$E_h = \frac{me^4}{\hbar^2} \equiv 1 \text{ a.u.} = 4.35974417 \times 10^{-18} \text{ J} = 27.2113962 \text{ eV}$$
- **Unit of electric field strength:**
$$E_0 = \frac{E_h}{ea_0} = \frac{m^2e^5}{\hbar^4} \equiv 1 \text{ a.u.} = 5.14220642 \times 10^{11} \text{ V/m}$$
- **Unit of energy flux (intensity):**
$$I_0 = \frac{cE_0^2}{8\pi} \equiv 1 \text{ a.u.} = 3.50944758 \times 10^{16} \text{ W/cm}^2$$
- **Period of a laser cycle:** In terms of the wavelength of the laser pulse λ (nm)
$$t_{1c}(\text{a.u.}) = \lambda(\text{nm}) \times 0.1378999$$

B SCS method: expectation value of the electron-nucleus attractive forces

The expectation value of the electron-nucleus attractive forces in the basis of static coherent states can be computed by employing Eq. (2.22):

$$\langle \mathbf{F}_{ij} \rangle = \sum_{kl} \mathbf{F}_{ij_{kl}} D_k^* D_l \tag{B.1}$$

where

$$\mathbf{F}_{ij_{kl}} = \left\langle \mathbf{Z}_k \left| \frac{\mathbf{r}_i - \mathbf{R}_j}{|\mathbf{r}_i - \mathbf{R}_j|^3} \right| \mathbf{Z}_l \right\rangle \tag{B.2}$$

are the matrix elements of the attractive Coulombic force on the basis of a static grid of coherent states. To compute $\mathbf{F}_{ij_{kl}}$, implementing the identity operator of coordinate states of electrons leads to

$$\mathbf{F}_{ij_{kl}} = \int\int \langle \mathbf{Z}_k | \mathbf{r}_i \rangle \left\langle \mathbf{r}_i \left| \frac{\mathbf{r}_i - \mathbf{R}_j}{|\mathbf{r}_i - \mathbf{R}_j|^3} \right| \mathbf{r}_i' \right\rangle \langle \mathbf{r}_i' | \mathbf{Z}_l \rangle \, \mathrm{d}\mathbf{r}_i \, \mathrm{d}\mathbf{r}_i' \, . \tag{B.3}$$

Employing the orthogonality in the coordinate representation, $\langle \mathbf{r}_i | \mathbf{r}_i' \rangle = \delta(\mathbf{r}_i - \mathbf{r}_i')$, one gets

$$\mathbf{F}_{ij_{kl}} = \int \langle \mathbf{Z}_k | \mathbf{r}_i \rangle \langle \mathbf{r}_i | \mathbf{Z}_l \rangle \frac{\mathbf{r}_i - \mathbf{R}_j}{|\mathbf{r}_i - \mathbf{R}_j|^3} \, \mathrm{d}\mathbf{r}_i \, . \tag{B.4}$$

Using the fact that coherent states are Gaussian wave packets in the coordinate representation [58, 62]

$$\langle \mathbf{Z}_k | \mathbf{r}_i \rangle = (\frac{\gamma}{\pi})^{3/4} \exp\left(\frac{-\gamma}{2} (\mathbf{r}_i - \frac{\sqrt{2}\mathbf{Z}_k^*}{\gamma^{\frac{1}{2}}})^2 + (\frac{\mathbf{Z}_k^* - \mathbf{Z}_k}{2}) \mathbf{Z}_k^* \right) \tag{B.5}$$

and by applying the Gaussian product rule, Eq. (3.2), it can be verified that

$$\langle \mathbf{Z}_k | \mathbf{r}_i \rangle \langle \mathbf{r}_i | \mathbf{Z}_l \rangle = (\tfrac{\gamma}{\pi})^{3/2} \exp\left(\tfrac{(\mathbf{Z}_k^* - \mathbf{Z}_k)\mathbf{Z}_k^*}{2} + \tfrac{(\mathbf{Z}_l - \mathbf{Z}_l^*)\mathbf{Z}_l}{2} - \tfrac{(\mathbf{Z}_l - \mathbf{Z}_k^*)^2}{2} \right) \exp\left(-\gamma |\mathbf{r}_A|^2 \right) \tag{B.6}$$

where

$$\mathbf{r}_A = \mathbf{r}_i - \mathbf{A} \quad , \quad \mathbf{A} = \frac{\mathbf{Z}_k^* + \mathbf{Z}_l}{\sqrt{2\gamma}} . \tag{B.7}$$

Taking into account the over-completeness property of coherent states (Eq. (2.6)) and then substituting Eq. (B.6) into Eq. (B.4) we get

$$\mathbf{F}_{ij_{kl}} = \langle \mathbf{Z}_k | \mathbf{Z}_l \rangle \, (\frac{\gamma}{\pi})^{3/2} \int \frac{\mathbf{r}_i - \mathbf{R}_j}{|\mathbf{r}_i - \mathbf{R}_j|^3} \exp\big(-\gamma |\mathbf{r}_A|^2\big) \mathrm{d}\mathbf{r}_i. \tag{B.8}$$

Now by substituting the following Laplace transform

$$\frac{1}{|\mathbf{r}_i - \mathbf{R}_j|^3} = \frac{4}{3\sqrt{\pi}} \int_0^\infty \exp\big(t^{-2/3} |\mathbf{r}_i - \mathbf{R}_j|^2\big) \mathrm{d}t \tag{B.9}$$

into Eq. (B.8) and implementing again the Gaussian product rule, we get

$$\mathbf{F}_{ij_{kl}} = \langle \mathbf{Z}_k | \mathbf{Z}_l \rangle \, \tfrac{4\gamma^{3/2}}{3\pi^2} \int_0^\infty \exp\Big(-\tfrac{\gamma t^{2/3}}{\gamma + t^{2/3}} |\boldsymbol{\rho}_{ij}|^2\Big) \int (\mathbf{r}_i - \mathbf{R}_j) \exp\big(-\big(\gamma + t^{2/3}\big) |\mathbf{r}_B|^2\big) \, \mathrm{d}\mathbf{r}_i \, \mathrm{d}t \tag{B.10}$$

where

$$\boldsymbol{\rho}_{ij} = \mathbf{A} - \mathbf{R}_j \quad , \quad \mathbf{r}_B = \mathbf{r}_i - \mathbf{B} \quad , \quad \mathbf{B} = \frac{\gamma}{\gamma + t^{2/3}} \mathbf{A} + \frac{t^{2/3}}{\gamma + t^{2/3}} \mathbf{R}_j. \tag{B.11}$$

One can also show that

$$\mathbf{r}_i - \mathbf{R}_j = \mathbf{r}_B + \frac{\gamma}{\gamma + t^{2/3}} \boldsymbol{\rho}_{ij}. \tag{B.12}$$

Substituting Eq. (B.12) in Eq. (B.10) and applying the well-known 3D Gaussian integral

$$\int \exp\big(-\alpha \mathbf{r}^2\big) \mathrm{d}\mathbf{r} = \Big(\frac{\pi}{\alpha}\Big)^{3/2} \tag{B.13}$$

and considering $\frac{t^{2/3}}{\gamma + t^{2/3}} = u^2$, it is straightforward to verify that

$$\mathbf{F}_{ij_{kl}} = \left(\frac{4\gamma^3}{\pi}\right)^{1/2} \boldsymbol{\rho}_{ij} F_1\big(\gamma |\boldsymbol{\rho}_{ij}|^2\big) \, \langle \mathbf{Z}_k | \mathbf{Z}_l \rangle \tag{B.14}$$

where F_1 is the first order Boys function [92]

$$F_n(x) = \int_0^1 t^{2n} \exp\big(-x t^2\big) \mathrm{d}t. \tag{B.15}$$

C Matrix elements on the basis of GTOs

C.1 1D systems

The following parameters are used in all 1D equations:

$$\begin{aligned}
\gamma_{ij} &= \alpha_i^* + \alpha_j \\
\alpha_{ij} &= \alpha_i^* \alpha_j \\
\beta_{ij} &= \frac{\alpha_{ij}}{\gamma_{ij}} \\
b_{ij} &= \frac{\alpha_i^* x_i^* + \alpha_j x_j}{\gamma_{ij}} \\
\mathbb{K}_{ij} &= e^{-\beta_{ij}\left(x_i^* - x_j\right)^2},
\end{aligned} \tag{C.1}$$

where $\alpha_{i(j)}$ is the exponent and $x_{i(j)}$ is the center-position of the i^{th} (j^{th}) GTO. In the time-independent scenarios, these parameters remain real, while in the time-dependent procedures, they become complex.

To evaluate the **overlap** between the i^{th} a-type GTO, $\mathcal{G}_i^a(x, x_i, \alpha_i) = \mathcal{N}_i^a (x - x_i)^{m_a} e^{-\alpha_i (x - x_i)^2}$, and the j^{th} b-type GTO, $\mathcal{G}_j^b(x, x_j, \alpha_j) = \mathcal{N}_j^b (x - x_j)^{m_b} e^{-\alpha_j (x - x_j)^2}$, with the help of the Gaussian product rule from Eq. (3.2), we get

$$\Omega_{ij}^{ab} = \mathcal{N}_i^a \mathcal{N}_j^b \mathbb{K}_{ij} \int_{-\infty}^{\infty} (x - x_i^*)^{m_a} (x - x_j)^{m_b} e^{-\gamma_{ij}(x - b_{ij})^2} \mathrm{d}x. \tag{C.2}$$

$\mathcal{N}_i^a$ and $\mathcal{N}_j^b$, respectively are the normalization factors associated with the a-, and b-type GTOs mentioned in Eq. (3.8). These normalization factors can be used in the time-independent scenarios where GTOs have real parameters. For the time-dependent cases, as GTOs receive complex parameters and lose their complex differentiability, we are obliged to use unnormalized GTOs, $\mathcal{N}_i^a = \mathcal{N}_j^b = 1$. For s-type GTOs: $m_a = m_b = 0$, for p-type GTOs: $m_a = m_b = 1$, and for d-type GTOs: $m_a = m_b = 2$.

In addition, to evaluate **the Hamiltonian matrix elements**, one must compute

$$\mathrm{H}_{ij}^{ab} = \int_{-\infty}^{\infty} \mathcal{G}_i^{a^*}(x, x_i, \alpha_i)(\mathrm{T} + \mathrm{V}(x))\mathcal{G}_j^b(x, x_j, \alpha_j)\mathrm{d}x. \tag{C.3}$$

where $\mathrm{T} = -\frac{1}{2}\frac{\mathrm{d}^2}{\mathrm{d}x^2}$ is the kinetic energy, and $\mathrm{V}(x)$ is the potential.

For computing **the kinetic energy matrix element** over the i^{th} a-type and the j^{th} b-type GTOs, with the help of the Gaussian product rule from Eq. (3.2), we use

$$\begin{aligned}\mathrm{T}_{ij}^{ab} = \frac{-1}{2}\mathcal{N}_i^a\mathcal{N}_j^b\mathbb{K}_{ij}\int_{-\infty}^{\infty}(x - x_i^*)^{m_a}\big(m_b(m_b-1)(x-x_j)^{m_b-2} - 2\alpha_j(2m_b+1)(x-x_j)^{m_b} \\ + 4\alpha_j^2(x-x_j)^{m_b+2}\big)e^{-\gamma_{ij}(x-b_{ij})^2}\mathrm{d}x.\end{aligned} \tag{C.4}$$

Moreover, to calculate **the potential matrix element** over the i^{th} a-type GTO, $\mathcal{G}_i^a(x, x_i, \alpha_i)$, and the j^{th} b-type GTO, $\mathcal{G}_j^b(x, x_j, \alpha_j)$, employing the Gaussian product rule from Eq. (3.2), one needs to evaluate

$$\mathrm{V}_{ij}^{ab} = \mathcal{N}_i^a\mathcal{N}_j^b\int_{-\infty}^{\infty}(x - x_i^*)^{m_a}e^{-\alpha_i^*\left(x-x_i^*\right)^2}\mathrm{V}(x)(x-x_j)^{m_b}e^{-\alpha_j(x-x_j)^2}\mathrm{d}x. \tag{C.5}$$

This integral is analytically solvable just for simple potentials like the 1D Harmonic oscillator, $\mathrm{V}(x) = \frac{\omega^2x^2}{2}$. For complicated potentials it can be numerically approximated employing the well-known Gauss-Hermite quadrature:

$$\int_{-\infty}^{\infty} f(x)e^{-x^2}\mathrm{d}x \approx \sum_{k=1}^{N_{GH}}\Omega_k f(\zeta_k), \tag{C.6}$$

where Ω_k are the weights, and N_{GH} is the number of the abscissae (nodes) , ζ_k , of the Gauss-Hermite quadrature. With the following change of variable

$$\gamma_{ij}(x-b_{ij})^2 = x'^2 \Rightarrow x' = \pm\gamma_{ij}^{1/2}(x-b_{ij}) \Rightarrow x_\pm = \frac{x'}{\pm\gamma_{ij}^{1/2}} + b_{ij} \Rightarrow \mathrm{d}x_\pm = \frac{\mathrm{d}x'}{\pm\gamma_{ij}^{1/2}},$$

we can exploit the general Gauss-Hermite quadrature weights and abscissae to approximate our integral. Consequently, from Eq. (C.5), we would obtain this general equation

$$\mathrm{V}_{ij}^{ab} = \frac{\mathcal{N}_i^a\mathcal{N}_j^b}{\pm\gamma_{ij}^{1/2}}\mathbb{K}_{ij}\int_{-\infty}^{\infty} f\left(x', m^a, m^b\right)e^{-x'^2}dx', \tag{C.7}$$

where

$$f\left(x', m^a, m^b\right) = \left(\frac{x'}{\pm\gamma_{ij}^{1/2}} + b_{ij} - x_i^*\right)^{m_a}\left(\frac{x'}{\pm\gamma_{ij}^{1/2}} + b_{ij} - x_j\right)^{m_b}\mathrm{V}(\frac{x'}{\pm\gamma_{ij}^{1/2}} + b_{ij}). \tag{C.8}$$

For solving the Gaussian integrals in Eqs. (C.2), and (C.4) and for the matrix elements

of the 1D Harmonic oscillator potential in Eq. (C.5), one can utilize the following general form of 1D Gaussian integrals

$$\int_{-\infty}^{\infty} x^n \exp\bigl(-ax^2\bigr)\mathrm{d}x = \frac{(n-1)!!\pi^{1/2}}{2^{n/2}a^{(n+1)/2}} \qquad , \qquad n = 0, 2, 4, 6, \cdots . \tag{C.9}$$

The mentioned Gaussian integrals can also be analytically solved using computer software like Mathematica.

C.2 3D systems

The following parameters are used in the 3D equations:

$$\begin{aligned}
\gamma_{ij} &= \alpha_i^* + \alpha_j \\
\alpha_{ij} &= \alpha_i^* \alpha_j \\
\beta_{ij} &= \frac{\alpha_{ij}}{\gamma_{ij}} \\
\mathbf{b}_{ij} &= \frac{\alpha_i^* \mathbf{r}_i^* + \alpha_j \mathbf{r}_j}{\gamma_{ij}} \\
\mathbb{K}_{ij} &= e^{-\beta_{ij}\left(\mathbf{r}_i^* - \mathbf{r}_j\right)^2},
\end{aligned} \tag{C.10}$$

where $\alpha_{i(j)}$ is the exponent and $\mathbf{r}_{i(j)}$ is the center-position of the i^{th} (j^{th}) 3D GTO. In addition, in the upcoming equations, $\mathcal{N}_i^a$ and $\mathcal{N}_j^b$, respectively are the normalization factors associated with the a-, and b-type 3D GTOs mentioned in Eq. (3.4). For the 3D unnormalized GTOs, we can simply consider $\mathcal{N}_i^a = \mathcal{N}_j^b = 1$.

To calculate the overlap between the i^{th} a-type and the j^{th} b-type 3D GTOs (Eq. (3.3)), we need to calculate

$$\Omega_{ij}^{ab} = \int \mathcal{G}_i^{a^*}(\mathbf{r}, \mathbf{r}_i, \alpha_i)\mathcal{G}_j^b(\mathbf{r}, \mathbf{r}_j, \alpha_j)\mathrm{d}\mathbf{r}. \tag{C.11}$$

In addition, to evaluate the Hamiltonian matrix elements, one should compute

$$\mathrm{H}_{ij}^{ab} = \int \mathcal{G}_i^{a^*}(\mathbf{r}, \mathbf{r}_i, \alpha_i)(\mathrm{T} + \mathrm{V}(\mathbf{r}))\mathcal{G}_j^b(\mathbf{r}, \mathbf{r}_j, \alpha_j)\mathrm{d}\mathbf{r}. \tag{C.12}$$

where $\mathrm{T} = -\frac{1}{2}\boldsymbol{\nabla}^2$ is the kinetic energy, and $\mathrm{V}(\mathbf{r})$ is the potential.

In the following sections, we explain in detail how to evaluate the matrix elements of the Overlap, the kinetic energy, and the potential over the 3D GTOs.

C.2.1 The overlap matrix elements over 3D s-type GTOs

To compute the overlap between the i^{th} and the j^{th} s-type GTOs, we can write

$$\begin{aligned}
\Omega_{ij}^{ss} = \left\langle \mathcal{G}_i^s \middle| \mathcal{G}_j^s \right\rangle &= \int \mathcal{G}_i^{s^*}(\mathbf{r}, \mathbf{r}_i, \alpha_i)\mathcal{G}_j^s(\mathbf{r}, \mathbf{r}_j, \alpha_j)\mathrm{d}\mathbf{r} \\
&= \mathcal{N}_i^s \mathcal{N}_j^s \int e^{-\alpha_i^*\left(\mathbf{r}-\mathbf{r}_i^*\right)^2} e^{-\alpha_j(\mathbf{r}-\mathbf{r}_j)^2}\mathrm{d}\mathbf{r}.
\end{aligned}$$

Employing the Gaussian product rule from Eq. (3.2), one obtains

$$\Omega_{ij}^{ss} = \mathcal{N}_i^s \mathcal{N}_j^s \mathbb{K}_{ij} \int e^{-\gamma_{ij}(\mathbf{r}-\mathbf{b}_{ij})^2}\mathrm{d}\mathbf{r}.$$

It is easy to verify that

$$\Omega_{ij}^{ss} = \Omega_{ij\,x}^{ss}\Omega_{ij\,y}^{ss}\Omega_{i,j\,z}^{ss} = \mathcal{N}_i^s\mathcal{N}_j^s\mathbb{K}_{ij}\frac{\pi^{3/2}}{\gamma_{ij}^{3/2}}. \tag{C.13}$$

C.2.2 Three-center overlap integrals

Differentiating the unnormalized 3D Cartesian Gaussian functions in Eq. (3.3) with respect to x_i:

$$\begin{aligned}\frac{\partial\mathcal{G}_i^{\boldsymbol{m}_i}(\mathbf{r},\mathbf{r}_i,\alpha_i)}{\partial x_i} &= -m_{ix}(x-x_i)^{m_{ix}-1}(y-y_i)^{m_{iy}}(z-z_i)^{m_{iz}}e^{-\alpha_i(\mathbf{r}-\mathbf{r}_i)^2}\\ &\quad + 2\alpha_i(x-x_i)^{m_{ix}+1}(y-y_i)^{m_{iy}}(z-z_i)^{m_{iz}}e^{-\alpha_i(\mathbf{r}-\mathbf{r}_i)^2}\end{aligned}, \tag{C.14}$$

the following differential relation between different type of GTOs can be verified in different directions, $o = x, y, z$,

$$\frac{\partial\mathcal{G}_i^{\boldsymbol{m}_i}(\mathbf{r},\mathbf{r}_i,\alpha_i)}{\partial o_i} = 2\alpha_i\mathcal{G}_i^{\boldsymbol{m}_i+1_o}(\mathbf{r},\mathbf{r}_i,\alpha_i) - m_{io}\mathcal{G}_i^{\boldsymbol{m}_i-1_o}(\mathbf{r},\mathbf{r}_i,\alpha_i). \tag{C.15}$$

Our desired matrix elements have generally the same form as the following three-center overlap over three different Gaussians

$$\left\langle\mathcal{G}_i^{\boldsymbol{m}_i}\middle|\mathcal{G}_k^{\boldsymbol{m}_k}\middle|\mathcal{G}_j^{\boldsymbol{m}_j}\right\rangle = \int\mathcal{G}_i^{\boldsymbol{m}_i*}(\mathbf{r},\mathbf{r}_i,\alpha_i)\mathcal{G}_k^{\boldsymbol{m}_k}(\mathbf{r},\mathbf{r}_k,\alpha_k)\mathcal{G}_j^{\boldsymbol{m}_j}(\mathbf{r},\mathbf{r}_j,\alpha_j)\mathrm{d}\mathbf{r}. \tag{C.16}$$

Employing the Gaussian product rule from Eq. (3.2), the product of the three Gaussian becomes ultimately a single Gaussian with the following parameters [82]

$$\begin{aligned}\gamma_{ijk} &= \gamma_{ij} + \alpha_k = \alpha_i^* + \alpha_j + \alpha_k\\ \alpha_{ijk} &= \alpha_{ij}\alpha_k\\ \beta_{ijk} &= \frac{\gamma_{ij}\alpha_k}{\gamma_{ijk}}\\ \mathbf{b}_{ijk} &= \frac{\gamma_{ij}\mathbf{b}_{ij} + \alpha_k\mathbf{r}_k}{\gamma_{ijk}} = \frac{\alpha_i^*\mathbf{r}_i^* + \alpha_j\mathbf{r}_j + \alpha_k\mathbf{r}_k}{\gamma_{ijk}}\\ c_{ijk} &= \frac{\alpha_i^*\mathbf{r}_i^{*2} + \alpha_j\mathbf{r}_j^2 + \alpha_k\mathbf{r}_k^2}{\gamma_{ijk}}\\ \mathbb{K}_{ijk} &= \mathbb{K}_{ij}e^{-\beta_{ijk}(\mathbf{b}_{ij}-\mathbf{r}_k)^2} = e^{\gamma_{ijk}\left(\mathbf{b}_{ijk}^2 - c_{ijk}\right)},\end{aligned} \tag{C.17}$$

where α_{ij}, β_{ij}, and $\mathbb{K}_{ij}$ have already been defined in Eq. (C.10).

The three-center overlap integral, Eq. (C.16), can be factorized as in [82]

$$\left\langle\mathcal{G}_i^{\boldsymbol{m}_i}\middle|\mathcal{G}_k^{\boldsymbol{m}_k}\middle|\mathcal{G}_j^{\boldsymbol{m}_j}\right\rangle = \mathbb{K}_{ijk}I_x(m_{i_x},m_{j_x},m_{k_x})I_y\big(m_{i_y},m_{j_y},m_{k_y}\big)I_z(m_{i_z},m_{j_z},m_{k_z}), \tag{C.18}$$

$$I_o(m_{i_o}, m_{j_o}, m_{k_o}) = \frac{\pi^{1/2}}{\gamma_{ijk}^{1/2}} \sum_{l_{i_o}=0}^{m_{i_o}} \sum_{l_{j_o}=0}^{m_{j_o}} \sum_{\substack{l_{k_o}=0 \\ l_o=even}}^{m_{k_o}} \binom{m_{i_o}}{l_{i_o}} \binom{m_{j_o}}{l_{j_o}} \binom{m_{k_o}}{l_{k_o}} \times$$
$$(\mathbf{b}_{ijk_o} - o_i)^{m_{i_o}-l_{i_o}} (\mathbf{b}_{ijk_o} - o_j)^{m_{j_o}-l_{j_o}} (\mathbf{b}_{ijk_o} - o_k)^{m_{k_o}-l_{k_o}} \frac{(l_o-1)!!}{(2\gamma_{ijk})^{l_o}},$$

where $o = x, y, z$ denotes the Cartesian directions, and $l_o = l_{i_o} + l_{j_o} + l_{k_o}$.

For s-type GTOs, the three-center overlap integral reads

$$\left\langle \mathcal{G}_i^s \middle| \mathcal{G}_k^s \middle| \mathcal{G}_j^s \right\rangle = \mathbb{K}_{ijk} \frac{\pi^{3/2}}{\gamma_{ijk}^{3/2}} = \frac{\gamma_{ij}^{3/2}}{\gamma_{ijk}^{3/2}} \left\langle \mathcal{G}_i^s \middle| \mathcal{G}_j^s \right\rangle e^{-\beta_{ijk}(\mathbf{b}_{ij}-\mathbf{r}_k)^2}. \tag{C.19}$$

The two-center overlap integral $\left\langle \mathcal{G}_i^s \middle| \mathcal{G}_j^s \right\rangle = \Omega_{ij}^{ss}$ which has already been obtained in Eq. (C.13), can be also calculated by putting $\mathcal{G}_k^{\boldsymbol{m}_k} = 1$ ($\alpha_k = 0$) in the three-center overlap integral, Eq. (C.18).

To compute $\left\langle \mathcal{G}_i^{\boldsymbol{m}_i+1_o} \middle| \mathcal{G}_k^{\boldsymbol{m}_k} \middle| \mathcal{G}_j^{\boldsymbol{m}_j} \right\rangle$, with the help Eq. (C.14), it is straightforward to obtain the Obara-Saika recurrence relation [82]

$$\left\langle \mathcal{G}_i^{\boldsymbol{m}_i+1_o} \middle| \mathcal{G}_k^{\boldsymbol{m}_k} \middle| \mathcal{G}_j^{\boldsymbol{m}_j} \right\rangle = (\mathbf{b}_{ijk_o} - o_i^*) \left\langle \mathcal{G}_i^{\boldsymbol{m}_i} \middle| \mathcal{G}_k^{\boldsymbol{m}_k} \middle| \mathcal{G}_j^{\boldsymbol{m}_j} \right\rangle + \frac{1}{2\gamma_{ijk}} \Big(m_{i_o} \left\langle \mathcal{G}_i^{\boldsymbol{m}_i-1_o} \middle| \mathcal{G}_k^{\boldsymbol{m}_k} \middle| \mathcal{G}_j^{\boldsymbol{m}_j} \right\rangle$$
$$+ m_{k_o} \left\langle \mathcal{G}_i^{\boldsymbol{m}_i} \middle| \mathcal{G}_k^{\boldsymbol{m}_k-1_o} \middle| \mathcal{G}_j^{\boldsymbol{m}_j} \right\rangle + m_{j_o} \left\langle \mathcal{G}_i^{\boldsymbol{m}_i} \middle| \mathcal{G}_k^{\boldsymbol{m}_k} \middle| \mathcal{G}_j^{\boldsymbol{m}_j-1_o} \right\rangle \Big). \tag{C.20}$$

Similarly, the recurrence formula for $\left\langle \mathcal{G}_i^{\boldsymbol{m}_i} \middle| \mathcal{G}_k^{\boldsymbol{m}_k} \middle| \mathcal{G}_j^{\boldsymbol{m}_j+1_o} \right\rangle$ is

$$\left\langle \mathcal{G}_i^{\boldsymbol{m}_i} \middle| \mathcal{G}_k^{\boldsymbol{m}_k} \middle| \mathcal{G}_j^{\boldsymbol{m}_j+1_o} \right\rangle = (\mathbf{b}_{ijk_o} - o_j) \left\langle \mathcal{G}_i^{\boldsymbol{m}_i} \middle| \mathcal{G}_k^{\boldsymbol{m}_k} \middle| \mathcal{G}_j^{\boldsymbol{m}_j} \right\rangle + \frac{1}{2\gamma_{ijk}} \Big(m_{i_o} \left\langle \mathcal{G}_i^{\boldsymbol{m}_i-1_o} \middle| \mathcal{G}_k^{\boldsymbol{m}_k} \middle| \mathcal{G}_j^{\boldsymbol{m}_j} \right\rangle$$
$$+ m_{k_o} \left\langle \mathcal{G}_i^{\boldsymbol{m}_i} \middle| \mathcal{G}_k^{\boldsymbol{m}_k-1_o} \middle| \mathcal{G}_j^{\boldsymbol{m}_j} \right\rangle + m_{j_o} \left\langle \mathcal{G}_i^{\boldsymbol{m}_i} \middle| \mathcal{G}_k^{\boldsymbol{m}_k} \middle| \mathcal{G}_j^{\boldsymbol{m}_j-1_o} \right\rangle \Big). \tag{C.21}$$

C.2.3 The Obara-Saika recurrence formula for two-center overlap integrals

By considering $\mathcal{G}_k^{\boldsymbol{m}_k} = 1$ ($\alpha_k = 0$) in the recurrence formula for three-center overlap integrals, Eq. (C.20), we get the following recurrence relations for two-center overlap integrals

$$\Omega_{ij}^{\boldsymbol{m}_i+1_o\boldsymbol{m}_j} = (\mathbf{b}_{ij_o} - o_i^*)\Omega_{ij}^{\boldsymbol{m}_i\boldsymbol{m}_j} + \frac{1}{2\gamma_{ij}} \Big(m_{i_o} \Omega_{ij}^{\boldsymbol{m}_i-1_o\boldsymbol{m}_j} + m_{j_o} \Omega_{ij}^{\boldsymbol{m}_i\boldsymbol{m}_j-1_o} \Big), \tag{C.22a}$$

$$\Omega_{ij}^{\boldsymbol{m}_i\boldsymbol{m}_j+1_o} = (\mathbf{b}_{ij_o} - o_j)\Omega_{ij}^{\boldsymbol{m}_i\boldsymbol{m}_j} + \frac{1}{2\gamma_{ij}} \Big(m_{i_o} \Omega_{ij}^{\boldsymbol{m}_i-1_o\boldsymbol{m}_j} + m_{j_o} \Omega_{ij}^{\boldsymbol{m}_i\boldsymbol{m}_j-1_o} \Big), \tag{C.22b}$$

$$\Omega_{ij}^{\boldsymbol{m}_i\boldsymbol{m}_j+1_o} = \Omega_{ij}^{\boldsymbol{m}_i+1_o\boldsymbol{m}_j} + (o_i^* - o_j)\Omega_{ij}^{\boldsymbol{m}_i\boldsymbol{m}_j}. \tag{C.22c}$$

***Over s-type and p-type GTOs*:** initiating the recursive procedure from Eq. (C.13), and utilizing Eq. (C.22b), it is easy to obtain the overlap between the i^{th} s-type and the j^{th} p-type 3D GTOs in different directions, $\Omega_{ij}^{sp_o}$,

$$\Omega_{ij}^{sp_o} = \big(\mathbf{b}_{ij_o} - o_j\big)\Omega_{ij}^{ss}, \tag{C.23}$$

or inversely, employing Eq. (C.22a), to get the overlap between the i^{th} p-type and the j^{th} s-type 3D GTOs in different directions, $\Omega_{ij}^{p_o s}$,

$$\Omega_{ij}^{p_o s} = \big(\mathbf{b}_{ij_o} - o_i^*\big)\Omega_{ij}^{ss}. \tag{C.24}$$

***Over s-type and d-type GTOs*:** using Eq. (C.23) and employing Eq. (C.22b), the overlap between the i^{th} s-type and j^{th} d-type 3D GTOs (Eq. (3.6)) is obtained as $\Omega_{ij}^{sd} = \sum_{o=x,y,z} \Omega_{ij}^{sd_o}$, where

$$\Omega_{ij}^{sd_o} = \big(\mathbf{b}_{ij_o} - o_j\big)\Omega_{ij}^{sp_o} + \frac{\Omega_{ij}^{ss}}{2\gamma_{ij}}. \tag{C.25}$$

Inversely, from Eqs. (C.24), and (C.22a), the overlap between the i^{th} d-type and the j^{th} s-type 3D GTOs, Ω_{ij}^{ds}, is achieved as $\Omega_{ij}^{ds} = \sum_{o=x,y,z} \Omega_{ij}^{d_o s}$, where

$$\Omega_{ij}^{ds} = \big(\mathbf{b}_{ij_o} - o_i^*\big)\Omega_{ij}^{p_o s} + \frac{\Omega_{ij}^{ss}}{2\gamma_{ij}}. \tag{C.26}$$

***Over p-type GTOs*:** to get the overlap between the i^{th} p-type and the j^{th} p-type 3D GTOs in different directions, using Eqs. (C.23), and (C.22a), we get

$$\Omega_{ij}^{p_o p_{o'}} = \begin{cases} \big(\mathbf{b}_{ij_o} - o_i^*\big)\Omega_{ij}^{sp_{o'}} + \frac{\Omega_{ij}^{ss}}{2\gamma_{ij}} & o = o' \in \{x,y,z\} \\ \big(\mathbf{b}_{ij_o} - o_i^*\big)\Omega_{ij}^{sp_{o'}} & o \neq o' \in \{x,y,z\} \end{cases}. \tag{C.27}$$

***Over p-type and d-type GTOs*:** to evaluate the overlap between the i^{th} p-type and the j^{th} d-type 3D GTOs in different directions, employing Eqs. (C.27) , and (C.22b), we get $\Omega_{ij}^{p_o d} = \sum_{o'=x,y,z} \Omega_{ij}^{p_o d_{o'}}$, where

$$\Omega_{ij}^{p_o d_{o'}} = \begin{cases} \big(\mathbf{b}_{ij_{o'}} - o'_j\big)\Omega_{ij}^{p_o p_{o'}} + \frac{1}{2\gamma_{ij}}\big(\Omega_{ij}^{sp_{o'}} + \Omega_{ij}^{p_o s}\big) & o = o' \in \{x,y,z\} \\ \big(\mathbf{b}_{ij_{o'}} - o'_j\big)\Omega_{ij}^{p_o p_{o'}} + \frac{1}{2\gamma_{ij}}\Omega_{ij}^{p_o s} & o \neq o' \in \{x,y,z\} \end{cases}. \tag{C.28}$$

***Over d-type GTOs*:** in order to compute the overlap between the i^{th} d-type and the j^{th} d-type 3D GTOs, from Eqs. (C.28), and (C.22a) we obtain $\Omega_{ij}^{dd} = \sum_{o,o'=x,y,z} \Omega_{ij}^{d_o d_{o'}}$, where

$$\Omega_{ij}^{d_o d_{o'}} = \begin{cases} \big(\mathbf{b}_{ij_o} - o_i^*\big)\Omega_{ij}^{p_o d_{o'}} + \frac{1}{2\gamma_{ij}}\Big(\Omega_{ij}^{s d_{o'}} + 2\Omega_{ij}^{p_o p_{o'}}\Big) & o = o' \in \{x,y,z\} \\ \big(\mathbf{b}_{ij_o} - o_i^*\big)\Omega_{ij}^{p_o d_{o'}} + \frac{1}{2\gamma_{ij}}\Omega_{ij}^{s d_{o'}} & o \neq o' \in \{x,y,z\} \end{cases}. \tag{C.29}$$

C.2.4 The kinetic energy matrix elements over 3D s-type GTOs

To compute the kinetic energy matrix element over the i^{th} and the j^{th} s-type GTOs, with the help of the Gaussian product rule from Eq. (3.2), one gets

$$\mathrm{T}_{ij}^{ss} = \mathcal{N}_i^s \mathcal{N}_j^s \int e^{-\alpha_i^* \left(\mathbf{r}-\mathbf{r}_i^*\right)^2} \frac{-1}{2} \boldsymbol{\nabla}^2 e^{-\alpha_j (\mathbf{r}-\mathbf{r}_j)^2} \mathrm{d}\mathbf{r},$$

$$\Rightarrow \mathrm{T}_{ij}^{ss} = \frac{-1}{2} \mathcal{N}_i^s \mathcal{N}_j^s \mathbb{K}_{ij} \times$$

$$\Bigg[\int_{-\infty}^{\infty} \big(-2\alpha_j + 4\alpha_j^2 (x - x_j)^2\big) e^{-\gamma_{ij}\left(x-\mathbf{b}_{ij_x}\right)^2} \mathrm{d}x \int_{-\infty}^{\infty} e^{-\gamma_{ij}\left(y-\mathbf{b}_{ij_y}\right)^2} \mathrm{d}y \int_{-\infty}^{\infty} e^{-\gamma_{ij}\left(z-\mathbf{b}_{ij_z}\right)^2} \mathrm{d}z$$

$$+ \int_{-\infty}^{\infty} e^{-\gamma_{ij}\left(x-\mathbf{b}_{ij_x}\right)^2} \mathrm{d}x \int_{-\infty}^{\infty} \big(-2\alpha_j + 4\alpha_j^2 (y - y_j)^2\big) e^{-\gamma_{ij}\left(y-\mathbf{b}_{ij_y}\right)^2} \mathrm{d}y \int_{-\infty}^{\infty} e^{-\gamma_{ij}\left(z-\mathbf{b}_{ij_z}\right)^2} \mathrm{d}z$$

$$+ \int_{-\infty}^{\infty} e^{-\gamma_{ij}\left(x-\mathbf{b}_{ij_x}\right)^2} \mathrm{d}x \int_{-\infty}^{\infty} e^{-\gamma_{ij}\left(y-\mathbf{b}_{ij_y}\right)^2} \mathrm{d}y \int_{-\infty}^{\infty} \big(-2\alpha_j + 4\alpha_j^2 (z - z_j)^2\big) e^{-\gamma_{ij}\left(z-\mathbf{b}_{ij_z}\right)^2} \mathrm{d}z \Bigg],$$

which is nothing but

$$\mathrm{T}_{ij}^{ss} = \mathrm{T}_{ij\,x}^{ss} \Omega_{ij\,y}^{ss} \Omega_{i,j\,z}^{ss} + \Omega_{ij\,x}^{ss} \mathrm{T}_{ij\,y}^{ss} \Omega_{i,j\,z}^{ss} + \Omega_{ij\,x}^{ss} \Omega_{ij\,y}^{ss} \mathrm{T}_{ij\,z}^{ss}. \tag{C.30}$$

Using Eq. (C.9), it is straightforward to finally obtain

$$\mathrm{T}_{ij}^{ss} = \big(3\beta_{ij} - 2\alpha_j^2 (\mathbf{b}_{ij} - \mathbf{r}_j)^2\big)\Omega_{ij}^{ss} = \beta_{ij}\big(3 - 2\beta_{ij}(\mathbf{r}_i^* - \mathbf{r}_j)^2\big)\Omega_{ij}^{ss}. \tag{C.31}$$

C.2.5 The Obara-Saika recurrence formula for the kinetic energy

Employing Eq. (C.14), and the identity of $\int \mathrm{d}\mathbf{r}\ \mathcal{G}_i^{\boldsymbol{m}_i} \boldsymbol{\nabla}^2 \mathcal{G}_j^{\boldsymbol{m}_j} = -\int \mathrm{d}\mathbf{r} (\boldsymbol{\nabla}\mathcal{G}_i^{\boldsymbol{m}_i}) \cdot \big(\boldsymbol{\nabla}\mathcal{G}_j^{\boldsymbol{m}_j}\big)$, the kinetic energy integral in Eq. (C.12) reduces to a linear combination of the two-center integrals. Then, we obtain the following recurrence relations for kinetic energy integrals

$$\mathrm{T}_{ij}^{\boldsymbol{m}_i + 1_o \boldsymbol{m}_j} = \big(\mathbf{b}_{ij_o} - o_i^*\big)\mathrm{T}_{ij}^{\boldsymbol{m}_i \boldsymbol{m}_j} + \frac{1}{2\gamma_{ij}}\Big(m_{i_o} \mathrm{T}_{ij}^{\boldsymbol{m}_i - 1_o \boldsymbol{m}_j} + m_{j_o} \mathrm{T}_{ij}^{\boldsymbol{m}_i \boldsymbol{m}_j - 1_o}\Big) \tag{C.32a}$$
$$+ 2\beta_{ij}\Big(\Omega_{ij}^{\boldsymbol{m}_i + 1_o \boldsymbol{m}_j} - \frac{m_{i_o}}{2\alpha_i^*} \Omega_{ij}^{\boldsymbol{m}_i - 1_o \boldsymbol{m}_j}\Big),$$

$$\mathrm{T}_{ij}^{\boldsymbol{m}_i\boldsymbol{m}_j+1_o} = \big(\mathbf{b}_{ij_o} - o_j\big)\mathrm{T}_{ij}^{\boldsymbol{m}_i\boldsymbol{m}_j} + \frac{1}{2\gamma_{ij}}\Big(m_{i_o}\mathrm{T}_{ij}^{\boldsymbol{m}_i-1_o\boldsymbol{m}_j} + m_{j_o}\mathrm{T}_{ij}^{\boldsymbol{m}_i\boldsymbol{m}_j-1_o}\Big) + 2\beta_{ij}\Big(\Omega_{ij}^{\boldsymbol{m}_i\boldsymbol{m}_j+1_o} - \frac{m_{j_o}}{2\alpha_j}\Omega_{ij}^{\boldsymbol{m}_i\boldsymbol{m}_j-1_o}\Big). \tag{C.32b}$$

***Over s-type and p-type GTOs*:** initiating the recursive procedure from Eq. (C.31), and utilizing Eq. (C.32b), it is easy to obtain the matrix element of the kinetic energy over the i^{th} s-type and the j^{th} p-type 3D GTOs in different directions, $\mathrm{T}_{ij}^{sp_o}$,

$$\mathrm{T}_{ij}^{sp_o} = \big(\mathbf{b}_{ij_o} - o_j\big)\mathrm{T}_{ij}^{ss} + 2\beta_{ij}\Omega_{ij}^{sp_o}, \tag{C.33}$$

or inversely, employing Eq. (C.32a), to get the matrix element of the kinetic energy over the i^{th} p-type and the j^{th} s-type 3D GTOs in different directions, $\mathrm{T}_{ij}^{p_os}$,

$$\mathrm{T}_{ij}^{p_os} = \big(\mathbf{b}_{ij_o} - o_i^*\big)\mathrm{T}_{ij}^{ss} + 2\beta_{ij}\Omega_{ij}^{p_os}. \tag{C.34}$$

***Over s-type and d-type GTOs*:** using Eqs. (C.33), and (C.32b), the matrix element of the kinetic energy over the i^{th} s-type and j^{th} d-type 3D GTOs (Eq. (3.6)) is obtained as $\mathrm{T}_{ij}^{sd} = \sum_{o=x,y,z}\mathrm{T}_{ij}^{sd_o}$, where

$$\mathrm{T}_{ij}^{sd_o} = \big(\mathbf{b}_{ij_o} - o_j\big)\mathrm{T}_{ij}^{sp_o} + \frac{\mathrm{T}_{ij}^{ss}}{2\gamma_{ij}} + 2\beta_{ij}\Big(\Omega_{ij}^{sd_o} - \frac{\Omega_{ij}^{ss}}{2\alpha_j}\Big). \tag{C.35}$$

Inversely, from Eqs. (C.34), and (C.32a), the matrix element of the kinetic energy over the i^{th} d-type and the j^{th} s-type 3D GTOs, is achieved as $\mathrm{T}_{ij}^{ds} = \sum_{o=x,y,z}\mathrm{T}_{ij}^{d_os}$, where

$$\mathrm{T}_{ij}^{d_os} = \big(\mathbf{b}_{ij_o} - o_i^*\big)\mathrm{T}_{ij}^{p_os} + \frac{\mathrm{T}_{ij}^{ss}}{2\gamma_{ij}} + 2\beta_{ij}\Big(\Omega_{ij}^{d_os} - \frac{\Omega_{ij}^{ss}}{2\alpha_i^*}\Big). \tag{C.36}$$

***Over p-type GTOs*:** to calculate the matrix element of the kinetic energy over the i^{th} p-type and the j^{th} p-type 3D GTOs in different directions, employing Eqs. (C.33), and (C.32a), we get

$$\mathrm{T}_{ij}^{p_op_{o'}} = \begin{cases} \big(\mathbf{b}_{ij_o} - o_i^*\big)\mathrm{T}_{ij}^{sp_{o'}} + \frac{\mathrm{T}_{ij}^{ss}}{2\gamma_{ij}} + 2\beta_{ij}\Omega_{ij}^{p_op_{o'}} & o = o' \in \{x,y,z\} \\ \big(\mathbf{b}_{ij_o} - o_i^*\big)\mathrm{T}_{ij}^{sp_{o'}} + 2\beta_{ij}\Omega_{ij}^{p_op_{o'}} & o \neq o' \in \{x,y,z\} \end{cases}. \tag{C.37}$$

***Over p-type and d-type GTOs*:** to get the matrix element of the kinetic energy over the i^{th} p-type and the j^{th} d-type 3D GTOs in different directions, from Eqs. (C.35), and (C.32a),

we arrive at $\mathrm{T}_{ij}^{p_o d} = \sum_{o'=x,y,z} \mathrm{T}_{ij}^{p_o d_{o'}}$, where

$$\mathrm{T}_{ij}^{p_o d_{o'}} = \begin{cases} \left(\mathbf{b}_{ij_o} - o_i^*\right)\mathrm{T}_{ij}^{s d o'} + \frac{\mathrm{T}_{ij}^{s p_{o'}}}{\gamma_{ij}} + 2\beta_{ij}\Omega_{ij}^{p_o d_{o'}} & o = o' \in \{x,y,z\} \\ \left(\mathbf{b}_{ij_o} - o_i^*\right)\mathrm{T}_{ij}^{s d o'} + 2\beta_{ij}\Omega_{ij}^{p_o d_{o'}} & o \neq o' \in \{x,y,z\} \end{cases}. \tag{C.38}$$

***Over d-type GTOs*:** in order to compute the matrix element of the kinetic energy over the i^{th} d-type and the j^{th} d-type 3D GTOs, using Eqs. (C.38), and (C.32a), we obtain $\mathrm{T}_{ij}^{dd} = \sum_{o,o'=x,y,z} \mathrm{T}_{ij}^{d_o d_{o'}}$, where

$$\mathrm{T}_{ij}^{d_o d_{o'}} = \begin{cases} \left(\mathbf{b}_{ij_o} - o_i^*\right)\mathrm{T}_{ij}^{p_o d_{o'}} + \frac{\mathrm{T}_{ij}^{s d_{o'}} + 2\mathrm{T}_{ij}^{p_o p_{o'}}}{2\gamma_{ij}} + 2\beta_{ij}\left(\Omega_{ij}^{d_o d_{o'}} - \frac{\Omega_{ij}^{s d_{o'}}}{2\alpha_i^*}\right) & o = o' \in \{x,y,z\} \\ \left(\mathbf{b}_{ij_o} - o_i^*\right)\mathrm{T}_{ij}^{p_o d_{o'}} + \frac{\mathrm{T}_{ij}^{s d_{o'}}}{2\gamma_{ij}} + 2\beta_{ij}\left(\Omega_{ij}^{d_o d_{o'}} - \frac{\Omega_{ij}^{s d_{o'}}}{2\alpha_i^*}\right) & o \neq o' \in \{x,y,z\} \end{cases}. \tag{C.39}$$

C.2.6 The Coulombic potential matrix elements over 3D s-type GTOs

For the matrix element of a single-center nuclear attraction potential of the form $\frac{-1}{|\mathbf{r}-\mathbf{R}|}$, over the i^{th} and the j^{th} s-type GTOs, one can write

$$\mathrm{V}_{ij}^{ss} = \mathcal{N}_i^s \mathcal{N}_j^s \int e^{-\alpha_i^*\left(\mathbf{r}-\mathbf{r}_i^*\right)^2} \frac{-1}{|\mathbf{r}-\mathbf{R}|} e^{-\alpha_j(\mathbf{r}-\mathbf{r}_j)^2} \mathrm{d}\mathbf{r}. \tag{C.40}$$

Since, the central term $\frac{1}{|\mathbf{r}-\mathbf{R}|}$ can be written as an integral of a s-type GTO

$$\frac{1}{|\mathbf{r}-\mathbf{R}|} = \frac{2}{\sqrt{\pi}} \int_0^\infty e^{-t^2(\mathbf{r}-\mathbf{R})^2} \mathrm{d}t, \tag{C.41}$$

Eq. (C.40), can be considered as an integral of a three-center overlap integral, Eq. (C.19), with $\alpha_k = t^2$ and $\mathbf{r}_k = \mathbf{R}$. Then, we directly get

$$\Rightarrow \mathrm{V}_{ij}^{ss} = \frac{-2}{\sqrt{\pi}} \gamma_{ij}^{3/2} \Omega_{ij}^{ss} \int_0^\infty \frac{e^{-\frac{\gamma_{ij} t^2}{\gamma_{ij}+t^2}\boldsymbol{\rho}^2}}{\left(\gamma_{ij}+t^2\right)^{3/2}} \mathrm{d}t,$$

where $\boldsymbol{\rho} = \mathbf{b}_{ij} - \mathbf{R}$. This integral can be easily solved changing the variable

$$\frac{t^2}{\gamma_{ij}+t^2} = u^2 \Rightarrow 1 + \gamma_{ij} t^{-2} = u^{-2} \Rightarrow \gamma_{ij} t^{-3} \mathrm{d}t = u^{-3} \mathrm{d}u \Rightarrow \mathrm{d}t = \frac{1}{\gamma_{ij}} \left(\frac{t}{u}\right)^3 \mathrm{d}u. \tag{C.42}$$

Hence, we ultimately obtain

$$\mathrm{V}_{ij}^{ss} = -2\sqrt{\frac{\gamma_{ij}}{\pi}}\Omega_{ij}^{ss}F_0\big(\gamma_{ij}\boldsymbol{\rho}^2\big), \tag{C.43}$$

where

$$F_0\big(\gamma_{ij}\boldsymbol{\rho}^2\big) = \int_0^1 e^{-\gamma_{ij}\boldsymbol{\rho}^2u^2}\mathrm{d}u = \sqrt{\frac{\pi}{4\gamma_{ij}\boldsymbol{\rho}^2}}\,\mathrm{erf}(\sqrt{\gamma_{ij}\boldsymbol{\rho}^2}), \tag{C.44}$$

is the zeroth order Boys function, Eq. (B.15). Substituting Eq. (C.13) in Eq. (C.43), we reach

$$\mathrm{V}_{ij}^{ss} = \frac{-2\pi}{\gamma_{ij}}\mathcal{N}_i^s\mathcal{N}_j^s\mathbb{K}_{ij}F_0\big(\gamma_{ij}\boldsymbol{\rho}^2\big). \tag{C.45}$$

C.2.7 The Obara-Saika recurrence formula for Coulombic potentials

As we already saw in Eq. (C.40), the matrix elements of single-center Coulombic potentials can be written as an integral of three-center overlap integrals

$$\mathrm{V}_{ij}^{\boldsymbol{m}_i\boldsymbol{m}_j} = \frac{2}{\sqrt{\pi}}\int_0^\infty \mathbb{V}_{ij}^{\boldsymbol{m}_i\boldsymbol{m}_j}(t)\mathrm{d}t, \tag{C.46}$$

where

$$\mathbb{V}_{ij}^{\boldsymbol{m}_i\boldsymbol{m}_j}(t) = \int \mathcal{G}_i^{\boldsymbol{m}_i^*}(\mathbf{r},\mathbf{r}_i,\alpha_i)\mathcal{G}_k^s(\mathbf{r},\mathbf{R},t^2)\mathcal{G}_j^{\boldsymbol{m}_j}(\mathbf{r},\mathbf{r}_j,\alpha_j)\mathrm{d}\mathbf{r}. \tag{C.47}$$

From the three-center overlap recurrence formula, Eq. (C.20), considering $\alpha_k = t^2$ and $\mathbf{r}_k = \mathbf{R}$, and $\boldsymbol{\rho} = \mathbf{b}_{ij} - \mathbf{R}$, it is straightforward to obtain the following recurrence formula for $\mathbb{V}_{ij}^{\boldsymbol{m}_i+1_o\boldsymbol{m}_j}(t)$

$$\begin{aligned}\mathbb{V}_{ij}^{\boldsymbol{m}_i+1_o\boldsymbol{m}_j}(t) = &\big(\mathbf{b}_{ij_o} - o_i^*\big)\mathbb{V}_{ij}^{\boldsymbol{m}_i\boldsymbol{m}_j}(t) - \boldsymbol{\rho}_o\left(\frac{t^2}{\gamma_{ij}+t^2}\right)\mathbb{V}_{ij}^{\boldsymbol{m}_i\boldsymbol{m}_j}(t)\\ &+\frac{1}{2\gamma_{ij}}\left(1-\frac{t^2}{\gamma_{ij}+t^2}\right)\Big(\boldsymbol{m}_{i_o}\mathbb{V}_{ij}^{\boldsymbol{m}_i-1_o\boldsymbol{m}_j}(t) + \boldsymbol{m}_{j_o}\mathbb{V}_{ij}^{\boldsymbol{m}_i\boldsymbol{m}_j-1_o}(t)\Big)\end{aligned}, \tag{C.48}$$

and inversely for $\mathbb{V}_{ij}^{\boldsymbol{m}_i\boldsymbol{m}_j+1_o}(t)$

$$\begin{aligned}\mathbb{V}_{ij}^{\boldsymbol{m}_i\boldsymbol{m}_j+1_o}(t) = &\big(\mathbf{b}_{ij_o} - o_j\big)\mathbb{V}_{ij}^{\boldsymbol{m}_i\boldsymbol{m}_j}(t) - \boldsymbol{\rho}_o\left(\frac{t^2}{\gamma_{ij}+t^2}\right)\mathbb{V}_{ij}^{\boldsymbol{m}_i\boldsymbol{m}_j}(t)\\ &+\frac{1}{2\gamma_{ij}}\left(1-\frac{t^2}{\gamma_{ij}+t^2}\right)\Big(\boldsymbol{m}_{i_o}\mathbb{V}_{ij}^{\boldsymbol{m}_i-1_o\boldsymbol{m}_j}(t) + \boldsymbol{m}_{j_o}\mathbb{V}_{ij}^{\boldsymbol{m}_i\boldsymbol{m}_j-1_o}(t)\Big)\end{aligned}. \tag{C.49}$$

Introducing the following auxiliary integral

$$\mathcal{V}_{ij,n}^{\boldsymbol{m}_i\boldsymbol{m}_j} = \frac{2}{\sqrt{\pi}}\int_0^\infty \left(\frac{t^2}{\gamma_{ij}+t^2}\right)^n \mathbb{V}_{ij}^{\boldsymbol{m}_i\boldsymbol{m}_j}(t)\mathrm{d}t, \tag{C.50}$$

with non-negative integer n, it satisfies the following recurrence formula

$$\begin{aligned}\mathcal{V}_{ij,n}^{\boldsymbol{m}_i+1_o\boldsymbol{m}_j} = \big(\mathbf{b}_{ij_o} - o_i^*\big)\mathcal{V}_{ij,n}^{\boldsymbol{m}_i\boldsymbol{m}_j} + \frac{1}{2\gamma_{ij}}\Big(\boldsymbol{m}_{i_o}\mathcal{V}_{ij,n}^{\boldsymbol{m}_i-1_o\boldsymbol{m}_j} + \boldsymbol{m}_{j_o}\mathcal{V}_{ij,n}^{\boldsymbol{m}_i\boldsymbol{m}_j-1_o}\Big)\\ -\boldsymbol{\rho}_o\mathcal{V}_{ij,n+1}^{\boldsymbol{m}_i\boldsymbol{m}_j} - \frac{1}{2\gamma_{ij}}\Big(\boldsymbol{m}_{i_o}\mathcal{V}_{ij,n+1}^{\boldsymbol{m}_i-1_o\boldsymbol{m}_j} + \boldsymbol{m}_{j_o}\mathcal{V}_{ij,n+1}^{\boldsymbol{m}_i\boldsymbol{m}_j-1_o}\Big)\end{aligned}, \tag{C.51}$$

and inversely

$$\begin{aligned}\mathcal{V}_{ij,n}^{\boldsymbol{m}_i\boldsymbol{m}_j+1_o} = \big(\mathbf{b}_{ij_o} - o_j\big)\mathcal{V}_{ij,n}^{\boldsymbol{m}_i\boldsymbol{m}_j} + \frac{1}{2\gamma_{ij}}\Big(\boldsymbol{m}_{i_o}\mathcal{V}_{ij,n}^{\boldsymbol{m}_i-1_o\boldsymbol{m}_j} + \boldsymbol{m}_{j_o}\mathcal{V}_{ij,n}^{\boldsymbol{m}_i\boldsymbol{m}_j-1_o}\Big)\\ -\boldsymbol{\rho}_o\mathcal{V}_{ij,n+1}^{\boldsymbol{m}_i\boldsymbol{m}_j} - \frac{1}{2\gamma_{ij}}\Big(\boldsymbol{m}_{i_o}\mathcal{V}_{ij,n+1}^{\boldsymbol{m}_i-1_o\boldsymbol{m}_j} + \boldsymbol{m}_{j_o}\mathcal{V}_{ij,n+1}^{\boldsymbol{m}_i\boldsymbol{m}_j-1_o}\Big)\end{aligned}. \tag{C.52}$$

So we can conclude

$$\mathcal{V}_{ij,n}^{\boldsymbol{m}_i+1_o\boldsymbol{m}_j} = \mathcal{V}_{ij,n}^{\boldsymbol{m}_i\boldsymbol{m}_j+1_o} - (o_i^* - o_j)\mathcal{V}_{ij,n}^{\boldsymbol{m}_i\boldsymbol{m}_j}. \tag{C.53}$$

The matrix elements of the Coulombic potential over GTOs, $\mathrm{V}_{ij}^{\boldsymbol{m}_i\boldsymbol{m}_j}$ is equal to the zeroth order of the auxiliary integrals, Eq. (C.50)

$$\mathrm{V}_{ij}^{\boldsymbol{m}_i\boldsymbol{m}_j} = \mathcal{V}_{ij,n=0}^{\boldsymbol{m}_i\boldsymbol{m}_j}. \tag{C.54}$$

The auxiliary integral introduced in Eq. (C.50), over **s-type** GTOs gives

$$\mathcal{V}_{ij,n}^{ss} = 2\sqrt{\frac{\gamma_{ij}}{\pi}}\Omega_{ij}^{ss}\int_0^1 u^{2n}e^{-\gamma_{ij}\boldsymbol{\rho}^2u^2}\mathrm{d}u = 2\sqrt{\frac{\gamma_{ij}}{\pi}}\Omega_{ij}^{ss}F_n(\gamma_{ij}\boldsymbol{\rho}^2), \tag{C.55}$$

where from Eq. (C.42), $u^2 = \frac{t^2}{\gamma_{ij}+t^2}$, and F_n is the n^{th} order Boys function.

***Over s-type and p-type GTOs*:** initiating the recursive procedure from V_{ij}^{ss}, and utilizing Eq. (C.52), it is easy to obtain the matrix element of the Coulombic potential over the i^{th} s-type and the j^{th} p-type 3D GTOs in different directions, $\mathrm{V}_{ij}^{sp_o} = \mathcal{V}_{ij,0}^{sp_o}$, where

$$\mathcal{V}_{ij,n}^{sp_o} = \big(\mathbf{b}_{ij_o} - o_j\big)\mathcal{V}_{ij,n}^{ss} - \boldsymbol{\rho}_o\mathcal{V}_{ij,n+1}^{ss}. \tag{C.56}$$

Inversely, employing Eq. (C.51), one can easily get the matrix element of the Coulombic potential over the i^{th} p-type and the j^{th} s-type 3D GTOs in different directions, $\mathrm{V}_{ij}^{p_os} = \mathcal{V}_{ij,0}^{p_os}$, where

$$\mathcal{V}_{ij,n}^{p_os} = \big(\mathbf{b}_{ij_o} - o_i^*\big)\mathcal{V}_{ij,n}^{ss} - \boldsymbol{\rho}_o\mathcal{V}_{ij,n+1}^{ss}. \tag{C.57}$$

***Over s-type and d-type GTOs*:** using Eqs. (C.56), and (C.52), the matrix element of the Coulombic potential over the i^{th} s-type and j^{th} d-type 3D GTOs (Eq. (3.6)) is obtained as

$\mathrm{V}_{ij}^{sd} = \sum_{o=x,y,z} \mathcal{V}_{ij,0}^{sd_0}$, where

$$\mathcal{V}_{ij,n}^{sd_0} = \big(\mathbf{b}_{ij_o} - o_j\big)\mathcal{V}_{ij,n}^{sp_o} - \boldsymbol{\rho}_o \mathcal{V}_{ij,n+1}^{sp_o} + \frac{1}{2\gamma_{ij}}\big(\mathcal{V}_{ij,n}^{ss} - \mathcal{V}_{ij,n+1}^{ss}\big). \tag{C.58}$$

Inversely, from Eqs. (C.57), and (C.51), the matrix element of the Coulombic potential over the i^{th} d-type and the j^{th} s-type 3D GTOs, reads $\mathrm{V}_{ij}^{ds} = \sum_{o=x,y,z} \mathcal{V}_{ij,0}^{d_0 s}$, where

$$\mathcal{V}_{ij,n}^{d_0 s} = \big(\mathbf{b}_{ij_o} - o_i^*\big)\mathcal{V}_{ij,n}^{p_o s} - \boldsymbol{\rho}_o \mathcal{V}_{ij,n+1}^{p_o s} + \frac{1}{2\gamma_{ij}}\big(\mathcal{V}_{ij,n}^{ss} - \mathcal{V}_{ij,n+1}^{ss}\big). \tag{C.59}$$

***Over p-type GTOs*:** to calculate the matrix element of the Coulombic potential over the i^{th} p-type and the j^{th} p-type 3D GTOs in different directions, employing Eqs. (C.56), and (C.51), we get $\mathrm{V}_{ij}^{p_o p_{o'}} = \mathcal{V}_{ij,0}^{p_o p_{o'}}$, where

$$\mathcal{V}_{ij,n}^{p_o p_{o'}} = \begin{cases} \big(\mathbf{b}_{ij_o} - o_i^*\big)\mathcal{V}_{ij,n}^{sp_{o'}} - \boldsymbol{\rho}_o \mathcal{V}_{ij,n+1}^{sp_{o'}} + \frac{1}{2\gamma_{ij}}\big(\mathcal{V}_{ij,n}^{ss} - \mathcal{V}_{ij,n+1}^{ss}\big) & o = o' \in \{x,y,z\} \\ \big(\mathbf{b}_{ij_o} - o_i^*\big)\mathrm{V}_{ij,n}^{sp_{o'}} - \boldsymbol{\rho}_o \mathcal{V}_{ij,n+1}^{sp_{o'}} & o \neq o' \in \{x,y,z\} \end{cases}. \tag{C.60}$$

***Over p-type and d-type GTOs*:** to get the matrix element of the Coulombic potential over the i^{th} p-type and the j^{th} d-type 3D GTOs in different directions, using Eqs. (C.58), and (C.51), we obtain $\mathrm{V}_{ij}^{p_o d} = \sum_{o'=x,y,z} \mathcal{V}_{ij,0}^{p_o d_{o'}}$, where

$$\mathcal{V}_{ij,n}^{p_o d_{o'}} = \begin{cases} \big(\mathbf{b}_{ij_o} - o_i^*\big)\mathcal{V}_{ij,n}^{sd_{o'}} - \boldsymbol{\rho}_o \mathcal{V}_{ij,n+1}^{sd_{o'}} + \frac{1}{\gamma_{ij}}\big(\mathcal{V}_{ij,n}^{sp_{o'}} - \mathcal{V}_{ij,n+1}^{sp_{o'}}\big) & o = o' \in \{x,y,z\} \\ \big(\mathbf{b}_{ij_o} - o_i^*\big)\mathrm{V}_{ij,n}^{sd_{o'}} - \boldsymbol{\rho}_o \mathcal{V}_{ij,n+1}^{sd_{o'}} & o \neq o' \in \{x,y,z\} \end{cases}. \tag{C.61}$$

***Over d-type GTOs*:** for the matrix element of the Coulombic potential over the i^{th} d-type and the j^{th} d-type 3D GTOs, from Eqs. (C.61), and (C.51), we arrive at $\mathrm{V}_{ij}^{dd} = \sum_{o,o'=x,y,z} \mathcal{V}_{ij,0}^{d_o d_{o'}}$, where

$$\mathcal{V}_{ij,n}^{d_o d_{o'}} = \begin{cases} \big(\mathbf{b}_{ij_o} - o_i^*\big)\mathcal{V}_{ij,n}^{p_o d_{o'}} - \boldsymbol{\rho}_o \mathcal{V}_{ij,n+1}^{p_o d_{o'}} + \frac{1}{2\gamma_{ij}}\Big(\mathcal{V}_{ij,n}^{sd_{o'}} - \mathcal{V}_{ij,n+1}^{sd_{o'}}\Big) & \\ \qquad + \frac{1}{\gamma_{ij}}\big(\mathcal{V}_{ij,n}^{p_o p_{o'}} - \mathcal{V}_{ij,n+1}^{p_o p_{o'}}\big) & o = o' \in \{x,y,z\} \\ \big(\mathbf{b}_{ij_o} - o_i^*\big)\mathrm{V}_{ij,n}^{p_o d_{o'}} - \boldsymbol{\rho}_o \mathcal{V}_{ij,n+1}^{p_o d_{o'}} + \frac{1}{2\gamma_{ij}}\Big(\mathcal{V}_{ij,n}^{sd_{o'}} - \mathcal{V}_{ij,n+1}^{sd_{o'}}\Big) & o \neq o' \in \{x,y,z\} \end{cases}. \tag{C.62}$$

C.2.8 3D Hydrogen atom represented by a single atomic-centered GTO

We are going to get the optimized exponent of a single atomic-centered s-type GTOs representing the ground state wave function of the 3D Hydrogen atom. Using Eqs. (C.31), and (C.43), and knowing the fact that $F_0(\boldsymbol{\rho} = 0) = 1$, for a normalized s-type GTO located on the center, $\alpha_i = \alpha_j = \alpha$, and $\mathbf{r}_i = \mathbf{r}_j = 0$, one can easily obtain

$$\mathrm{H}_{11}^{ss} = \mathrm{T}_{11}^{ss} + \mathrm{V}_{11}^{ss} = \frac{3\alpha}{2} - 2\left(\frac{2\alpha}{\pi}\right)^{1/2}. \tag{C.63}$$

Employing the variational method, the optimized value for α can be found as

$$\frac{\mathrm{dH}_{11}^{ss}}{\mathrm{d}\alpha} = \frac{3}{2} - \frac{2}{\pi}\left(\frac{2\alpha}{\pi}\right)^{-1/2} = 0 \Rightarrow \alpha = \frac{8}{9\pi}. \tag{C.64}$$

References

[1] F. Krausz and M. Ivanov. "Attosecond physics". In: *Reviews of Modern Physics* 81 (2009), pp. 163–234 (cit. on p. 1).

[2] M. Chini, K. Zhao, and Z. Chang. "The generation characterization and applications of broadband isolated attosecond pulses". In: *Nature Photonics* 8 (2014), pp. 178–186 (cit. on p. 1).

[3] K. Ueda et al. "Roadmap on photonic electronic and atomic collision physics: I. Light-matter interaction". In: *Journal of Physics B: Atomic, Molecular and Optical Physics* 52 (2019), p. 171001 (cit. on p. 1).

[4] D. M. Villeneuve. "Attosecond science". In: *Contemporary Physics* 59 (2018), pp. 47–61 (cit. on p. 1).

[5] L. Cattaneo et al. "Attosecond coupled electron and nuclear dynamics in dissociative ionization of H 2". In: *Nature Physics* 14 (2018), pp. 733–739 (cit. on p. 1).

[6] C. D. Lin et al. *Attosecond and Strong-Field Physics*. Cambridge University Press, 2018 (cit. on p. 1).

[7] M. Nisoli et al. "Attosecond Electron Dynamics in Molecules". In: *Chemical Reviews* 117 (2017), pp. 10760–10825 (cit. on p. 1).

[8] M. F. Ciappina et al. "Attosecond physics at the nanoscale". In: *Reports on Progress in Physics* 80 (2017), p. 054401 (cit. on p. 1).

[9] Z. Chang, P. B. Corkum, and S. R. Leone. "Attosecond optics and technology: progress to date and future prospects [Invited]". In: *Journal of the Optical Society of America B* 33 (2016), p. 1081 (cit. on p. 1).

[10] R. Pazourek, S. Nagele, and J. Burgdörfer. "Attosecond chronoscopy of photoemission". In: *Reviews of Modern Physics* 87 (2015), pp. 765–802 (cit. on p. 1).

[11] P. M. Kraus et al. "Attosecond charge migration and its laser control". In: *Journal of Physics: Conference Series* 635 (2015), p. 112136 (cit. on p. 1).

[12] X.-Y. Miao and C.-P. Zhang. "Multichannel recombination in high-order-harmonic generation from asymmetric molecular ions". In: *Physical Review A* 89 (2014), p. 033410 (cit. on p. 1).

[13] F. Morales et al. "High harmonic spectroscopy of electron localization in the hydrogen molecular ion". In: *Journal of Physics B: Atomic, Molecular and Optical Physics* 47 (2014), p. 204015 (cit. on p. 1).

[14] A. Scrinzi. "t -SURFF: fully differential two-electron photo-emission spectra". In: *New Journal of Physics* 14 (2012), p. 085008 (cit. on p. 1).

[15] C. B. Madsen et al. "Multiphoton above threshold effects in strong-field fragmentation". In: *Physical Review Letters* 109 (2012), p. 163003 (cit. on p. 1).

[16] J. Zhao and M. Lein. "Positioning of Bound Electron Wave Packets in Molecules Revealed by High-Harmonic Spectroscopy". In: *The Journal of Physical Chemistry A* 116 (2012), pp. 2723–2727 (cit. on p. 1).

[17] S. Chelkowski, T. Bredtmann, and A. D. Bandrauk. "High-order-harmonic generation from coherent electron wave packets in atoms and molecules as a tool for monitoring attosecond electrons". In: *Physical Review A* 85 (2012), p. 033404 (cit. on p. 1).

[18] A. D. Bandrauk et al. "Effect of Nuclear Motion on Molecular High-Order Harmonics and on Generation of Attosecond Pulses in Intense Laser Pulses". In: *Physical Review Letters* 101 (2008), p. 153901 (cit. on p. 1).

[19] L. Feng, H. J. Kapteyn, and A. Y. Feng. "Generations of even-order harmonics from vibrating H2+ and T2+ in the rising and falling parts of the laser field". In: *Chemical Physics* 505 (2018), pp. 47–54 (cit. on p. 1).

[20] W. Y. Li et al. "Probing nuclear dynamics of oriented HeH+ with odd-even high-order harmonics". In: *Physical Review A* 94 (2016), p. 053407 (cit. on p. 1).

[21] K.-J. Yuan and A. D. Bandrauk. "Time-Resolved Photoelectron Imaging of Molecular Coherent Excitation and Charge Migration by Ultrashort Laser Pulses". In: *The Journal of Physical Chemistry A* 122 (2018), pp. 2241–2249 (cit. on pp. 1, 12).

[22] S. Chelkowski and A. D. Bandrauk. "Photon-momentum transfer in molecular photoionization". In: *Physical Review A* 97 (2018), p. 053401 (cit. on p. 1).

[23] N. Suárez et al. "High-order-harmonic generation in atomic and molecular systems". In: *Physical Review A* 95 (2017), p. 033415 (cit. on p. 1).

[24] A. Palacios, J. L. Sanz-Vicario, and F. Martín. "Theoretical methods for attosecond electron and nuclear dynamics: applications to the H 2 molecule". In: *Journal of Physics B: Atomic, Molecular and Optical Physics* 48 (2015), p. 242001 (cit. on p. 1).

[25] M. Y. Emelin and M. Y. Ryabikin. "Atomic photoionization and dynamical stabilization with subrelativistically intense high-frequency light: Magnetic-field effects revisited". In: *Physical Review A* 89 (2014), p. 013418 (cit. on p. 1).

[26] V. Roudnev, B. D. Esry, and I. Ben-Itzhak. "Controlling HD+ and H2+ dissociation with the carrier-envelope phase difference of an intense ultrashort laser pulse". In: *Physical Review Letters* 93 (2004), p. 163601 (cit. on p. 1).

[27] J. M. N. Djiokap et al. "Dynamical electron vortices in attosecond double photoionization of H2". In: *Physical Review A* 98 (2018), p. 063407 (cit. on p. 1).

[28] S. X. Hu, L. A. Collins, and B. I. Schneider. "Attosecond photoelectron microscopy of H2+". In: *Physical Review A - Atomic, Molecular, and Optical Physics* 80 (2009), p. 023426 (cit. on p. 1).

[29] R.-F. Lu, P.-Y. Zhang, and K.-L. Han. "Attosecond-resolution quantum dynamics calculations for atoms and molecules in strong laser fields". In: *Physical Review E* 77 (2008), p. 066701 (cit. on p. 1).

[30] T. Morishita et al. "Two-dimensional electron momentum spectra of argon ionized by short intense lasers: Comparison of theory with experiment". In: *Physical Review A - Atomic, Molecular, and Optical Physics* 75 (2007), p. 023407 (cit. on p. 1).

[31] Z. Chen et al. "Analysis of two-dimensional photoelectron momentum spectra and the effect of the long-range Coulomb potential in single ionization of atoms by intense lasers". In: *Physical Review A - Atomic, Molecular, and Optical Physics* 74 (2006), p. 053405 (cit. on p. 1).

[32] D. Bauer and P. Koval. "Qprop: A Schrödinger-solver for intense laser–atom interaction". In: *Computer Physics Communications* 174 (2006), pp. 396–421 (cit. on pp. 1, 43).

[33] Z. Zhou and S.-I. Chu. "Precision calculation of above-threshold multiphoton ionization in intense short-wavelength laser fields: The momentum-space approach and time-dependent generalized pseudospectral method". In: *Physical Review A* 83 (2011), p. 013405 (cit. on p. 1).

[34] J. L. Sanz-Vicario, H. Bachau, and F. Martín. "Time-dependent theoretical description of molecular autoionization produced by femtosecond xuv laser pulses". In: *Physical Review A* 73 (2006), p. 033410 (cit. on p. 1).

[35] O. Zatsarinny. "BSR: B-spline atomic R-matrix codes". In: *Computer Physics Communications* 174 (2006), pp. 273–356 (cit. on p. 1).

[36] C. Marante, L. Argenti, and F. Martín. "Hybrid Gaussian-B-spline basis for the electronic continuum: Photoionization of atomic hydrogen". In: *Physical Review A - Atomic, Molecular, and Optical Physics* 90 (2014), p. 012506 (cit. on p. 1).

[37] A. P. Woźniak et al. "A systematic construction of Gaussian basis sets for the description of laser field ionization and high-harmonic generation". In: *The Journal of chemical physics* 154 (2021), p. 094111 (cit. on p. 1).

[38] M. Werther, S. L. Choudhury, and F. Großmann. "Coherent state based solutions of the time-dependent Schrödinger equation: hierarchy of approximations to the variational principle". In: *International Reviews in Physical Chemistry* 40 (2021), pp. 81–125 (cit. on pp. 1, 4).

[39] G. A. Worth and B. Lasorne. "Gaussian Wave Packets and the DD-vMCG Approach". In: *Quantum Chemistry and Dynamics of Excited States* (2020), pp. 413–433 (cit. on p. 1).

[40] G. W. Richings et al. "Quantum dynamics simulations using Gaussian wavepackets: the vMCG method". In: *International Reviews in Physical Chemistry* 34 (2015), pp. 269–308 (cit. on p. 1).

[41] D. V. Shalashilin and I. Burghardt. "Gaussian-based techniques for quantum propagation from the time-dependent variational principle: Formulation in terms of trajectories of coupled classical and quantum variables". In: *The Journal of Chemical Physics* 129 (2008), p. 084104 (cit. on p. 1).

[42] G. A. Worth, M. A. Robb, and I. Burghardt. "A novel algorithm for non-adiabatic direct dynamics using variational Gaussian wavepackets". In: *Faraday Discussions* 127 (2004), p. 307 (cit. on p. 1).

[43] A. F. White et al. "Computation of high-harmonic generation spectra of the hydrogen molecule using time-dependent configuration-interaction". In: *Molecular Physics* 114 (2016), pp. 947–956 (cit. on p. 1).

[44] E. Luppi and M. Head-Gordon. "The role of Rydberg and continuum levels in computing high harmonic generation spectra of the hydrogen atom using time-dependent configuration interaction". In: *The Journal of Chemical Physics* 139 (2013), p. 164121 (cit. on p. 1).

[45] M. Awasthi, Y. V. Vanne, and A. Saenz. "Non-perturbative solution of the time-dependent Schrödinger equation describing H2 in intense short laser pulses". In: *Journal of Physics B: Atomic, Molecular and Optical Physics* 38 (2005), pp. 3973–3985 (cit. on p. 1).

[46] M. Bonfanti, G. A. Worth, and I. Burghardt. "Multi-Configuration Time-Dependent Hartree Methods: From Quantum to Semiclassical and Quantum-Classical". In: *Quantum Chemistry and Dynamics of Excited States* (2020), pp. 383–411 (cit. on p. 1).

[47] C. Jhala and M. Lein. "Multiconfiguration time-dependent Hartree approach for electron-nuclear correlation in strong laser fields". In: *Physical Review A - Atomic, Molecular, and Optical Physics* 81 (2010), p. 063421 (cit. on p. 1).

[48] H. D. Meyer, F. Gatti, and G. A. Worth. *Multidimensional Quantum Dynamics*. Ed. by H. Meyer, F. Gatti, and G. A. Worth. Wiley, 2009, pp. 1–419 (cit. on p. 1).

[49] M. H. Beck et al. "The multiconfiguration time-dependent Hartree MCTDH method: A highly efficient algorithm for propagating wavepackets". In: *Physics Report* 324 (2000), pp. 1–105 (cit. on p. 1).

[50] D. J. Haxton, K. V. Lawler, and C. W. McCurdy. "Multiconfiguration time-dependent Hartree-Fock treatment of electronic and nuclear dynamics in diatomic molecules". In: *Physical Review A - Atomic, Molecular, and Optical Physics* 83 (2011), p. 063416 (cit. on p. 2).

[51] J. Caillat et al. "Correlated multielectron systems in strong laser fields: A multiconfiguration time-dependent Hartree-Fock approach". In: *Physical Review A - Atomic, Molecular, and Optical Physics* 71 (2005), p. 012712 (cit. on p. 2).

[52] J. Zanghellini et al. "Testing the multi-configuration time-dependent Hartree–Fock method". In: *Journal of Physics B: Atomic, Molecular and Optical Physics* 37 (2004), pp. 763–773 (cit. on p. 2).

[53] M. Lewenstein et al. "Theory of high-harmonic generation by low-frequency laser fields". In: *Physical Review A* 49 (1994), pp. 2117–2132 (cit. on pp. 2, 16).

[54] P. B. Corkum. "Plasma perspective on strong field multiphoton ionization". In: *Physical Review Letters* 71 (1993), pp. 1994–1997 (cit. on pp. 2, 16).

[55] C. Symonds et al. "Coupled-coherent-states approach for high-order harmonic generation". In: *Physical Review A - Atomic, Molecular, and Optical Physics* 91 (2015), p. 023427 (cit. on pp. 2, 4).

[56] A. Kirrander and D. V. Shalashilin. "Quantum dynamics with fermion coupled coherent states: Theory and application to electron dynamics in laser fields". In: *Physical Review A* 84 (2011), p. 033406 (cit. on pp. 2, 4, 6).

[57] D. V. Shalashilin, M. S. Child, and A. Kirrander. "Mechanisms of double ionization in strong laser field from simulation with Coupled Coherent States: Beyond reduced dimensionality models". In: *Chemical Physics* 347 (2008), pp. 257–262 (cit. on pp. 2, 4).

[58] D. V. Shalashilin and M. S. Child. "Real time quantum propagation on a Monte Carlo trajectory guided grids of coupled coherent states: 26D simulation of pyrazine absorption spectrum". In: *The Journal of Chemical Physics* 121 (2004), pp. 3563–3568 (cit. on pp. 4, 6, 80).

[59] Z. Zhou and S.-I. Chu. "Photoionization dynamics and angular squeezing phenomenon in intense long-wavelength laser fields". In: *Physical Review A* 83 (2011), p. 033406 (cit. on p. 4).

[60] M. Eidi, M. Vafaee, and M. Rooein. "Complementary version of fermion coupled coherent states method and gram-schmidt algorithm: Theory and applications for electronic states of H2 and H2+". In: *Journal of Computational Chemistry* 39 (2018), pp. 679–684 (cit. on pp. 4, 6, 8, 9).

[61] M. Eidi, M. Vafaee, and A. Landsman. "Static Coherent States Method: One- and Two-Electron Laser-Induced Systems with Classical Nuclear Dynamics". In: *Applied Sciences* 8 (2018), p. 1252 (cit. on pp. 4, 9, 10).

[62] M. Eidi et al. "A new version of fermion coupled coherent states method: Theory and applications in simulation of two-electron systems". In: *Chemical Physics Letters* 653 (2016), pp. 60–66 (cit. on pp. 4, 6–8, 10, 80).

[63] M. Eidi et al. "High-order harmonic generation by static coherent states method in single-electron atomic and molecular systems". In: *Journal of Computational Chemistry* 42 (2021), pp. 1312–1320 (cit. on pp. 4, 20).

[64] D. Huber and E. J. Heller. "Generalized Gaussian wave packet dynamics". In: *The Journal of Chemical Physics* 87 (1987), pp. 5302–5311 (cit. on p. 4).

[65] D. Huber and E. J. Heller. "Hybrid mechanics: A combination of classical and quantum mechanics". In: *The Journal of Chemical Physics* 89 (1988), pp. 4752–4760 (cit. on p. 4).

[66] D. Huber et al. "Hybrid mechanics. II". In: *The Journal of Chemical Physics* 90 (1989), pp. 7317–7329 (cit. on p. 4).

[67] L. M. Andersson. "Quantum dynamics using a discretized coherent state representation: An adaptive phase space method". In: *The Journal of Chemical Physics* 115 (2001), pp. 1158–1165 (cit. on p. 4).

[68] D. V. Shalashilin and M. S. Child. "Electronic energy levels with the help of trajectory-guided random grid of coupled wave packets. I. Six-dimensional simulation of H2". In: *The Journal of Chemical Physics* 122 (2005), p. 224108 (cit. on pp. 7, 8).

[69] D. V. Shalashilin and M. S. Child. "A version of diffusion Monte Carlo method based on random grids of coherent states. II. Six-dimensional simulation of electronic states of H2". In: *The Journal of Chemical Physics* 122 (2005), p. 224109 (cit. on p. 8).

[70] M. M. Madsen and J. M. Peek. "Eigenparameters for the lowest twenty electronic states of the hydrogen molecule ion". In: *Atomic Data and Nuclear Data Tables* 2 (1970), IN3–204 (cit. on p. 10).

[71] H. J. Wörner et al. "Charge migration and charge transfer in molecular systems". In: *Structural Dynamics* 4 (2017), p. 061508 (cit. on pp. 12, 13).

[72] K. J. Schafer et al. "Above threshold ionization beyond the high harmonic cutoff". In: *Physical Review Letters* 70 (1993), pp. 1599–1602 (cit. on p. 16).

[73] J. L. Krause, K. J. Schafer, and K. C. Kulander. "High-order harmonic generation from atoms and ions in the high intensity regime". In: *Physical Review Letters* 68 (1992), pp. 3535–3538 (cit. on p. 16).

[74] D. B. Milosevic. "Cut-off law for high-harmonic generation by an elliptically polarized laser field". In: *Journal of Physics B: Atomic, Molecular and Optical Physics* 33 (2000), pp. 2479–2488 (cit. on p. 16).

[75] T. Popmintchev et al. "The attosecond nonlinear optics of bright coherent X-ray generation". In: *Nature Photonics* 4 (2010), pp. 822–832 (cit. on p. 17).

[76] C. H. Garcia. "Coherent attosecond light sources based on high-order harmonic generation : influence of the propagation effects". In: *PhD Thesis* (2013) (cit. on p. 17).

[77] J. L. Krause, K. J. Schafer, and K. C. Kulander. "Calculation of photoemission from atoms subject to intense laser fields". In: *Physical Review A* 45 (1992), pp. 4998–5010 (cit. on p. 19).

[78] H. Ahmadi et al. "Effect of nuclear motion on high-order-harmonic generation of H2+ in intense ultrashort laser pulses". In: *Physical Review A - Atomic, Molecular, and Optical Physics* 90 (2014), p. 043411 (cit. on p. 21).

[79] P. B. Corkum, N. H. Burnett, and M. Y. Ivanov. "Subfemtosecond pulses". In: *Optics Letters* 19 (1994), p. 1870 (cit. on p. 21).

[80] N. Safaei. "Generation of isolated attosecond pulses by polarization gating of high-order harmonic emission from H2+ in intense ultrashort laser fields". In: *Laser Physics Letters* 15 (2018), p. 015202 (cit. on p. 22).

[81] S. F. Boys. "Electronic wave functions - I. A general method of calculation for the stationary states of any molecular system". In: *Proceedings of the Royal Society of London. Series A. Mathematical and Physical Sciences* 200 (1950), pp. 542–554 (cit. on p. 24).

[82] S. Obara and A. Saika. "Efficient recursive computation of molecular integrals over Cartesian Gaussian functions". In: *The Journal of Chemical Physics* 84 (1986), pp. 3963–3974 (cit. on pp. 26, 86, 87).

[83] L. Brooke et al. "Distributed Gaussian orbitals for the description of electrons in an external potential". In: *Journal of Molecular Modeling* 24 (2018), p. 216 (cit. on p. 31).

[84] Z. xian Wang and E. J. Heller. "Semiclassical investigation of the revival phenomena in a one-dimensional system". In: *Journal of Physics A: Mathematical and Theoretical* 42 (2009), p. 285304 (cit. on p. 37).

[85] S. Wang et al. "Comparative study of photoionization of atomic hydrogen by solving the one- A nd three-dimensional time-dependent Schrödinger equations". In: *Chinese Physics B* 30 (2021), p. 083301 (cit. on p. 39).

[86] R. D. Bardo and K. Ruedenberg. "Even-tempered atomic orbitals. III. Economic deployment of Gaussian primitives in expanding atomic SCF orbitals". In: *The Journal of Chemical Physics* 59 (1973), pp. 5956–5965 (cit. on p. 42).

[87] S. Battaglia et al. "Distributed Gaussian orbitals for molecular calculations: application to simple systems". In: *Molecular Physics* 118 (2020), p. 1615646 (cit. on pp. 49, 50, 52).

[88] F. M. Fernández and J. Garcia. "Highly Accurate Potential Energy Curves for the Hydrogen Molecular Ion". In: *ChemistrySelect* 6 (2021), pp. 9527–9534 (cit. on p. 52).

[89] L. Exl. "Splitting methods for the Schrödinger equation". In: (2013) (cit. on p. 54).

[90] F. Grossmann. *Atoms in Strong Laser Fields*. Vol. 1. Springer International Publishing, 2018, pp. 113–172 (cit. on p. 55).

[91] C. Jhala, I. Dreissigacker, and M. Lein. "Absorbing boundaries in the mean-field approximation". In: *Physical Review A - Atomic, Molecular, and Optical Physics* 82 (2010) (cit. on p. 67).

[92] T. Helgaker, P. Jørgensen, and J. Olsen. *Molecular Electronic-Structure Theory*. John Wiley & Sons, Ltd, 2000, p. 938 (cit. on p. 81).

Declaration / Versicherung

Erklärung:

Hiermit versichere ich, dass ich die vorliegende Arbeit ohne unzuläßige Hilfe Dritter und ohne Benutzung anderer als der angegebenen Hilfsmittel angefertigt habe; die aus fremden Quellen direkt oder indirekt bernommenen Gedanken sind als solche kenntlich gemacht. Die Arbeit wurde bisher weder im Inland noch im Ausland in gleicher oder hnlicher Form einer anderen Prüfungsbehörde vorgelegt. Diese Arbeiten wurden unter der Leitung von Prof. Dr. Jan Michael Rost am Max-Planck-Institut für Physik komplexer Systeme in Dresden durchgeführt. Ich erkläre hiermit, dass keine früheren erfolglosen Promotionsverfahren stattgefunden haben. Ich erkenne die Promotionsordnung der Fakultät Physik der Technische Universität Dresden an.

Unterschrift :

Ort, Datum : Dresden, 12.09.2022